Supplementary Video Captions

Supplementary Video 1, Deconvolution comparison on simulated object. Two parallel lines in 3D space are blurred by the iSIM point spread function (1st column) and deconvolved using traditional ('Trad', 2nd column) and Wiener-Butterworth ('WB', 3rd column) back projectors. For clarity, only a transverse XY plane through the object is shown. Corresponding line profiles through the middle of the image (4th column) are also shown, updated after each iteration count. **See also Fig. 1e**.

Supplementary Video 2, Deconvolution comparison on fixed U2OS cells, immunolabeled with Tomm20 Alexa-488. Fixed U2OS cells were immunolabeled with Tomm 20 Alexa-488 and imaged with iSIM. Single planes (top) and higher magnification views (bottom, corresponding to the yellow rectangular region) are shown, derived from image volumes deconvolved using traditional (left) and Wiener-Butterworth (right) back projectors, with iteration number (it) indicated. **See also Fig. 1f, g**.

Supplementary Video 3, Time-lapse images of U2OS cells expressing ERmoxGFP. Image volumes were acquired with iSIM every 2 s, over 150 time points, and deconvolved (1 iteration) using the Wiener-Butterworth back projector. The deconvolved maximum intensity projection is shown here.

Supplementary Video 4, Angular maximum intensity projections, comparing raw and deconvolved *C. elegans* embryos showing histone and neuronal markers. *C. elegans* embryos expressing neuronal (green, GFP-membrane) and pan-nuclear (magenta, mCherry-histone) markers were acquired with diSPIM (top, raw views) and deconvolved using traditional ('Trad', bottom left) and Wiener-Butterworth ('WB', bottom right) back projectors. Isotropic reconstructions are obtained with both back projectors. **See also Fig. 2a-d**.

Supplementary Video 5, Two-color time-lapse images of *C. elegans* embryos expressing histone and neuronal markers. *C. elegans* embryos expressing neuronal (green, GFP-membrane) and pan-nuclear (magenta, mCherry-histone) markers were acquired with diSPIM every 1.5 min, over 50 time points, and deconvolved using traditional and Wiener-Butterworth back projectors. Maximum intensity projections of raw data (View A, left column) and deconvolved data using traditional ('Trad', middle column) and Wiener-Butterworth ('WB', right) back projectors are shown for lateral (top) and axial (bottom) views. Time is referenced as minutes post fertilization. **See also Fig. 2a-d**.

Supplementary Video 6, Time-lapse images of Jurkat T cells expressing GFP-actin. Jurkat T cells expressing GFP-actin were acquired with a quadruple-view light-sheet microscope every 15 s, over 30 time points, and deconvolved using traditional and Wiener-Butterworth back projectors. Left: Perspective 3D view of Wiener-Butterworth deconvolution result . Right: Maximum intensity projections of raw (top row) and deconvolved results using traditional ('Trad', middle row) and Wiener-Butterworth ('WB', bottom row) back projectors are shown for lateral (left) and axial (right) views. **See also Fig. 2e-g**.

Supplementary Video 7, Time-lapse images of zebrafish embryo expressing Lyn-eGFP. Volumetric images of 32-hour zebrafish embryo expressing Lyn-eGFP under the control of the ClaudinB were acquired with diSPIM every 30 s, over 900 time points (a total acquisition period of 7.5 h), and deconvolved using the Wiener-Butterworth back projector. Maximum intensity projections of deconvolutions are shown for lateral (top) and axial (bottom) views. Labels that indicate anterior and posterior directions, the direction of the coverslip; and the skin cell layer are also indicated. Images were binned 2×2 relative to the data for display and memory purposes. **See also Fig. 2j**.

Supplementary Video 8, Higher magnification view of subregion in Supplementary Video 7, highlighting the immune cell migration. See also **Fig. 2m, n**.

Supplementary Video 9, Automated segmentation of cell membranes in zebrafish embryo lateral line. Slices indicated by z-distance from skin surface shows the automated segmentation result based on the raw data ('Raw', View A image (top)), deconvolved image with Wiener-Butterworth back projector ('WB', middle) and the overlay of the segmentations (bottom). **See also Fig. 2o, p.**

Supplementary Video 10, Wiener-Butterworth deconvolution compares favorably to Huygens deconvolution on single-view data acquired on Zeiss Z.1 light-sheet microscope. Z stacks are shown comparing the raw image (left), Huygens deconvolution (middle) and Wiener-Butterworth deconvolution (right). **See also Supplementary Fig. 13.**

Supplementary Video 11, Cleared tissue: mouse brain slice. A 4 x 2 x 0.5 mm^3 slab of brain tissue derived from a V1b transgenic mouse was immunolabeled and cleared using iDISCO+, imaged in the cleared tissue diSPIM, and reconstructed by registering the two views and deconvolving them. An Alexa Fluor 555 secondary antibody against tdTomato primary antibody sparsely labels neurons and neurites across the entire volume. See also **Fig. 3a**.

Supplementary Video 12, Cleared tissue: 4-color embryonic mouse intestine. A 2.1 x 2.5 x 1.5 mm^3 intestinal volume from an E18.5 mouse was immunolabeled and cleared using iDISCO, imaged in the cleared tissue diSPIM, and reconstructed by registering the two views and deconvolving them. Orange: Alexa Fluor 647 secondary antibody against Tomm20 primary antibody; purple: Alexa Fluor 568 secondary antibody against α-Tubulin primary antibody; yellow: Alexa Fluor 488 secondary antibody against PECAM-1 primary antibody; blue: DAPI, highlighting nuclei. See also **Fig. 3d**.

Supplementary Video 13, Cleared tissue: 2-color adult mouse intestine. A 2.3 x 0.7 x 0.5 mm^3 intestinal volume from an adult C57BL/6 mouse was immunolabeled and cleared using iDISCO, imaged in the cleared tissue diSPIM, and reconstructed by registering the two views and deconvolving them. Red: Alexa Fluor 488 secondary antibody against PECAM-1 primary antibody; Cyan: autofluorescence of tissue.

Supplementary Video 14, Cleared tissue: 2-color embryonic mouse stomach. A 2.4 x 2.7 x 1.0 mm^3 volume of stomach from an E18.5 mouse was immunolabeled and cleared using iDISCO, imaged in the cleared tissue diSPIM, and reconstructed by registering the two views and deconvolving them. Red: Alexa Fluor 647 secondary antibody against PECAM-1 primary antibody; Green: Alexa Fluor 568 secondary antibody against α-Tubulin primary antibody.

Supplementary Video 15, Cleared tissue: 2-color adult mouse ovary. A 2.6 x 1.9 x 0.5 mm^3 volume ovary from an adult C57BL/6 mouse was immunolabeled and cleared using iDISCO, imaged in the cleared tissue diSPIM, and reconstructed by registering the two views and deconvolving them. Green: Alexa Fluor 488 secondary antibody against CD11c primary antibody; Red: CF-568 secondary antibody against CD11b primary antibody.

Supplementary Video 16, Three-fold *C. elegans* embryos expressing GCaMP3 from a *myo-3* promoter were imaged in the reflective diSPIM on mirrored coverslips (155 volumes, each acquired every 350 ms). Maximum intensity projections of raw data (left column), traditional (Trad) joint deconvolution (second column), Wiener-Butterworth deconvolution (third column), and deep learning reconstruction (right column, 100 time points are used for training, and the other 55 time points are used for validation) are shown for lateral (top) and axial (bottom) views. See also **Fig. 4c**.

Supplementary Video 17, U2OS cells expressing mEmerald-α-Actinin were imaged in the reflective LLS microscope on mirrored coverslips (100 volumes, each acquired every 2.5 s). Maximum intensity projections of raw data (left column), Wiener-Butterworth deconvolution (middle column), and deep

learning reconstruction (right column, 80 time points are used for training, and the other 20 time points are used for validation) are shown for lateral (top) and axial (bottom) views. **See also Fig. 4f**.

Supplementary Video 18, *C. elegans* embryos with GFP-histone label were imaged with a free-space coupled diSPIM on a glass coverslip. Maximum intensity projections of raw view A (first column), raw view B (second column), traditional (Trad) joint deconvolution of view A and view B (third column), deep learning reconstruction (fourth column) based on single-view input (i.e., view A) and deep learning reconstruction (rightmost column) based on dual-view inputs (i.e., both view A and view B) are shown for lateral (top) and axial (bottom) views. In the deep learning reconstructions, 180 time points are used for training, and the other 110 time points are used for validation. hpf: hours post fertilization. See also **Fig. S4.4** in **Supplementary Note 4**.

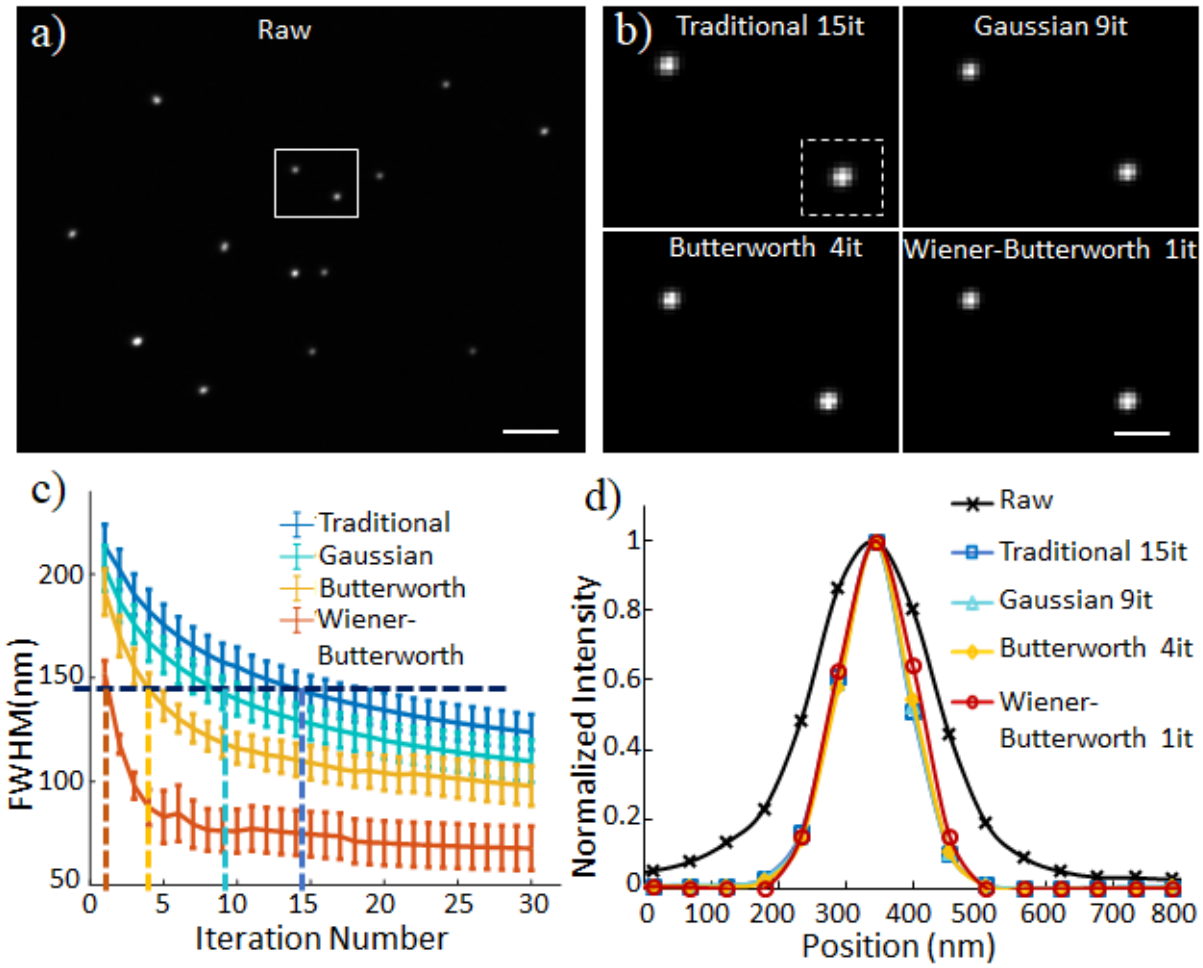

Supplementary Fig. 1, Comparing different back projectors when deconvolving 100 nm beads captured with the iSIM. a) 100 nm yellow green beads were imaged on the iSIM. Raw data are shown (single planes from imaging volumes). **b)** Deconvolved, higher magnification views of the white rectangle in **a)** with indicated back projector. **c)** Full width at half maximum (FWHM) values derived from n = 10 beads as shown in **Fig. 1**, standard deviations as well as mean values are shown. Note the considerably more rapid descent to the resolution-limited result of the Wiener-Butterworth back projector compared to other back projectors. The resolution limit of iSIM is indicated with the horizontal dotted line. **d**) Line profiles through the example bead highlighted by the dotted white rectangle in **b**), showing that all back projectors yield an equivalent estimate of the bead. Scale bars: 2 μm in **a)** and 500 nm in **b)**.

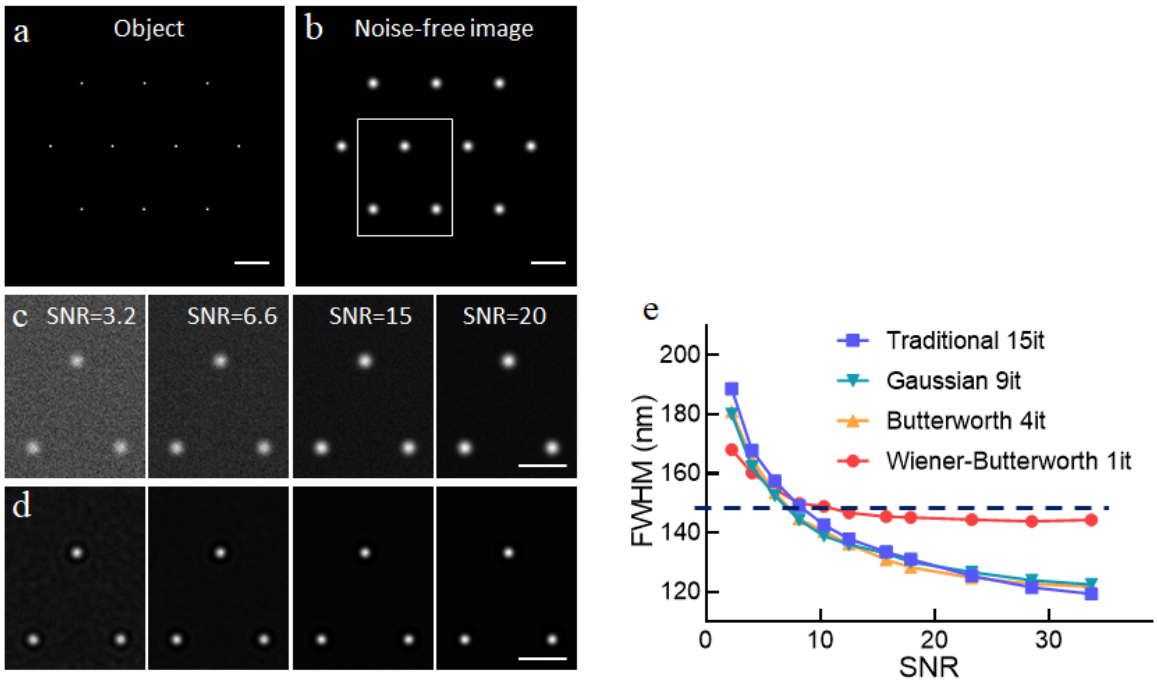

Supplementary Fig. 2, Simulated resolution vs. input data SNR curves for different back projectors. a) Ten synthetic point sources form the object. **b)** Blurring the object with the iSIM PSF generates a noise-free image. **c)** Gaussian and Poisson noise are added to the noise-free image to generate input images of variable SNR. See **Methods** for further detail on this procedure. **d)** Images in **c**) after 1 iteration deconvolution with Wiener-Butterworth filter. **e)** Average bead FWHM values vs. input data SNR are plotted for different back projectors. The Wiener-Butterworth filter provides more accurate (i.e. closer to the resolution-limit) resolution enhancement than do other choices over a wide range of SNRs.

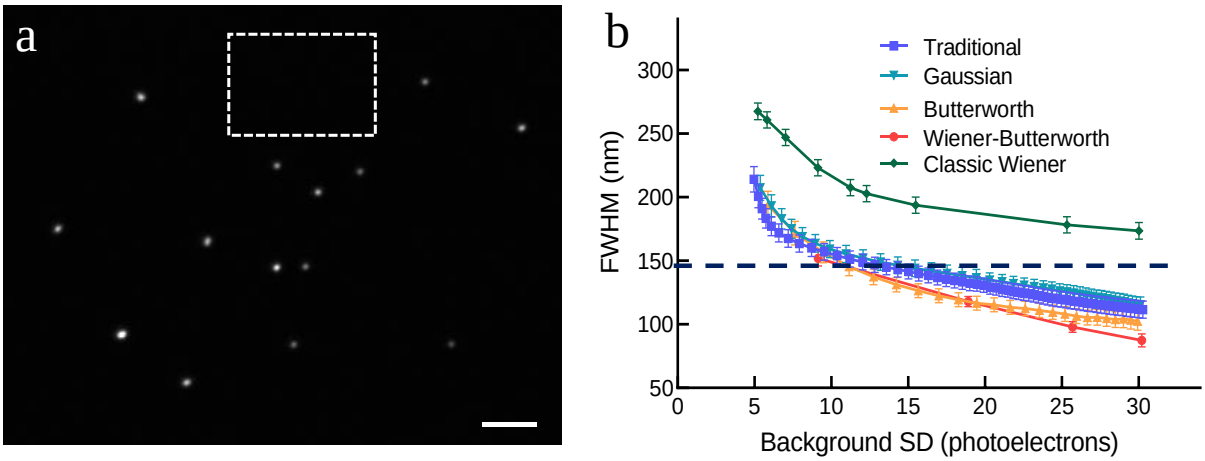

Supplementary Fig. 3, Resolution vs. background noise amplification for different back projectors. a) Raw bead data in **Supplementary Fig. 1** were deconvolved with different back projectors **b)** and the FHWM of n = 10 beads plotted as a function of the standard deviation of the background (corresponding to the dotted rectangular region in **a**) to assess noise-resolution tradeoffs achievable by the various deconvolution methods (central value represents mean and error bars indicate standard deviation). For the RLD methods, different noise-resolution combinations were generated by increasing the number of iterations, which both amplifies noise and improves resolution. For the classic Wiener filter, different noise-resolution combinations were generated by changing the filter parameter. Curves closer to the lower left origin of the plot are better as they indicate the ability to achieve a specified resolution with lower noise amplification. Deconvolution with the Wiener-Butterworth (WB) back projector offers consistently comparable or lower noise amplification at any given resolution than other approaches, i.e., despite its fast descent to the resolution limit, WB noise amplification is no worse than with other methods. The horizontal dotted line indicates the resolution limit. Scale bar in **a**) 2 µm.

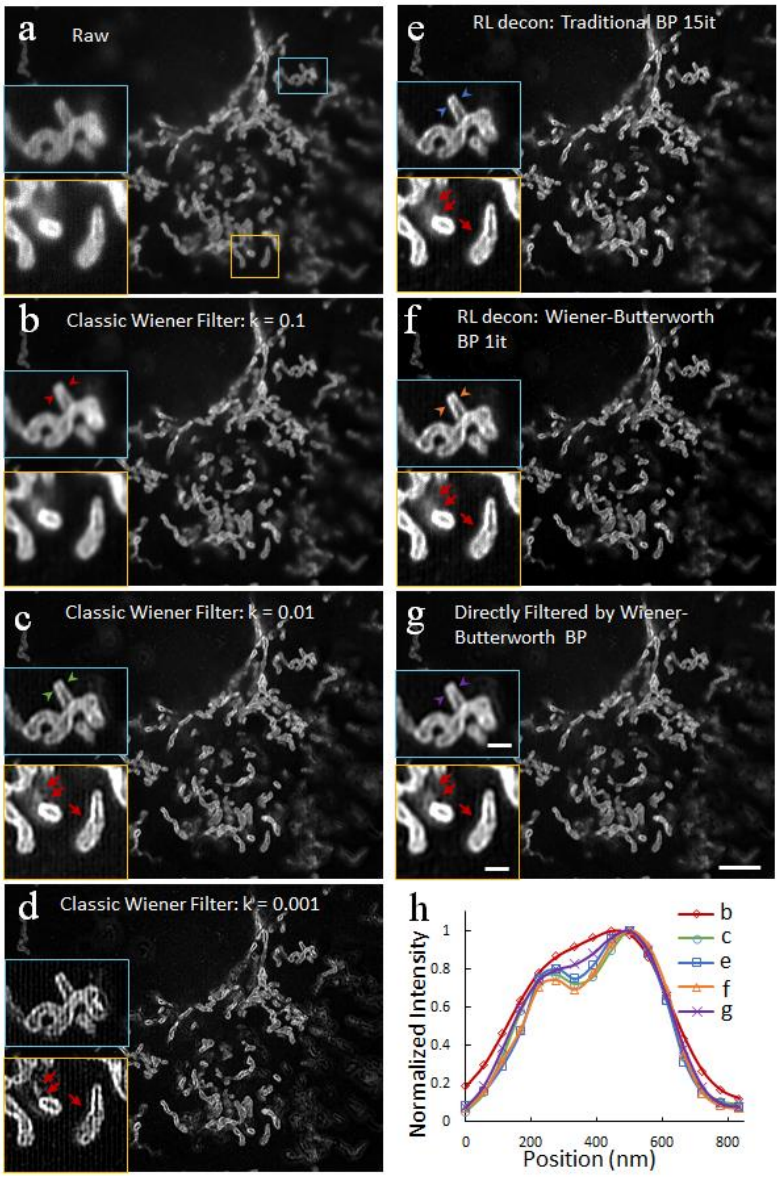

Supplementary Fig. 4, Comparing the Wiener Filter to Richardson Lucy Deconvolution. a) Fixed U2OS cells immunolabeled against Tomm20 and imaged with iSIM. Dataset is the same as in **Fig. 1f**. **b-d**) Data deconvolved using Wiener filter with k value as indicated. **e, f**) Richardson Lucy Deconvolution with conventional (**e**) and Wiener-Butterworth (**f**) back projectors with indicated iteration (it) numbers. **g)** Wiener deconvolution using the Wiener-Butterworth back projector instead of the typical kernel. Blue and orange rectangular insets in **a-g**) show higher magnification views. Line profiles across the mitochondrial structure marked with the arrowheads in **b, c, e-g** are shown in **h**). At k = 0.1 (**b**), the Wiener filter fails to resolve the boundaries of the mitochondria. Smaller values of k better resolve the mitochondria (**h**) but lead to progressively greater ringing artifacts (red arrows in **c-d**). Such artifacts are also present when using the Wiener-Butterworth filter in Wiener deconvolution, which also fails to fully resolve the mitochondrial boundaries. Richardson Lucy Deconvolution (**e, f**) resolve the mitochondria without introducing ringing. Scale bars: 5 μm in lower magnification view and 1 μm in inset. Experiments were repeated on similar datasets at least 2 times, with similar results obtained each time; representative data from a single experiment are shown.

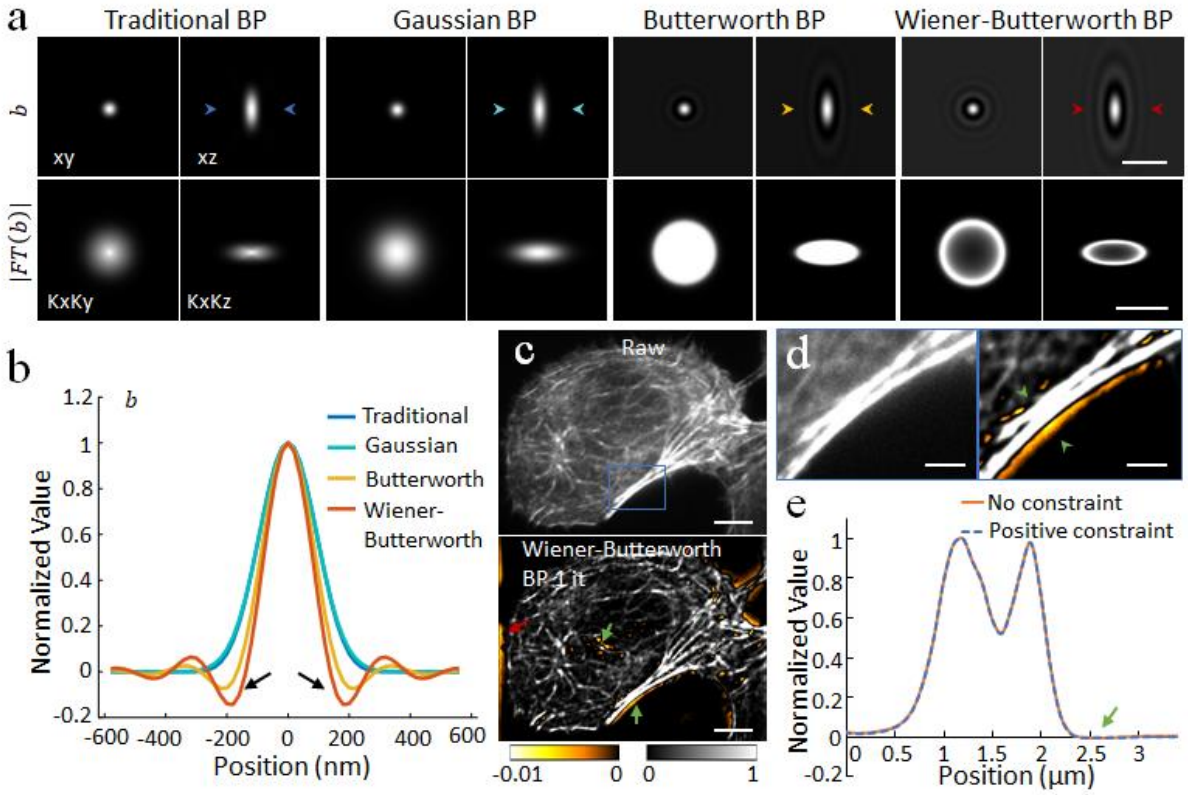

Supplementary Fig. 5, Negative value analysis. a) Different back projectors in real space (top row) and Fourier space (bottom row). See also **Fig. 1b. b)** Line profiles through regions demarcated by arrowheads in **a**)**.** Butterworth and Wiener-Butterworth back projectors exhibit negative values, highlighted by black arrows. **c)** Alexa Fluor 488 Phalloidin-labeled actin in fixed U2OS cell, as in **Supplementary Fig. 3**. Raw data (top) and Richardson Lucy deconvolution with Wiener-Butterworth back projector prior to negative value removal, 1 iteration (bottom) are shown. Negative values are highlighted with arrows and with yellow colormap. **d)** Higher magnification of blue rectangular region in **c**), showing raw data (left) and deconvolved result prior to negative value removal (right). Note that negative values mostly arise in background pixels, or in very low intensity pixels adjacent to regions of higher intensity. **e**) Line profile through region demarcated by arrowheads in **d**, comparing the effect of setting negative valued pixels to zero (positivity constraint, blue dotted line) to the deconvolved data without constraint (orange solid line). Profiles overlay except for very slight differences near zero on right-hand portion of curve (arrow). Scale bars: 1 μm (top) and 1/100 nm^{-1} (bottom) in **a)**, 5 μm in **c)**, and 2 μm in **d**). Experiments were repeated on similar datasets at least 2 times, with similar results obtained each time; representative data from a single experiment are shown.

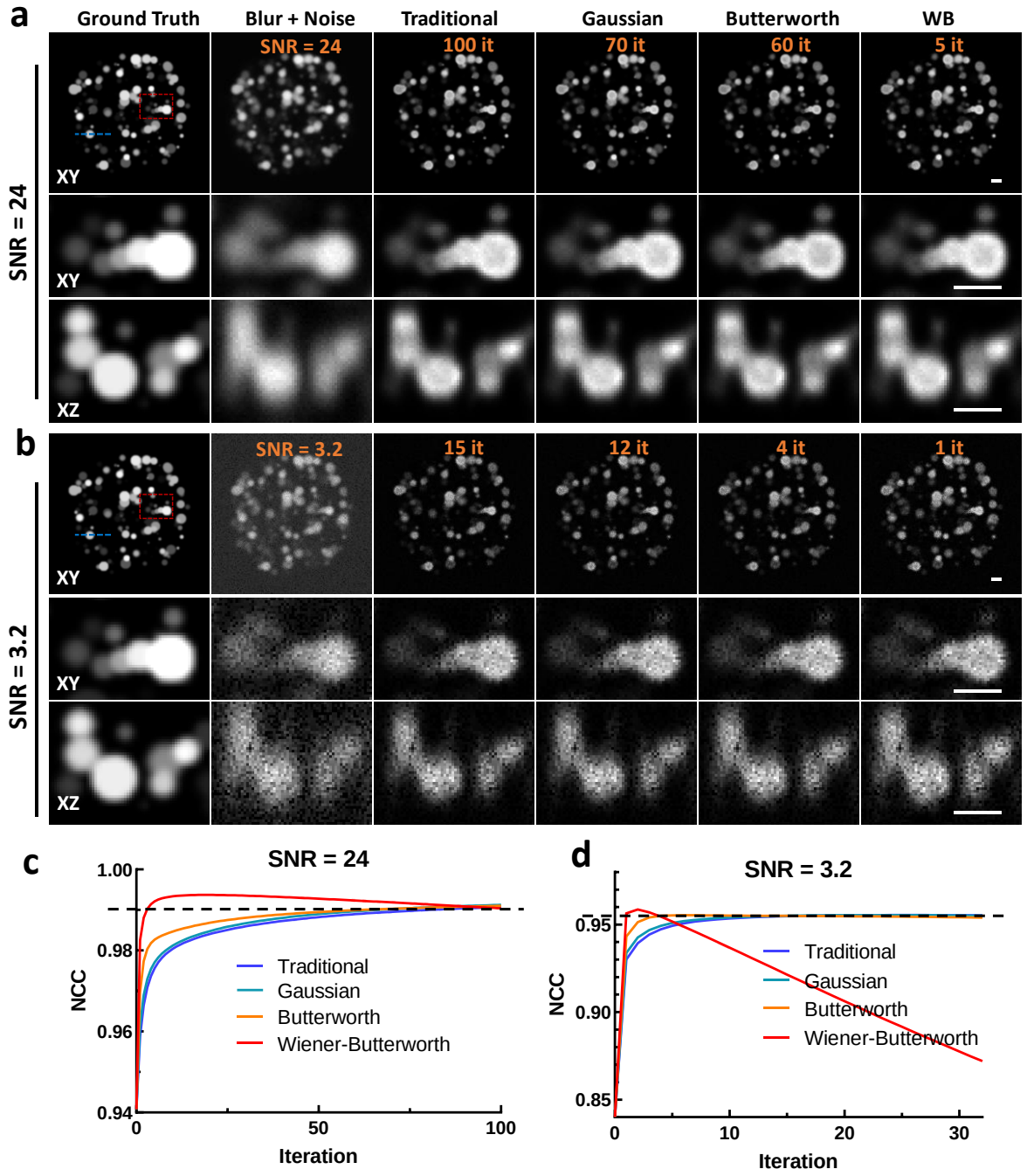

Supplementary Fig. 6, Unmatched back projectors accelerate deconvolution of spherical phantoms. a) The ground truth phantom, corresponding blurred and noisy image, and corresponding deconvolved reconstructions for traditional, Gaussian, Butterworth, and Wiener-Butterworth (WB) approaches are shown (columns) for the middle plane through the phantom. The phantom was blurred with the iSIM PSF used in **Fig. 1**. The signal-to-noise ratio (SNR) in the blurred, noisy image was set at 24, and the number of iterations (it) needed for the resolution-limited reconstruction is indicated at the top of each column. Middle and third rows show higher magnification views of red dotted rectangle (XY, lateral view) and along blue dotted line (XZ, axial view) in top left subimage. **b)** As in **a)**, except more noise was added to

achieve an SNR of 3.2. **c, d)** Normalized cross-correlation (NCC) of the reconstruction compared to the ground truth as a function of iteration number for the different back projectors, and for the different SNR levels. Note the faster rise in NCC and subsequent decay for the WB back projector. All scale bars: 1 μm. See **Methods** for further details on how phantoms were generated, SNR was determined, and how NCC is computed.

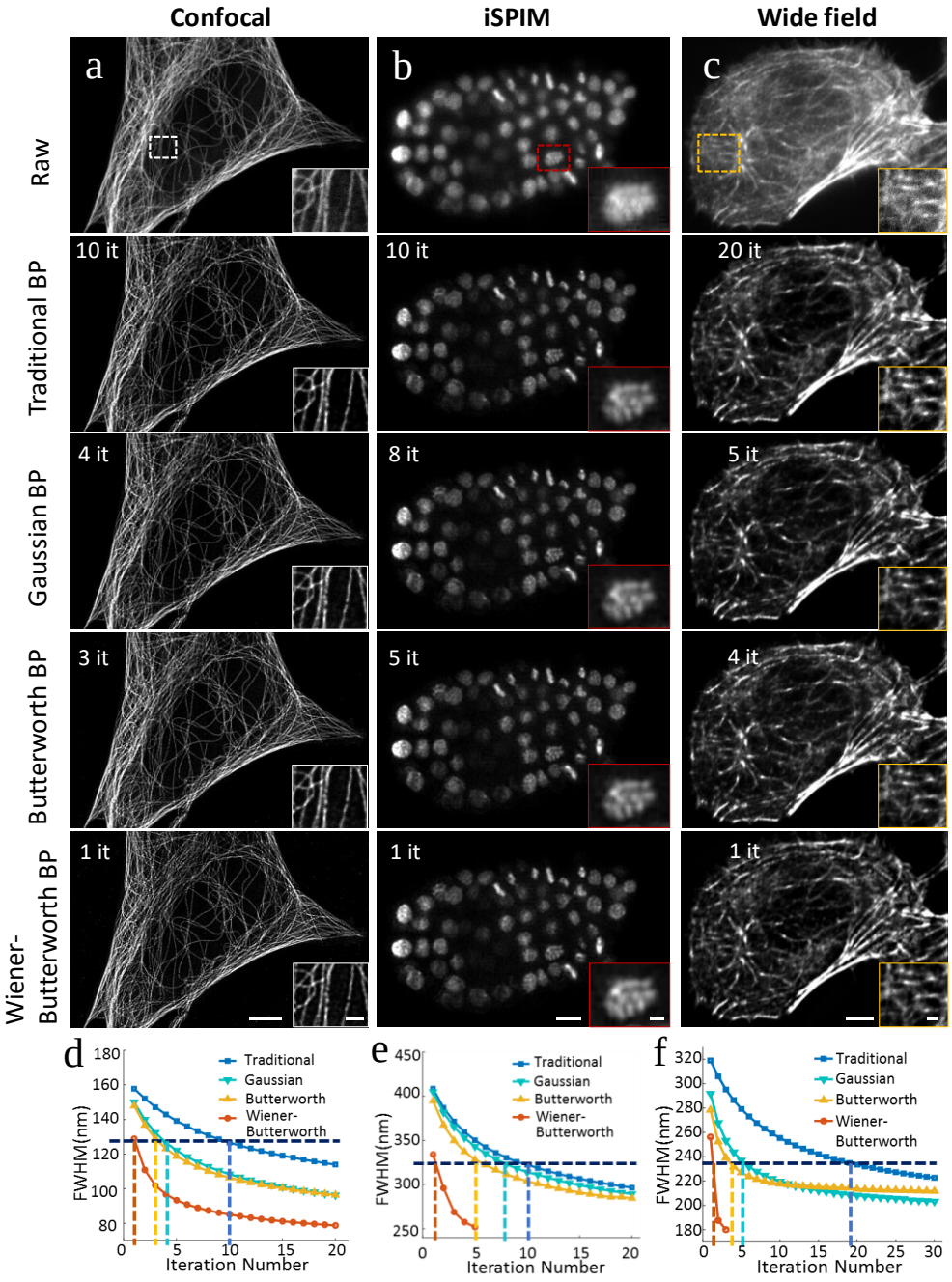

Supplementary Fig. 7, Unmatched back projectors speed iterative deconvolution convergence in confocal, light-sheet, and widefield microscopy. Confocal (**a**, immunolabeled microtubules), inverted selective plane illumination (iSPIM, **b**, GFP-labeled histones) and widefield (**c**, phalloidin-labeled actin) microscopy images are shown. Note higher magnification insets at lower right corner of each image. Single planes from imaging stacks are shown, with iteration number and back projector as indicated. The effect of different back projectors is illustrated, with experimental resolution vs. iteration number curves derived

by plotting the mean FWHM of 10 microtubule filaments (**d**) or beads (**e** and **f**) vs. iteration number as shown in graphs at bottom. Iteration numbers (vertical dotted lines) corresponding to the resolution limit (horizontal dotted lines) were used in generating the images, as in **Fig. 1d, f**. Scale bar: 5 μm in main figures and 5 μm in subsets. Experiments were repeated on similar datasets 2 times for **a)**, **c)**, and at least 3 times for **b)**, with similar results obtained each time; representative data from a single experiment are shown.

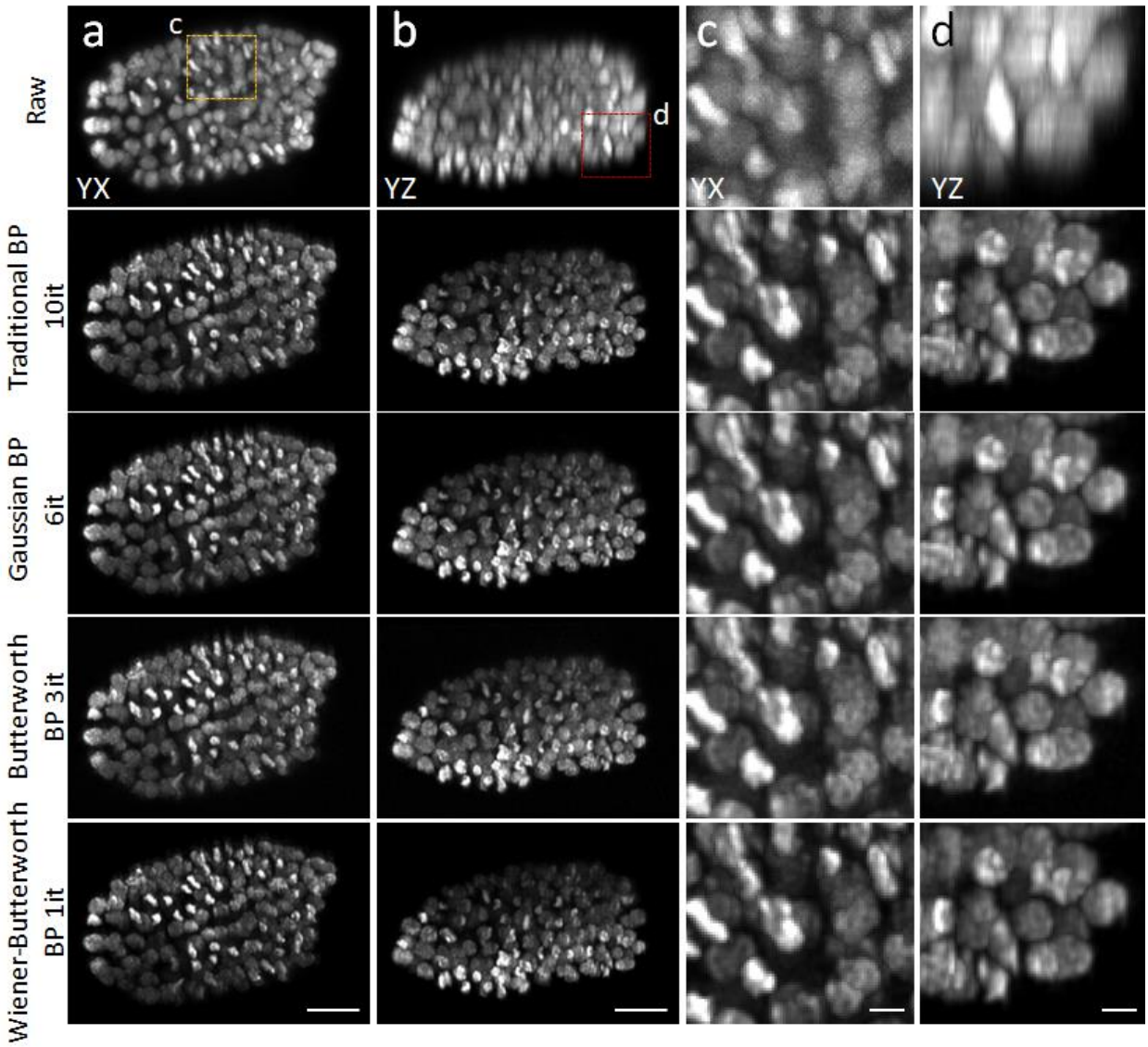

Supplementary Fig. 8, Unmatched back projectors reduce the number of iterations required when deconvolving dual-view light-sheet microscopy (diSPIM) data. Nematode embryos expressing GFP-labeled histones were imaged in diSPIM. Lateral (**a**) and axial (**b**) views are shown for raw and deconvolved data, with iteration ('it') numbers and back projectors as indicated. Higher magnification views **c, d**) correspond to yellow and red rectangular regions in **a, b**). Scale bars: 10 μm in **a, b**; 2 μm in **c, d**. Experiments were repeated on similar datasets at least 3 times, with similar results obtained each time; representative data from a single experiment are shown.

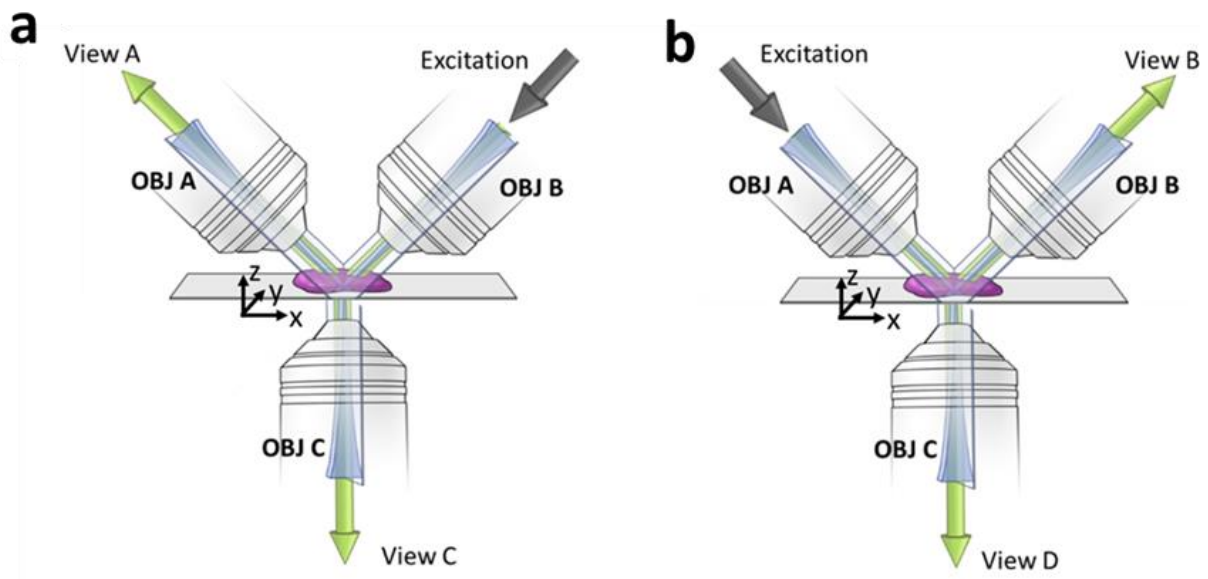

Supplementary Fig. 9, Schematic of the quad-view SPIM system for acquiring up to 4 volumetric views. Dual views (View A and View B) are sequentially acquired by diSPIM using the top two objectives (OBJ A and OBJ B). Four views (View A, B, C and D) are acquired with the additional third objective (OBJ C). **(a)** Views A/C are simultaneously acquired when the excitation is introduced from OBJ B; **(b)** Views B/D are simultaneously acquired when the excitation is introduced from OBJ A. Here, x, y, z coordinates are defined from the perspective of the coverslip.

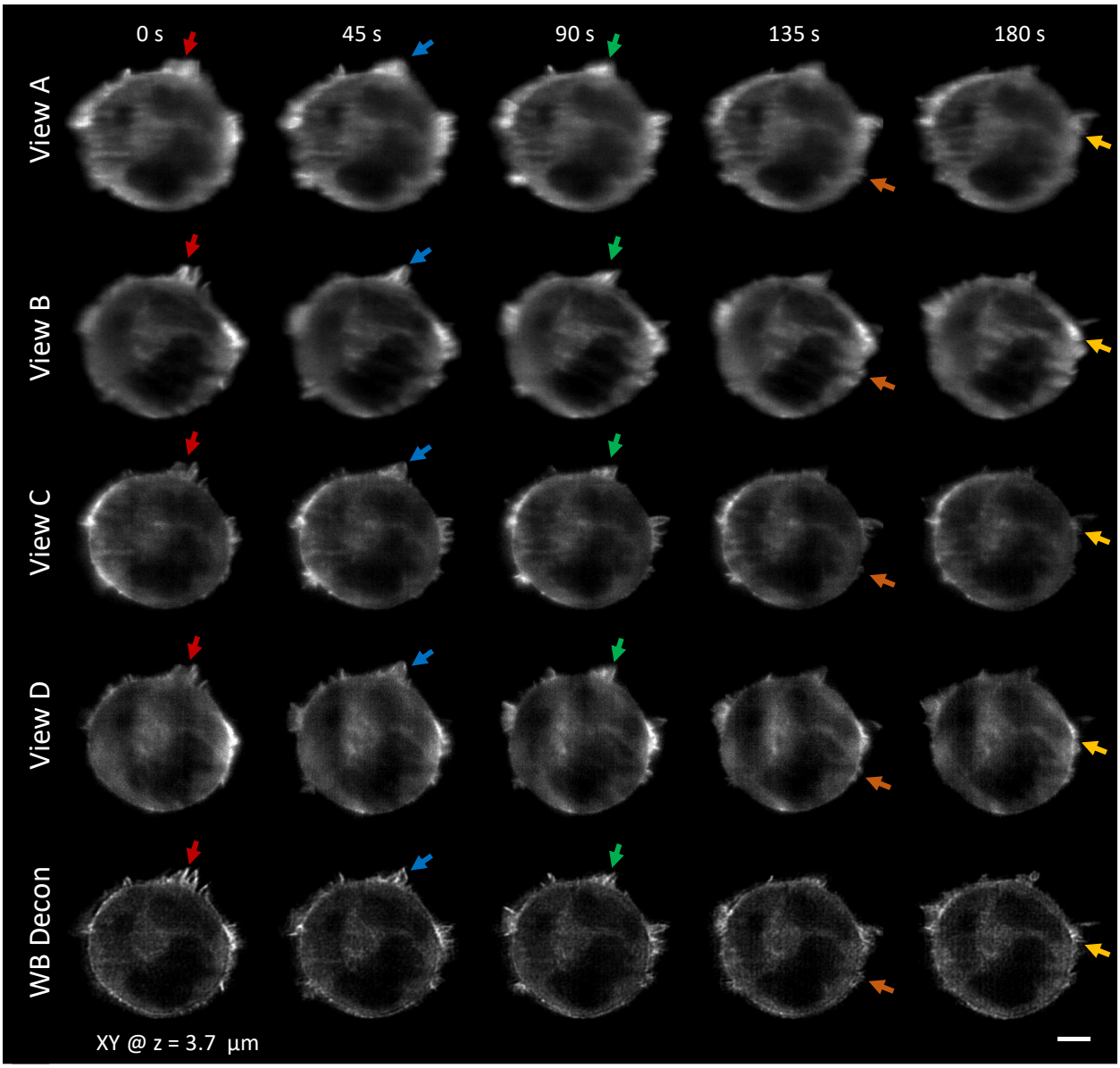

Supplementary Fig. 10, Quad-view Wiener-Butterworth (WB) deconvolution resolves more detail than raw views. Colored arrow pairs highlight fine, GFP-labeled actin structures expressed in Jurkat T cell for comparison. View A and View B are collected by the upper 0.8 NA collection lenses; View C and View D are collected by the lower 1.2 NA collection lens. Scale bar: 5 µm. See also **Fig. 2f**. Experiments were repeated on similar datasets 2 times, with similar results obtained each time; representative data from a single experiment are shown.

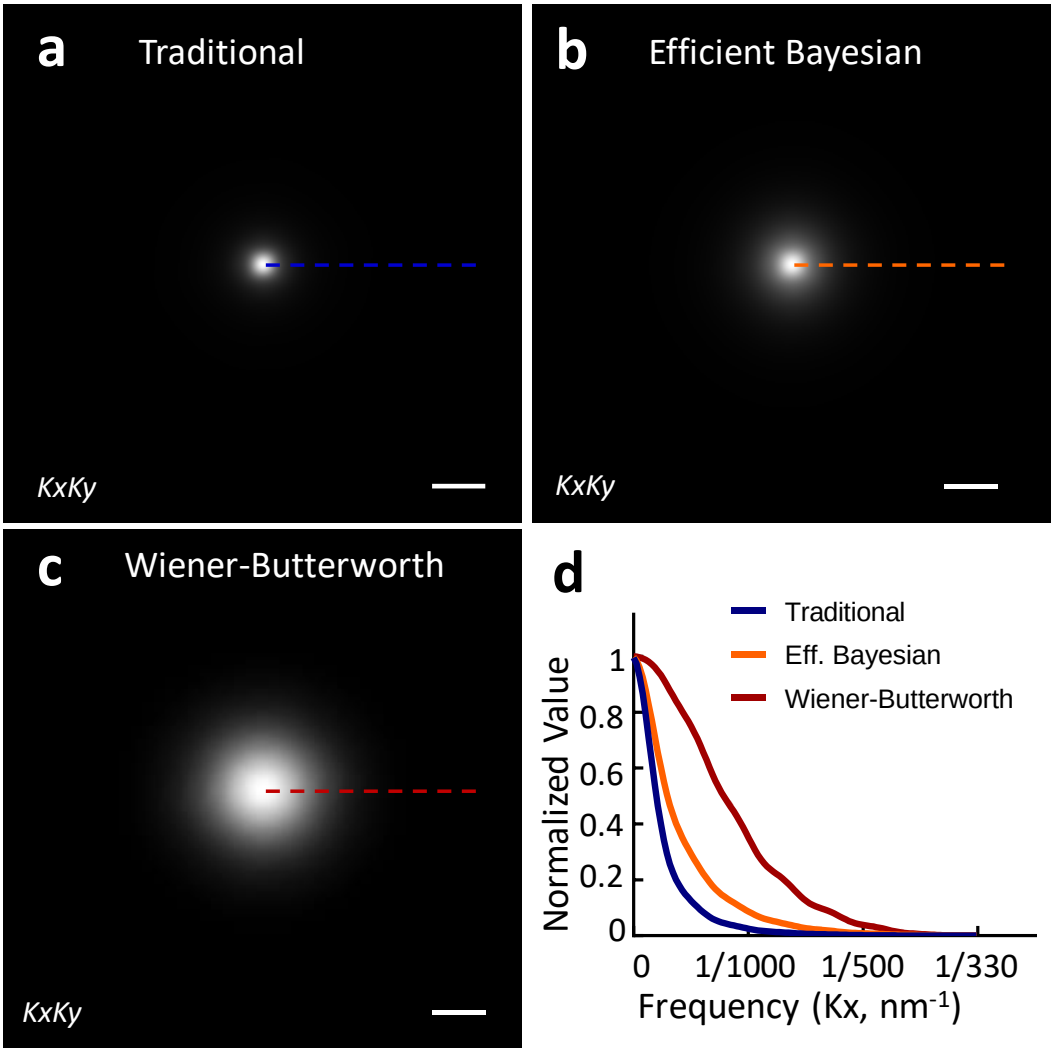

Supplementary Fig. 11, |FT(*f*) x FT(*b*)| comparison for traditional, Efficient Bayesian and Wiener-Butterworth back projectors in Quadruple-view light-sheet microscopy. |FT(*f*) x FT(*b*)|for the bottom objective, with traditional **(a)**, Efficient Bayesian **(b)** and Wiener-Butterworth **(c)** back projectors. **(d)** line profiles through the images in **a**, **b** and **c**. Scale bars: 1/1000 nm^{-1}. The data that accompany these back projectors are shown in **Fig. 2f and Supplementary Fig. 10**.

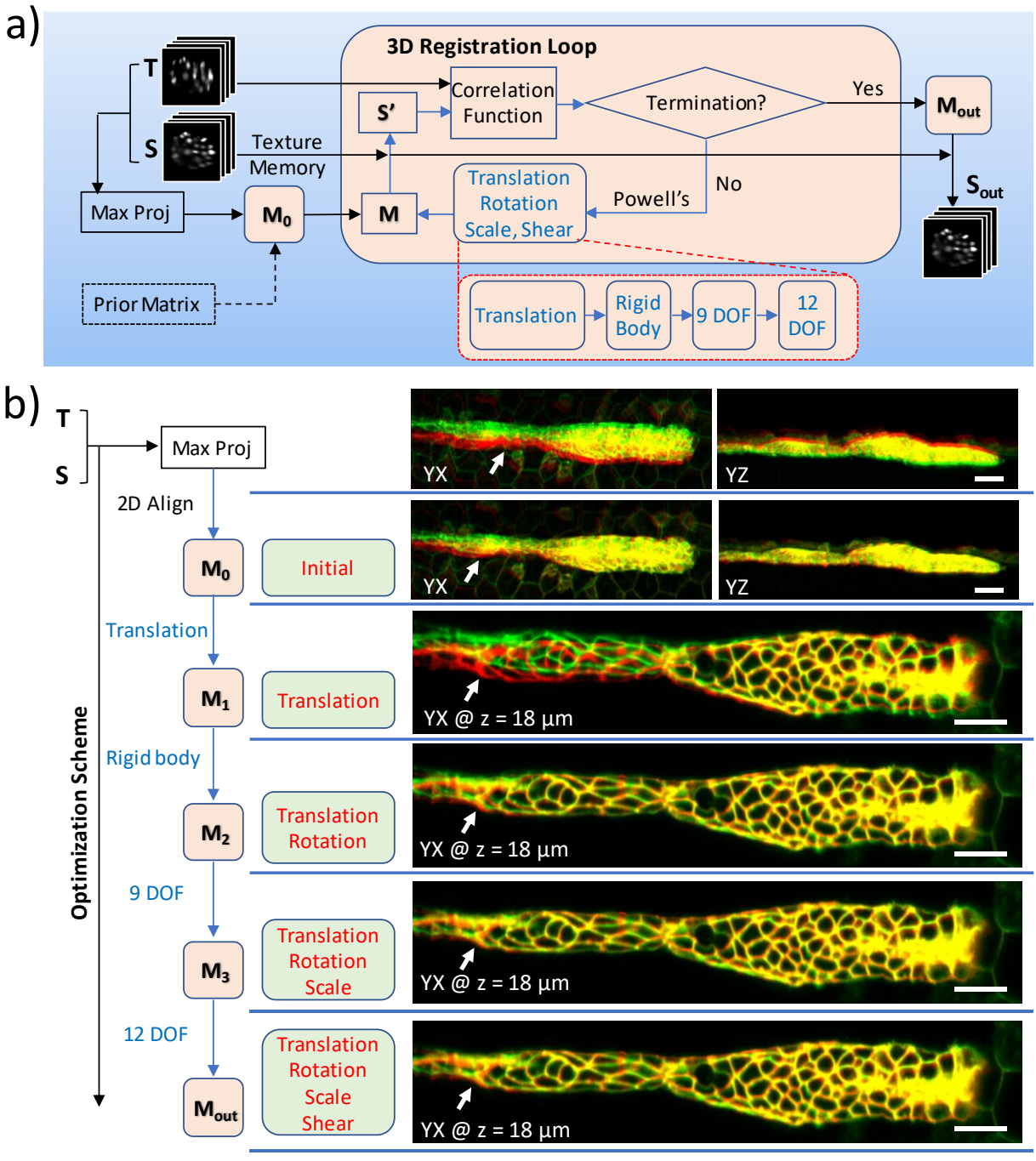

Supplementary Fig. 12, Schematic of GPU-based 3D registration. **a)** The inputs to the registration are usually two 3D images, referred as the source (S, image to be registered) and target image (T, fixed image). The XY and ZY maximum intensity projections of the input 3D images are used for preliminary alignment (only adjusting translation and rotation) and to generate an initial transformation matrix (M_0). Alternatively, a transformation matrix from a prior time point is used as M_0. A 3D registration loop iteratively performs affine transfomations on S (which is kept in GPU texture memory for fast trilinear interpolation) based on the transformation matrix M. The correlation ratio between the transformed source (S') and T is used as the cost function. This cost function is minimized with Powell's method,

updating the transformation matrix by optimizing its four affine tranformation components: translation, rotation, scale and shear. The optimization is performed serially, optimizing translation; translation and rotation (i.e. rigid body registration with 6 degrees of freedom);translation, rotation and scale (9 degrees of freedom) ; and finally translation, rotation, scale and shear (12 degrees of freedom). **b)** Example images of zebrafish embryo expressing Lyn-eGFP (see also **Fig. 2j**) show the iteration optimization scheme and corresponding improvements in registration quality (white arrows). Target images are shown in red, source images in green, and the overlay in yellow. Images in top two rows are maximum intensity projections of lateral (left) and axial (right) views, while images in other rows are single planes from 3D stacks. See **Methods** for further details on this process. Scale bars: 20 μm for all images. Experiments were repeated on similar datasets at least 3 times for **b)**, with similar results obtained each time; representative data from a single experiment are shown.

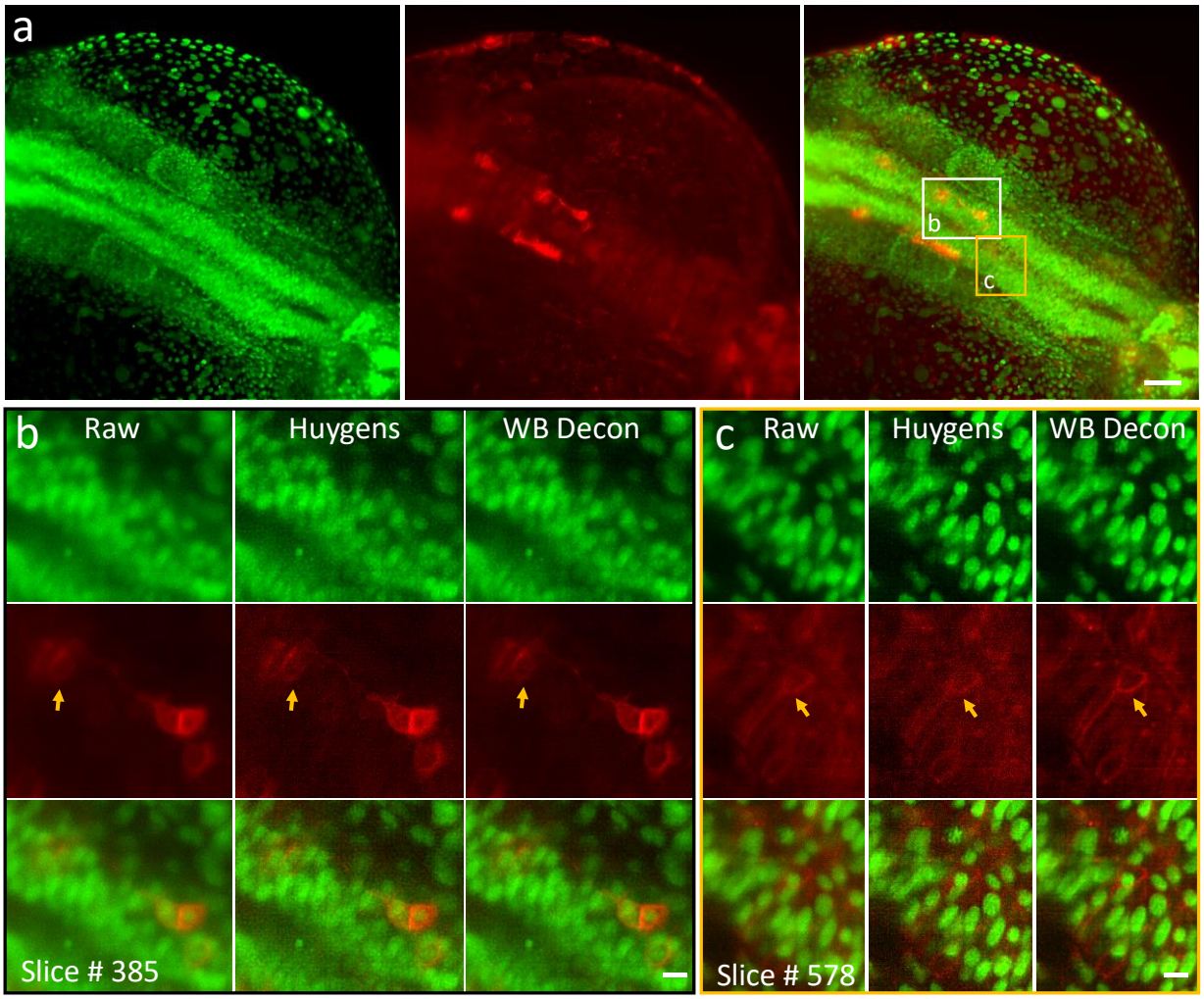

Supplementary Fig. 13, **Wiener-Butterworth (WB) deconvolution improves raw single-view data acquired on Zeiss Z.1 light-sheet microscope and performs favorably against Huygens deconvolution software.** 18 hpf zebrafish embryos were mounted (anterior to bottom right, hindbrain in center of the field of view), imaged, and the images deconvolved with 1 iteration WB deconvolution (**a**). Nuclear (GFP, green), cranial efferent marker (mRFP, red) and merged low magnification views are shown in (**a**). Higher magnification views (**b**, **c**), corresponding to rectangular regions in (**a**) are also shown, comparing raw (left), Huygens (middle), and WB deconvolution (right). Arrows highlight regions of low signal-to-noise ratio that are better revealed with WB deconvolution than Huygens. Scale bars: 50 µm in (**a**); 10 µm in (**b**, **c**). See also **Methods**, **Supplementary Table 3**, **Supplementary Video 10**. Experiments were repeated on similar datasets at least 3 times, with similar results obtained each time; representative data from a single experiment are shown.

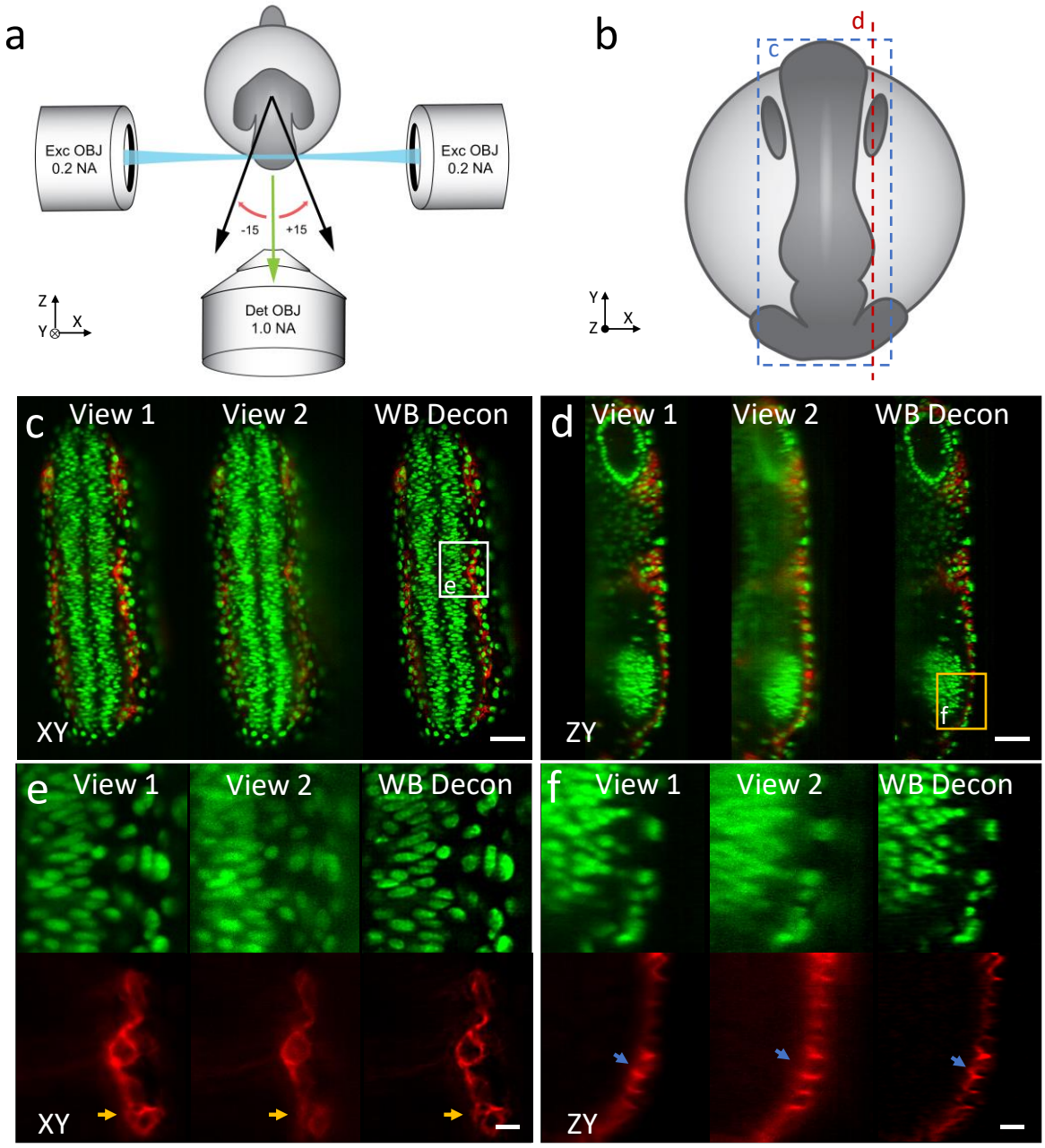

Supplementary Fig 14, Multiview registration and Wiener-Butterworth deconvolution improves contrast and resolution isotropy of raw data acquired on Zeiss Z.1 microscope. 18 hpf zebrafish embryos were mounted and imaged, acquiring two views of the sample ~30 degrees apart (**a**). (**b**) Schematic view of imaged region of embryo. (**c**, **d**) Lateral and axial planes indicated by the blue dashed rectangle and red dashed line in (b) comparing raw views and deconvolved result. Nuclear (green, GFP) and neural crest cell (red, mRFP) morphologies are evident. (e, f) Higher magnification views of rectangular regions in (**c**, **d**), emphasizing improved resolution and contrast in deconvolved result (blue arrows). Scale bars: 50 µm in (**c**, **d**); 10 µm in (**e**, **f**). See also **Supplementary Table 3**. Experiments were repeated on similar datasets at least 3 times, with similar results obtained each time; representative data from a single experiment are shown.

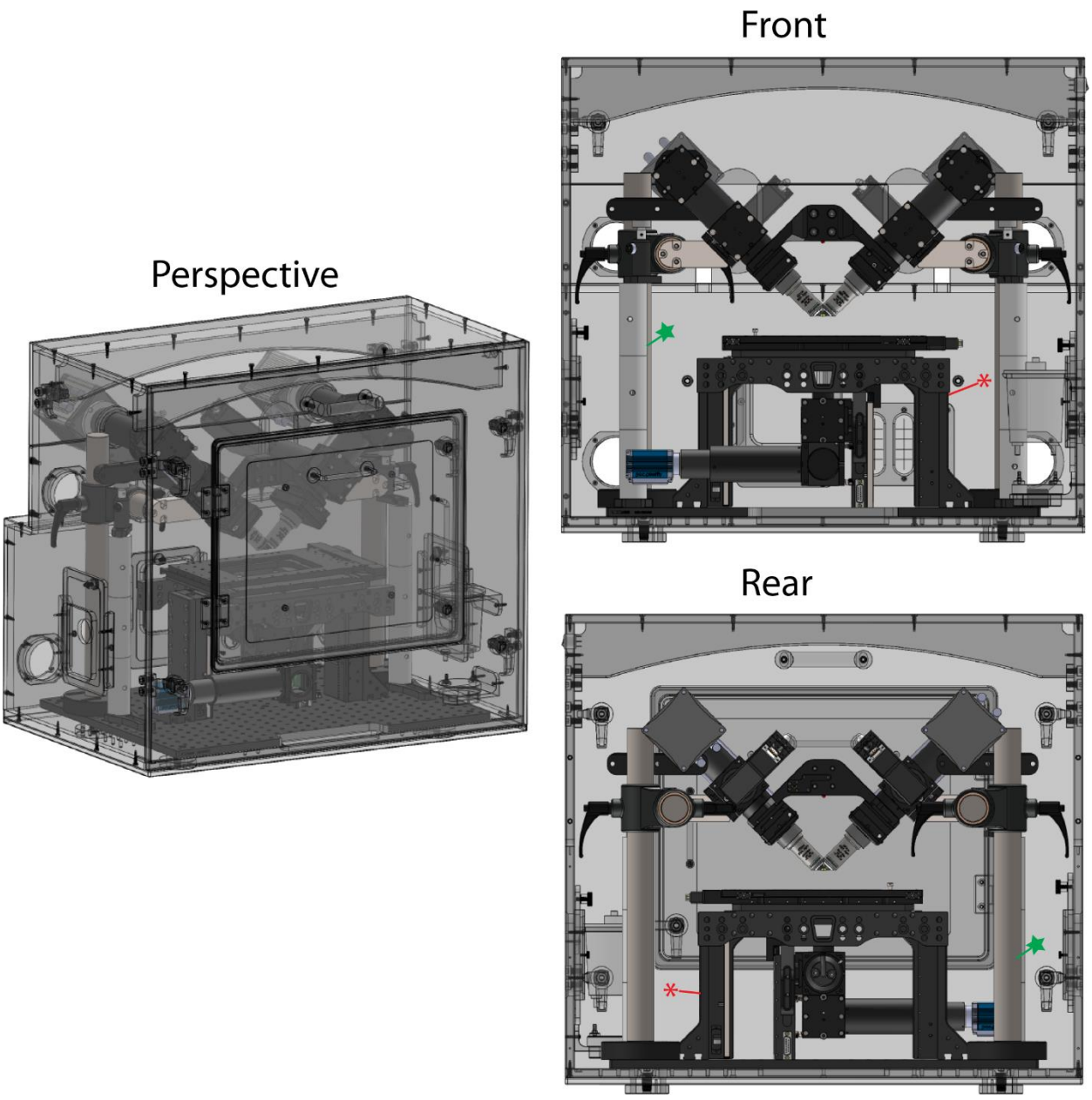

Supplementary Fig. 15, DiSPIM for cleared tissue imaging. Perspective, front, and rear drawings are shown. A substantive change from our previous diSPIM includes a movable 3D sample stage (FTP-2000, indicated with red asterisk), that allows the illumination and detection systems to remain fixed in space, improving imaging of large specimens. Additional changes include post systems (green stars) that support the fixed diSPIM head. The objectives can be easily switched between 40x, 0.8 NA water immersion lenses (shown here) for imaging live, aqueous samples and 17.9x, 0.4 NA multi-immersion lenses for cleared tissue imaging. See **Methods** for further details.

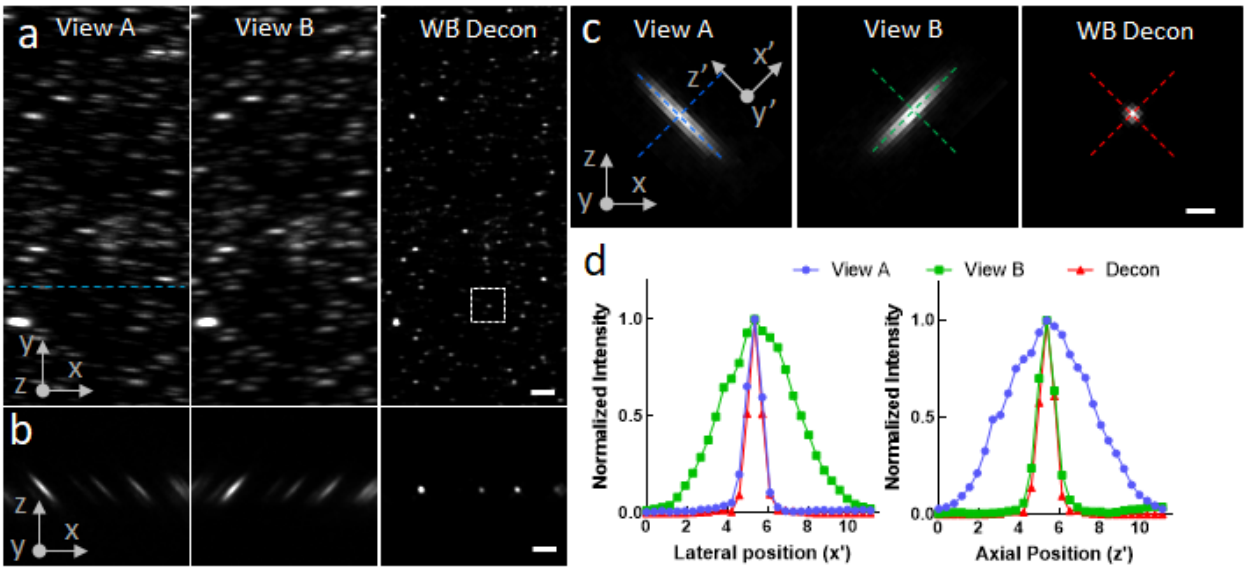

Supplementary Fig. 16, Estimating spatial resolution in the cleared tissue diSPIM. 100 nm yellow-green fluorescent beads were deposited on a coverslip, immersed in dibenzyl ether, and imaged in the cleared-tissue diSPIM. **a)** xy maximum intensity projections corresponding to raw single views and Wiener-Butterworth (1 iteration) deconvolution of registered views. Note that data have been rotated so that x, y are parallel to the plane of the coverslip and z is normal to the coverslip. **b)** Axial plane corresponding to dotted blue line in **a)**. **c)** Higher magnification images of single beads. Primed coordinates are from perspective of light-sheet collection objective. **d)** Lateral and axial profiles as indicated in **c)**. Scale bars: **a), b)** 5 μm, **c)** 2 μm. Experiments were repeated on similar datasets at least 2 times, with similar results obtained each time; representative data from a single experiment are shown.

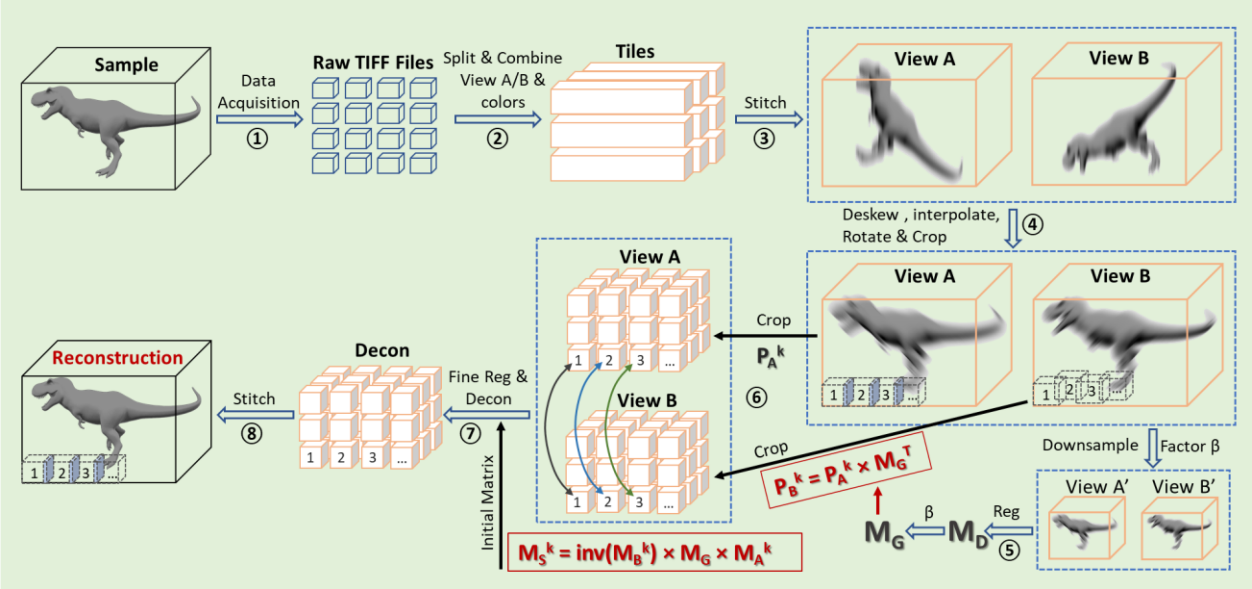

Supplementary Fig. 17, Post-processing pipeline for large, cleared tissue data imaged with diSPIM. Raw data acquired by the cleared-tissue diSPIM are saved as multiple 16-bit TIFF files (each less than or equal to 4 GB, step 1). These files contain mixed information, i.e. colors, views, and spatial locations are saved as they are recorded in the acquisition sequence. The XY slices are re-organized and re-saved as TIFF stacks (each usually a few hundred GB), each corresponding to a distinct spatial tile/color/view (step 2). Tiles for each color/view are then combined (with Imaris Stitcher, BigStitcher or custom stitching software written in MATLAB) to reassemble blurred, images of the sample (View A and View B, step 3), rotated 45 degrees relative to the coverslip. These TIFF stacks at each color and each view are deskewed (transforming from stage-scanning mode to light-sheet scanning mode), interpolated (obtaining isotropic pixel resolution), rotated (transformed from the objective view to the perspective of coverslip), cropped (saving memory), and resaved as TIFF files (e.g. ~ 2 TB for 4 colors/2 views for the dataset shown in **Fig. 3d,** step 4). By down-sampling View A and View B (typically by a factor of 5) to View A' and View B' and registering them, a coarse, global transformation matrix $\mathbf{M_G}$ that maps view B to view A can be calculated based on the registration matrix $\mathbf{M_D}$ that maps view B' to view A' (step 5). The coarsely registered View A and View B are then split into multiple subvolumes (e.g., ~1000 subvolumes, each 640 x 640 x 640 pixels, step 6). Coordinates that define the cropping locations in View B (i.e., $\mathbf{P_B^k}$) can be roughly estimated from the position in the cropped View A (i.e., $\mathbf{P_A^k}$) and the transpose of the coarse, global transformation matrix $\mathbf{M_G}$ (i.e., $\mathbf{M_G^T}$). The index k denotes the index of the subvolume and runs from 1 to the total number of subvolumes. Each of the cropped tiles in View B can be coarsely registered to the corresponding cropped tile in view A with a new matrix $\mathbf{M_S^k}$, derived from the cropping positions ($\mathbf{M_A^k}$, $\mathbf{M_B^k}$) and global transformation matrix $\mathbf{M_G}$. Fine registration and joint Wiener-Butterworth deconvolution are then performed on the paired subvolumes of View A and View B (step 7). Finally, stitching all deconvolved subvolumes results in the final reconstruction (step 8). See **Methods** for further information.

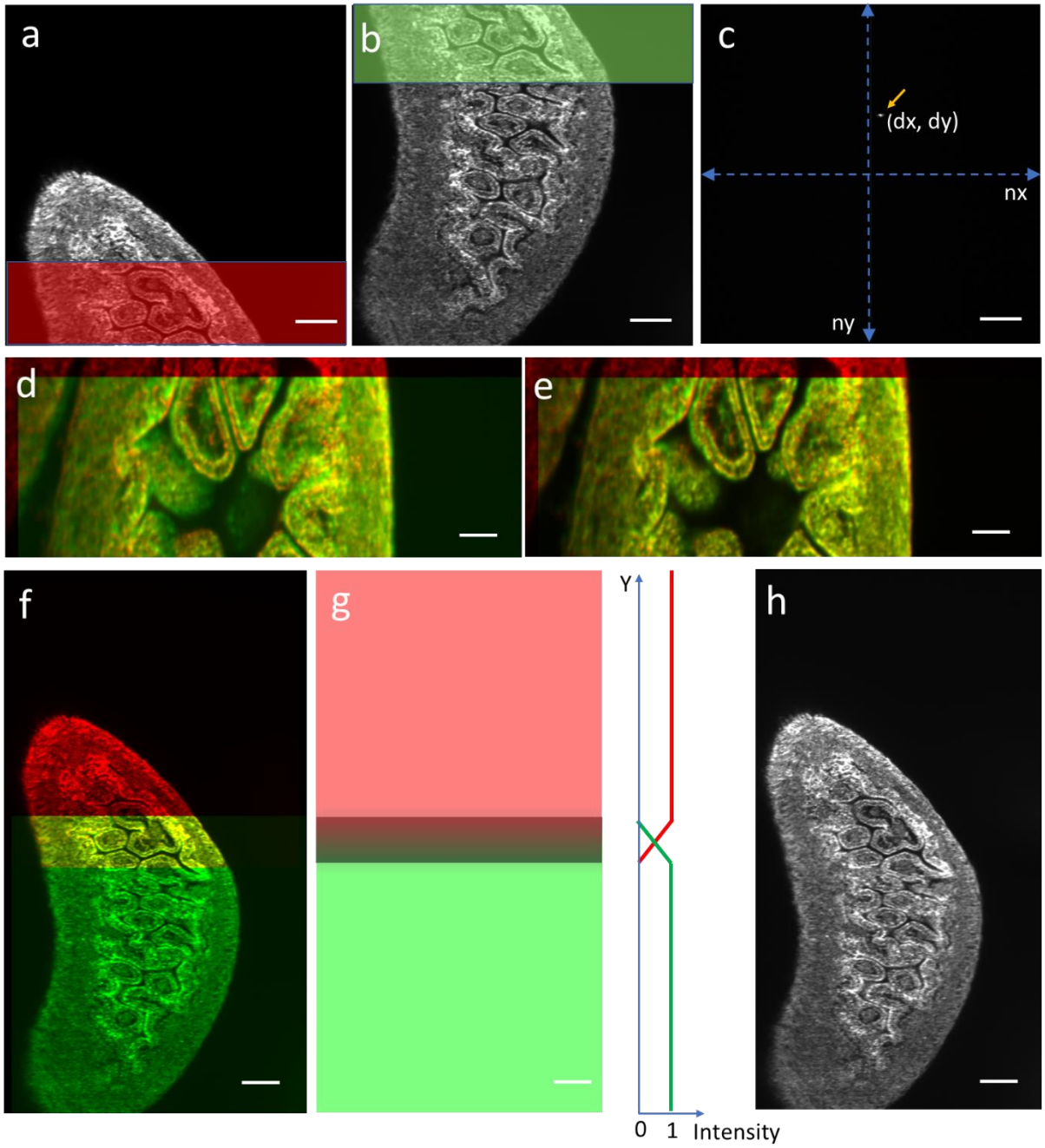

Supplementary Fig. 18, Stitching image tiles with our custom software. (**a**-**b**) An example with two adjacent tiles (XY slices are shown) with overlap along the vertical Y dimension. Green and red shading indicate the regions of overlap. (**c**) The shift image obtained by computing the Fourier-based phase correlation between the two tiles. The location of the peak indicated by the arrow provides information on possible shifts between the two tiles. Possible shifts are given by the location of the peak relative to the center of the image (located at the intersection of the two dashed lines) denoted (dx, dy), and locations in the other three quadrants (dx, dy - ny), (dx - nx, dy), (dx - nx, dy - ny), where nx and ny are the maximum pixel values along the x and y dimensions, respectively. Note that for 3D stacks there are $2^3 = 8$ possibilities. (**d**) The two tiles are shifted according to each candidate shift, the overlapping regions cropped, and the normalized cross-correlation (NCC) for the cropped regions computed. The shift with

the highest NCC is the correct candidate. In this example, (dx, dy - ny) leads to the highest NCC of 0.83, which is applied to yield the coarsely overlapped region in yellow. Note that the top tile (**a**) is pseudo-colored in red, and the bottom tile (**b**) is pseudo-colored in green. (**e**) The cropped tiles are further finely registered with our GPU-based registration method for computing sub-pixel shifts, resulting in an NCC of 0.95. (**f**) Overlap of the two tiles after sub-pixel shifting is applied. (**g**) Weight images for the corresponding tiles. The intensity is one except in the overlap region, in which the weight of the top tile is linearly decreased from 1 to 0, and the weight of the bottom tile is linearly increased from 0 to 1. (**h**) Merged image after linear blending the two tiles by multiplying them with the weight images and then summing the resulted weighed images together. Scale bars: 50 μm in (**a**-**c**), 30 μm in (**d**-**e**), and 100 μm in (**f**-**h**).

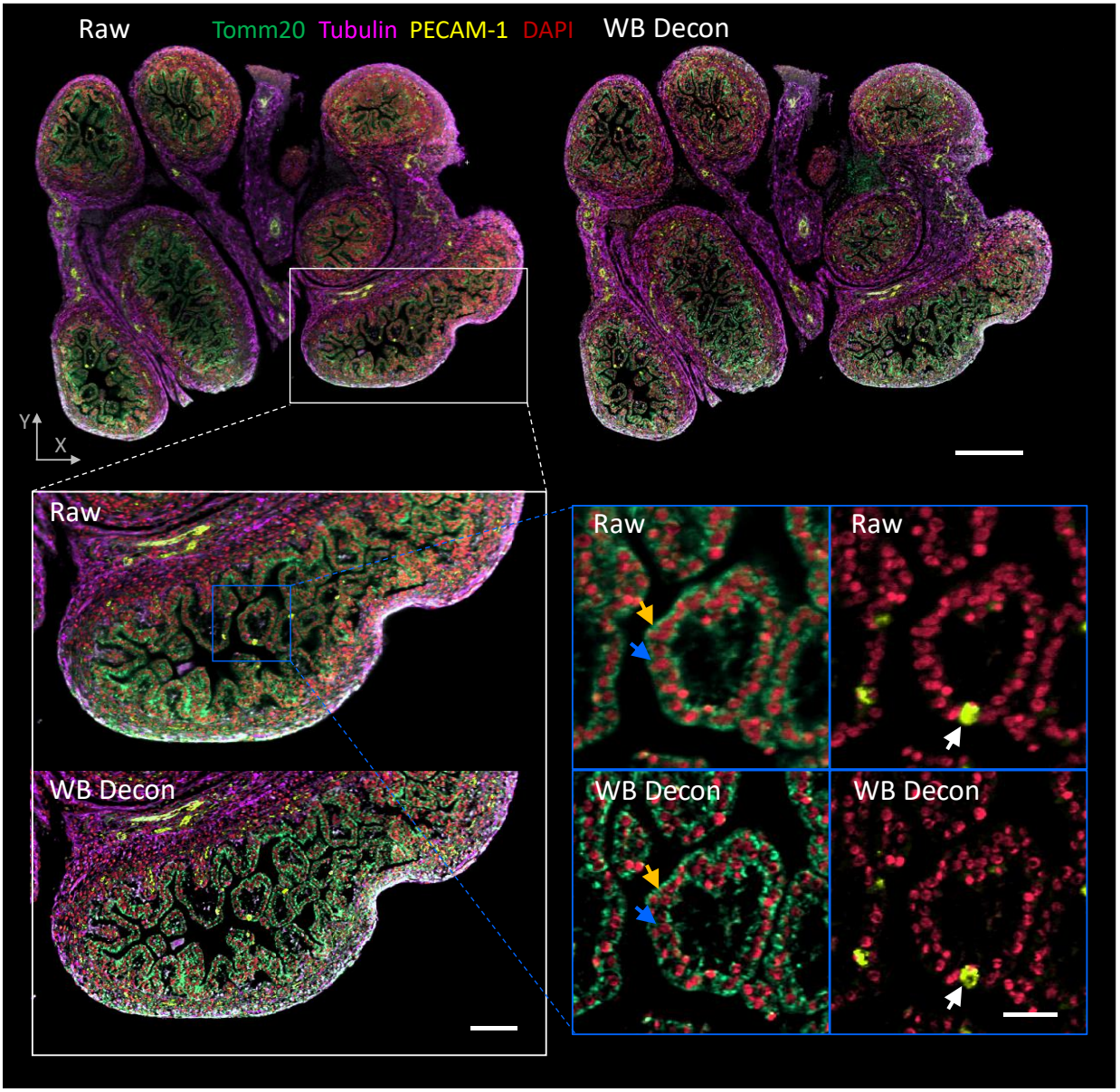

Supplementary Fig. 19, Dual-view Wiener-Butterworth (WB) deconvolution reveals more detail than single-view imaging. The single plane shown in **Fig. 3d** is reproduced, comparing raw single-view data versus WB deconvolution, at progressively higher levels of magnification. The increased detail evident in the deconvolved results are especially evident at the highest level of magnification, where nuclei (blue, yellow arrows) and the hollow interior of blood vessels (white arrows) are revealed in the WB deconvolution but not in raw data. Scale bars are at progressive levels of magnification: 300 μm, 100 μm, and 30 μm. Experiments were repeated on similar datasets at least 3 times, with similar results obtained each time; representative data from a single experiment are shown.

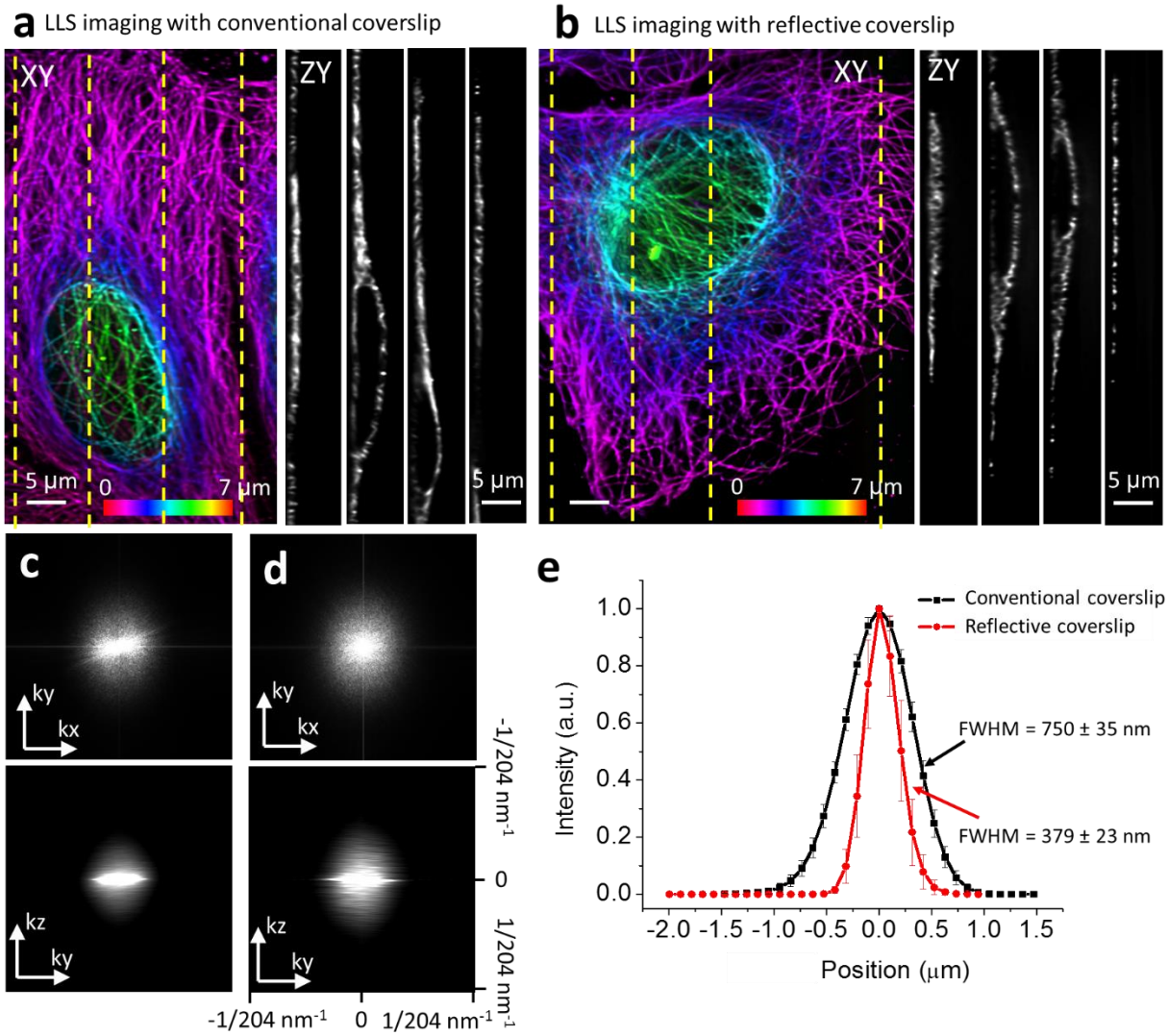

Supplementary Figure 20, Reflective lattice light-sheet (LLS) imaging improves axial resolution. Lateral maximum intensity projections (axial depth from coverslip indicated with color bar) derived from 3D LLS microscopy of Alexa Fluor 488 immunolabeled microtubules in fixed U2OS cells on **(a)** conventional glass and **(b)** reflective coverslip. Reconstructions were performed using traditional deconvolution with a spatially varying PSF. Axial slices (right columns) correspond to the yellow dotted lines in each panel. **(c-d)** Lateral and axial optical transfer functions (OTFs) of the images shown in a) and b), respectively. Note that the displayed OTFs were computed by averaging the 2D OTFs over all slices in the stack. Coordinates are defined from the perspective of coverslip (i.e. z is normal to the coverslip surface, xy are parallel to the coverslip surface). **(e)** The axial profiles derived from **n =** 10 microtubule filaments. Means and standard deviations (bars) in the plots are shown. Experiments were repeated on similar datasets at least 2 times for **a)-d)**, with similar results obtained each time; representative data from a single experiment are shown.

Supplementary Table 1, MSE and SSIM analysis for deconvolution with Traditional, Gaussian, Butterworth and Wiener-Butterworth back projectors, on spherical phantoms presented in Supplementary Figure 6.

SNR		**3.2**	**24**
MSE	Traditional	0.0045	0.0014
	Gaussian	0.0047	0.0015
	Butterworth	0.0044	0.0016
	Wiener-Butterworth	0.0038	0.0012
SSIM	Traditional	0.7829	0.9147
	Gaussian	0.7719	0.9128
	Butterworth	0.7943	0.9054
	Wiener-Butterworth	0.8364	0.9363

SNR: signal-to-noise ratio; MSE: mean squared error; SSIM: structural similarity index; See **Supplementary Note 4** for detailed definitions of these quantities. All calculations are based on ground truth spherical phantoms. All back projectors produce similar results, although the Wiener-Butterworth back projector produces the best results as indicated by the smallest MSE value and largest SSIM value.

Supplementary Table 2, MSE and SSIM evaluation for deconvolution results of experimental datasets based on Gaussian, Butterworth and Wiener-Butterworth back projectors.

Samples		**U2OS cells Mitochondria**	**U2OS cells Microtubule**	***C. elegans* embryo nuclei**	**U2OS cells actin**	***C. elegans* embryo nuclei**
Figures/Videos		Fig. 1 f	Sup. Fig. 7a	Sup. Fig. 7b	Sup. Fig. 7c	Sup. Fig. 8
Microscope		iSIM	Confocal	iSPIM	Widefield	diSPIM
MSE	Gaussian	5.71e-6	4.80e-5	4.67e-6	2.23e-4	2.40e-6
	Butterworth	3.21e-5	8.73e-5	1.30e-5	2.38e-4	1.61e-5
	Wiener-Butterworth	1.11e-4	7.81e-4	3.99e-5	7.68e-5	1.04e-4
SSIM	Gaussian	0.9978	0.9979	0.998	0.8418	0.999
	Butterworth	0.9883	0.9964	0.996	0.8342	0.9932
	Wiener-Butterworth	0.9629	0.9594	0.9889	0.9447	0.9612

MSE: mean squared error; SSIM: structural similarity index; See **Supplementary Note 4** for detailed definitions of these quantities. All calculations are based on using the deconvolution results from the traditional RL back projector as ground truth. Note the close correspondence between ground truth and deconvolution using other back projectors, indicated by the small values of MSE and high values of SSIM.

Supplementary Table 3, Data acquisition and processing details for data shown in Figs. 1, 2, and associated Supplementary Figures

Samples		Fixed U2OS mitochondria	Live U2OS ER	Fixed U2OS microtubule	Fixed U2OS actin	*C. elegans* embryo nuclei		*C. elegans* embryo neuron/nuclei	Jurkat T cell actin	Zebrafish embryo	Zebrafish embryo	
Figures/Videos		Fig. 1 e,f Sup. Fig. 4	Sup. Video 3	Sup. Fig. 7a	Sup. Fig. 5c, 7c	Sup. Fig. 7b	Sup. Fig. 8	Fig. 2 a, b, c, d Sup. Video 4, 5	Fig. 2 e, f, g Sup. Video 6	Fig. 2 j-p Sup. Video 7-9	Sup. Fig. 13 Sup. Video 10	Sup. Fig. 14
Fluorescence Label		Alexa-488	ERmoxGFP	Microtubule-561	Alexa-488	GFP-histone		GFP-membrane, mCherry-histone	GFP-Actin	Lyn-eGFP	GFP-histone, mRFP-cranial efferent/neural crest	
Microscope		iSIM	iSIM	Confocal	Widefield	diSPIM (iSPIM)		diSPIM	quad-view light-sheet	diSPIM	Zeiss Lightsheet Z.1	
View number		1	1	1	1	1	2	2	4	2	1	2
Color number		1	1	1	1	1		2	1	1	2	
Acquisition	Excitation	488	488	561	XT 640-W	488		488, 561	488	488	488, 561	
	Step size x Slices per view per color	0.1 µm x 95 slices	0.5 µm x 6 slices	0.5 µm x 6 slices	0.15 µm x 77 slices	1 µm x 40 slices		1 µm x 50 slices	1 µm x 60 slices	1 µm x 80 slices	0.427 µm x 600 slices	0.430 µm x 415 slices
	Acquisition time / tp	5 s	0.3 s	332 s	1.8 s	0.5 s		1 s	3.2 s	3.5 s	12 s	24
	Time interval	--	2 s	--	--	60 s		100 s	15 s	30 s	120 s	300 s
	Total time points	1	150	1	1	780		50	30	902	36	35
	Total acquisition time	5 s	300 s	332 s	1.8 s	780 min		83 min	450 s	7.5 h	72 min	175 min
Image size (each volume after interpolation)		1920 x 1550 x 95	1920 x 1550 x 6	1024 x 1024 x 22	512 x 512 x 77	240 x 360 x 246		280 x 380 x 308	360 x 338 x 181	640 x 2048 x 496	1280 x 1280 x 600	1280 x 1280 x 415
Total data size		270 M voxels, 539 MB, 16 bit	2.5 G voxels, 5.1 GB, 16 bit	22 M voxels, 44 MB, 16 bit	19 M voxels, 39 MB, 16 bit	20M voxels, 41MB,16 bit	16.1G voxels, 31.2GB,16 bit	6.1 G voxels, 12.2 GB, 16 bit	2.5 G voxels, 5 GB, 16 bit	1.05 T voxels, 2.1 TB, 16 bit	65 G voxels, 121 GB, 16 bit	88 G voxels, 177 GB, 16 bit
Data processing	Registration time / tp	--	--	--	--	--	1.9 s	6.26 s	16 s	13.4 s	--	36 s
	Deconvolution time / tp	2.9 s	0.21 s	0.29 s	0.27 s	0.29 s	0.11 s	0.16 s	8.4 s	0.6 s	14.5 s * (128 s for Huygens)	26 s
	File IO / tp	10.6 s	1.2 s	1.2 s	1.0 s	1.0 s	0.52 s	1.38 s	6.4 s	0.82 s	17 s	32 s
	Total time / tp	13.5 s	1.4 s	1.5 s	1.3 s	1.3 s	2.5 s	7.8 s	30. 8 s	14.8 s	31.5 s	94 s
	Total processing time	13.5 s	211 s	1.5 s	1.3 s	1.3 s	33 min	390 s	7.7 h	445 s	19 min	1.8 h

The registration and deconvolution for all datasets use our new methods (faster registration, Wiener-Butterworth deconvolution) with GPU implementation on an NVIDIA Quadro M6000 card except for the single view Zebrafish embryo dataset acquired with the Zeiss Z.1 light-sheet microscope. For this dataset, Wiener-Butterworth (indicated by *) and Huygens deconvolution methods were compared using an NVIDIA Quadro RTX6000. tp: time point.

Supplementary Table 4, Comparing the performance of different registration methods on time-lapse diSPIM datasets.

Samples			***C. elegans* embryo nuclei**		**Zebrafish embryo**	
Figures			Sup. Fig. 8		Fig. 2 j-p	
Image Size			240 x 360 x 246, 41 MB, 16 bit		640 x 2048 x 496, 1.2 GB, 16 bit	
Total Time Point			780		902	
Total Data Size			31.2 GB, 16 bit		2.1 TB, 16 bit	
Time Cost			Single Time point	Time series	Single Time point	Time series
	MIPAV	CPU	380 s/tp	366 s/tp	2.1 hr/tp	2.0 hr/tp *
	Niftyreg	CPU	405 s/tp	324 s/tp *	2.8 hr/tp	2.6 hr/tp *
	Elastix	CPU	53 s/tp	58 s/tp	219 s/tp	201 s/tp
	Elastix	GPU	52 s/tp	55 s/tp	211 s/tp	186 s/tp
	Our method	GPU	6.1 s/tp	1.9 s/tp	55 s/tp	16 s/tp
MSE	Niftyreg	CPU	2.7e-04		9.5e-05	
	Elastix	CPU	3.8e-05		1.2e-05	
	Elastix	GPU	3.8e-05		1.2e-05	
	Our method	GPU	2.0e-04		3.1e-05	
SSIM	Niftyreg	CPU	0.9588		0.7272	
	Elastix	CPU	0.9932		0.9842	
	Elastix	GPU	0.9932		0.9842	
	Our method	GPU	0.9711		0.9617	

MSE: mean squared error; SSIM: structural similarity index; See **Supplementary Note 4** for detailed definitions of these quantities; s/tp: second per time point; hr/tp: hour per time point; *: estimated by 10 time points. MSE and SSIM are calculated based on assuming the registration results from MIPAV are ground truth. All registrations were performed on the same computer, equipped with an NVIDIA Quadro M6000 card. The NiftyReg provides both CPU and GPU implementations, but we found the GPU implementation failed to correctly register the two datasets (i.e., generated unacceptable artifacts for the *C. elegans* embryo nuclei dataset and encountered CUDA errors for the zebrafish embryo dataset, probably due to the large data size), so only the results obtained via the CPU implementation are reported.

Supplementary Table 5, Sample preparation, data acquisition and processing details for all cleared tissue datasets

Samples		Adult mouse brain	Embryonic mouse intestine	Adult mouse intestine	Embryonic mouse stomach	Adult mouse ovary
Figures/Videos in paper		Fig. 3 a, b, c Sup. Video 11	Fig. 3 d Sup. Fig. 19, Sup. Video 12	Sup. Video 13	Sup. Video 14	Sup. Video 15
Size	Physical Size	4 x 2 x 0.5 mm^3	2.1 x 2.5 x 1.5 mm^3	2.3 x 0.7 x 0.5 mm^3	2.4 x 2.7 x 1.0 mm^3	2.6 x 1.9 x 0.5 mm^3
	Number of colors	1	4	2	2	2
	Digital Size, voxels (X x Y x Z x color)	10280 x 5160 x 1400 x 1	5586 x 6500 x 3930 x 4	6221 x 2008 x 1516 x 2	6370 x 7226 x 2850 x 2	6820 x 6100 x 1460 x 2
Sample Preparation	Primary antibody	Rabbit anti-RFP	Mouse anti-α-Tubulin, Rabbit anti-Tomm20, Goat anti-PECAM-1	Goat anti-PECAM-1	Mouse anti αTubulin, Goat anti-PECAM-1	Mouse anti-CD11c (Integrin aX), Rat anti CD11b
	Secondary antibody	Goat anti-Rabbit IgG(H+L) Alexa-555	Donkey anti-Goat Alexa-488, Donkey anti-Mouse Alexa-568, Donkey anti-Rabbit Alexa-647, DAPI (dye)	Donkey anti-Goat Alexa-488	Donkey anti-Mouse Alexa-568, Donkey anti-Goat Alexa-647	Goat anti-Mouse IgG1 Alexa-488, Donkey anti-Rat CF-568
	Chemical Reagent	TritonX, Dichloromethane (DCM), Dibenzyl Ether (DBE), Tetrahydrofuran (THF), Methanol, Hydrogen Peroxide, Krazy Glue, Glass slide				
Acquisition	Views	2	2	2	2	2
	Excitation Lasers	488	405, 488, 561,637	405, 488	561, 637	488, 561
	Camera ROI (slice size)	2048 x 2048	2048 x 2048	2048 x 2048	2048 x 2048	2048 x 2048
	Tile number (y x z)	3 x 1	3 x 3	1 x 1	4 x 2	3 x 1
	step size x Slices (view/color/tile)	2 µm x 1600 slices	2 µm x 1300 slices	1 µm x 2200 slices	2 µm x 1200 slices	2 µm x 1300 slices

	exposure time / slice		5 ms	10 ms	5 ms	10 ms	10 ms
	acquisition time / tile		51 s	239 s	220 s	104 s	109 s
	Total acquisition Time (Step 1)		154 s	36 min	220 s	832 s	327 s
Post processing and time cost	Step 2	File I/O, splitting	0.5 h	2.5 h	0.3 h	1.2 h	0.8 h
	Step 3 (Imaris Stitcher)	File converting	1.6 h	4.8 h	NA	2.4 h	2 h
		Stitching	0.2 h	0.8 h	NA	0.4 h	0.4 h
		File I/O and converting	2.5 h	30 h	NA	14 h	8.1 h
	Step 3 (ImageJ BigStitcher)	Stitching and File I/O	0.8 h	7.0 h	NA	3.4 h	1.2 h
	Step 3 (MATLAB Stitcher)	Stitching and File I/O	0.6 h	2.7 h	NA	2.7 h	1.0 h
	Step 4	File I/O, deskew, interpolation, rotation	4 h	24 h	2.2 h	11 h	6.6 h
	Step 5	Coarse reg	0.1 h	0.2 h	0.1 h	0.2 h	0.2 h
	Step 6	Cropping subvolumes	3.5 h	24 h	1.4 h	12 h	5.4 h
	Step 7	Fine Reg / Decon	3.4 h	24 h	1.4 h	12 h	5.3 h
	Step 8	Stitching	5 h	30 h	2.8 h	12 h	10 h
	Total time (with Imaris Stitcher)*		21 h	140 h	8.2 h	65 h	39 h

Overlap was in the 10-20% range in y and z for all tiling experiments, where y is defined as the lateral direction that points towards the front of the microscope and z is defined perpendicular to the coverslip. The total acquisition time is computed by multiplying the acquisition time cost for each tile by the number of tiles. This omits the time cost for moving between tiles. Since moving between tiles was done manually, we estimate an additional time cost of ~30 s per tile. This timing is negligible compared to the total acquisition time we report, and we note that it could be significantly reduced by using the microscope control software (µManager) to perform multi-tile acquisition, a capability that exists within the software. *'Total time' values are based on the Imaris Stitcher values; during the revision process of the manuscript we investigated the use of our own MATLAB-based Stitcher and BigStitcher which are both substantially faster than Imaris Stitcher. Please also see accompanying schematic, **Supplementary Fig. 17**.

Supplementary Table 6, Antibodies and reagents for cleared tissue preparation

Primary antibody			
Name	**Vendor**	**Catalog**	**Related Samples**
Rabbit anti-RFP	Rockland	600-401-379	adult mouse brain
Mouse anti-α-Tubulin	Thermo Fisher Scientific	322500	embryonic mouse stomach, embryonic mouse intestine
Rabbit anti-Tomm20	Abcam	ab78547	adult mouse intestine
Goat anti-PECAM-1	R&D Systems	AF3628	embryonic mouse stomach, embryonic mouse intestine, adult mouse intestine
Mouse anti-CD11c (Integrin αX)	Santa Cruz	sc-398708	adult mouse ovary
Rat anti-CD11b	R&D Systems	MAB1124	adult mouse ovary
Secondary antibody/counter stain			
Name	**Vendor**	**Catalog**	**Related Samples**
Goat anti-Rabbit IgG (H+L) Alexa-555	Invitrogen	A27039	adult mouse brain
Donkey anti-Goat IgG (H+L) AffiniPure F(ab')$_2$ Fragment Alexa-488	Jackson ImmunoResearch	705-546-147	embryonic mouse intestine, adult mouse intestine
Goat anti-Mouse IgG1 Alexa-488	Thermo Fisher Scientific	A21121	adult mouse ovary
Donkey anti-Rat IgG (H+L) CF-568	Sigma	SAB-4600077	adult mouse ovary
Donkey anti-Mouse IgG (H+L) Alexa-568	Thermo Fisher Scientific	A10037	embryonic mouse stomach, embryonic mouse intestine
Donkey anti Rabbit IgG (H+L) AffiniPure F(ab')$_2$ Alexa-647	Jackson ImmunoResearch	711-606-152	embryonic mouse intestine
Donkey anti-Goat IgG(H+L) Alexa-Plus-647	Thermo Fisher Scientific	A32849	embryonic mouse stomach
DAPI	Thermo Fisher Scientific	D1306	embryonic mouse intestine
Chemical Reagent			
Name	**Vendor**	**Catalog**	**Purpose**
TritonX	Sigma	T9284	stain/wash buffer
Dichloromethane (DCM)	Sigma	270997	Delipidation
Dibenzyl Ether (DBE)	Sigma	108014	Clearing
Tetrahydrofuran (THF)	Sigma	186562	Dehydration
Methanol	Sigma	179957	Pre-treatment
Hydrogen Peroxide	Sigma	H1009	Bleaching
Krazy Glue	krazyglue.com (Elmer's Products)	KG385	Sample mounting
Glass slide	Globe Scientific Inc.	1380-20	Sample mounting

Supplementary Table 7, Data acquisition and processing details for data imaged with reflective diSPIM and reflective LLS presented in Fig. 4

Samples		***C. elegans* embryos expressing GCaMP3**	**U2OS cells expressing mEmerald-α-Actinin**
Figures/Videos		Fig. 4 c Sup. Video 16	Fig. 4f Sup. Video 17
Microscope		Reflective diSPIM	Reflective LLS
View number		2 normal views 2 mirror view	1 normal view 1 mirror view
Color number		1	1
Acquisition	Slices per view	60	300
	Exposure per slice	5 ms	8 ms
	Axial step size	1 μm	0.4 μm
	acquisition time (each time point, all views)	0.3 s	2.4 s
	time interval	0.35 s	2.5 s
	total time points	155	100
	total acquisition time	~54 s	~250 s
Image size (after interpolation)		360 x 310 x 360 x 2	425 x 540 x 256 x 2
Total data size		12.5 G voxels, 25 GB, 16 bit	12 G voxels, 24 GB, 16 bit
Data processing (registration /deconvolution)	Registration time (each time point)	10.6 min @ CPU 6.8 s @ GPU	16 min @ CPU 12 s @ GPU
	Deconvolution time (each time point)	14 min @ Trad Decon 1.4 min @ WB Decon	2 h @ Trad Decon 8 min @ WB Decon
	total deconvolution time (all time points)	36 h @ Trad Decon 3.6 h @ WB Decon	8.3 day @ Trad Decon 13.3 h @ WB Decon
	Deep learning training volumes	100	80
Data processing (deep learning)	Deep learning training time	10.8 h	8.2 h
	Deep learning validation time	1.68 s	2 s
	Total processing time for (all time points)	260 s	200 s

Supplementary Note 1, Using an unmatched projector/back projector

We can represent a general, linear shift-invariant imaging model by a linear system of equations

$$\boldsymbol{i} = F\boldsymbol{e}, \tag{1}$$

where the vector $\boldsymbol{i}$ represents the measured image data, the vector $\boldsymbol{e}$ represents the desired deconvolved estimate image, and the matrix F represents convolution with a point spread function f. If the 1D image vectors are formed by concatenating the rows of the images into single column vectors, then the matrix F is very structured: it is block circulant with circulant blocks (BCCB).

The modified Richardson-Lucy algorithm

$$e_{k+1} = e_k \{\left[\frac{i}{e_k * f}\right] * b\} \tag{2}$$

iteratively updates the estimate of the deconvolved image by comparing the convolution of that estimate with the measured image *i* and convolving their ratio with a "back projection" kernel *b* to determine a multiplicative correction factor.

Equation (2) can be recast in this matrix-vector notation using

$$e_{k+1} = e_k \{B\left[\frac{i}{Fe_k}\right]\}, \tag{3}$$

where the division operation in square brackets is performed elementwise and the backprojection matrix B implements convolution with a backprojection kernel b. The matrix B is also BCCB. Note that this form of the R-L equation without normalizing prefactors assumes the PSF f and backprojection kernel b are both normalized to sum to one, which preserves counts across iterations. The standard R-L equation would set $B = F^T$, where T denotes transpose, which corresponds to convolution with a flipped version of the PSF f (or equivalently to convolution with the PSF f itself if f is symmetric).

In the context of image reconstruction in medical imaging, where the R-L algorithm is widely used under the name Maximum Likelihood Expectation Maximization (MLEM), Zeng and Gullberg showed that the R-L algorithm can be accelerated through careful choice of the backprojection matrix B[1]. Specifically, the R-L algorithm was shown to move more rapidly toward desirable reconstructed images when the eigenvalue spectrum of the matrix product BF is flatter (i.e., the eigenvalues cluster closely together). Zeng and Gullberg discuss additional constraints on the back projector B that guarantee convergence to the same solution as when using the traditional matched back projector $B = F^T$. However, these constraints are mainly important for the additional class of Landweber iterations they study. R-L algorithms are rarely run to convergence since that yields unacceptably noisy solutions. Moreover, as in Zeng and Gullberg, we truncate any negatives that arise in the modified R-L iteration at each iteration, a step that invalidates any analysis based on these convergence constraints.

Thus, the key result from Zeng and Gullberg that we invoke (and validate) in this paper is that deconvolution can be accelerated by choosing the backprojection matrix B such that the eigenvalue spectrum of the matrix product BF is as flat as possible.

It is straightforward to determine the eigenvalue spectrum of BF. Both B and F are BCCB and circulant matrices can be diagonalized by the discrete Fourier transform (DFT) matrix:

$$B = QD_BQ^{\dagger}, \tag{4}$$

where Q is a matrix representing application of the DFT and $Q^\dagger$ is its conjugate transpose[2]. D_B is a diagonal matrix whose diagonal elements are given by the Fourier transform of the backprojection kernel b. These diagonal elements are also the eigenvalues of B. Thus

$$D_B = \mathrm{Diag}[\mathrm{DFT}(b)], \tag{5}$$

where the elements of $\mathrm{DFT(b)}$ are appropriately organized into a 1D vector. This is a formal way of expressing the well-known fact that convolution in the spatial domain is equivalent to multiplication in the Fourier domain.

Likewise, for the forward projection matrix F we have

$$F = QD_FQ^\dagger, \tag{6}$$

where

$$D_F = \mathrm{Diag}[\mathrm{DFT}(f)]. \tag{7}$$

Note that the DFT of the system PSF is the system optical transfer function (OTF). I.e,

$$OTF_f \equiv \mathrm{DFT}(f). \tag{8}$$

The product BF is thus given by

$$BF = QD_BQ^\dagger QD_FQ^\dagger. \tag{9}$$

Invoking the fact that the DFT matrix is unitary, i.e., $QQ^\dagger = Q^\dagger Q = I$, we have

$$BF = QD_BD_FQ^\dagger. \tag{10}$$

We see that BF is also a circulant matrix since it is diagonalized by the DFT and that its eigenvalue spectrum is given by the product of the diagonal matrices D_BD_F. Thus, the eigenvalue spectrum of BF is given by the product $\mathrm{DFT}(b)\mathrm{DFT}(f)$, the elementwise product of the DFTs of the kernels used in the forward and back projector steps of the algorithm.

Let's consider a few cases:

1. In the usual case with a symmetric PSF and matched back projector, we have $B = F^T = F$ and so the eigenvalues of BF will be given by $[\mathrm{DFT}(f)]^2 = OTF_f^2$, the squared OTF of the system. This is not especially flat.
2. In previous efforts to accelerate R-L based deconvolution[3], the kernel b has been constructed in such a way that it is narrower than the kernel f. For Gaussian-like kernels, this makes $\mathrm{DFT}(b)$ broader and higher than $\mathrm{DFT}(f)$ and thus $\mathrm{DFT}(b)\mathrm{DFT}(f) > [\mathrm{DFT}(f)]^2$. This gives a flatter eigenvalue spectrum than in case 1, consistent with the finding of faster production of the resolution-limited result.
3. The flattest possible eigenvalue spectrum for BF would be obtained if $\mathrm{DFT}(b) \sim \frac{1}{\mathrm{DFT}(f)} = \frac{1}{\mathrm{OTF_f}}$. This implies we should construct the backprojection kernel b such that the inverse of its DFT approximates the system OTF. Obviously OTF_f goes to zero or falls below the noise floor at some point for most PSFs f, but this suggests using a kernel corresponding to an inverse OTF filter with appropriate apodization. This is the basis for the Wiener-Butterworth kernel studied in this paper.

1 Zeng, G. L. & Gullberg, G. T. Unmatched Projector/Backprojector Pairs in an Iterative Reconstruction Algorithm. *IEEE Trans Med Imaging* **19**, 548-555 (2000).
2 Hunt, B. R. The application of constrained least squares estimation to image restoration by digital computers. *IEEE Trans. Comp.* **22**, 805-812 (1973).
3 Preibisch, S. *et al.* Efficient Bayesian-based multiview deconvolution. *Nat Methods* **11**, 645-648 (2014).

Supplementary Note 2, Generating unmatched back projectors

Supplementary Note 1 discusses how acceleration of the R-L algorithm can be achieved by using an unmatched back projector that provides a flatter product of the Fourier transforms of forward and backwards projectors, $|DFT(b)DFT(f)|$. This section describes how we create such unmatched back projectors, including the Gaussian back projector, Butterworth back projector and Wiener-Butterworth back projector. We also provide the parameters that we use in implementing these filters in our manuscript. Consider a fixed coordinate system (x, y, z) in 3-dimensional (3D) space and the corresponding spatial frequency coordinate system (k_x, k_y, k_z) in the 3D Fourier domain. For simplicity, we will also assume the long axis of the forward projector aligns along the axial direction, i.e. along the z-axis.

Given a forward projector $f(x, y, z)$, the traditional R-L algorithm defines the back projector as:

$$b(x, y, z) = \hat{f}(x, y, z), \tag{11}$$

where $\hat{f}$ is the transpose of f.

If we transition to discrete notation, the transpose can be expressed as

$$b(i, j, k) = \hat{f}(i, j, k) = f(M - i + 1, N - j + 1, L - k + 1), 1 \leq i, j, k \leq M, N, L \tag{12}$$

where the M, N and L denote the dimensions of the 3D image and i, j and k are the voxel indices.

In the Fourier domain, the discrete Fourier transform of the back projector is the conjugate of the discrete Fourier transform of the forward projector:

$$B_{Trad}(k_x, k_y, k_z) = DFT(b) = conj[DFT(f)]. \tag{13}$$

1. Gaussian back projector

The Gaussian back projector uses a 3D Gaussian function with full width at half maximum (FWHM) matching the FWHM of the forward projector (i.e. the microscope PSF). The 3D normal Gaussian distribution is defined as

$$h(x, y, z) = a \exp\left(-\frac{x^2}{2\sigma_x^2} - \frac{y^2}{2\sigma_y^2} - \frac{z^2}{2\sigma_z^2}\right), \tag{14}$$

with $a = \frac{1}{(2\pi)^{3/2}\sigma_x\sigma_y\sigma_z}$, and $\sigma_x, \sigma_y, \sigma_z$ are the standard deviations in 3 dimensions, respectively.

The coefficient a can be omitted since the back projector is normalized before deconvolution, and the relationship between the standard deviation and FWHM for a Gaussian distribution is:

$$\sigma_x = FWHM_x/(2\sqrt{2\ln 2}) \tag{15}$$

$$\sigma_y = FWHM_y/(2\sqrt{2\ln 2}) \tag{16}$$

$$\sigma_z = FWHM_z/(2\sqrt{2\ln 2})\,. \tag{17}$$

Then the Gaussian back projector is derived as:

$$b_{Gauss}(x,y,z) = \exp\left(-\frac{4\ln 2 \cdot x^2}{FWHM_x^2} - \frac{4\ln 2 \cdot y^2}{FWHM_y^2} - \frac{4\ln 2 \cdot z^2}{FWHM_z^2} \right), \quad (18)$$

where $FWHM_x$, $FWHM_y$, $FWHM_z$ are the FWHMs of the Gaussian back projector in x, y, and z, respectively, and are equivalent to the FWHMs of f and $\hat{f}$.

Using the same sized FWHMs as f in the spatial domain implies that the Gaussian back projector possesses a greater spatial frequency extent i than the traditional back projector in the Fourier domain, and as such results in a slightly flatter spectral product $|DFT(b)DFT(f)|$ as shown in **Figure S2.1**. This explains why we observe an acceleration with a Gaussian back projector compared to the traditional R-L back projector.

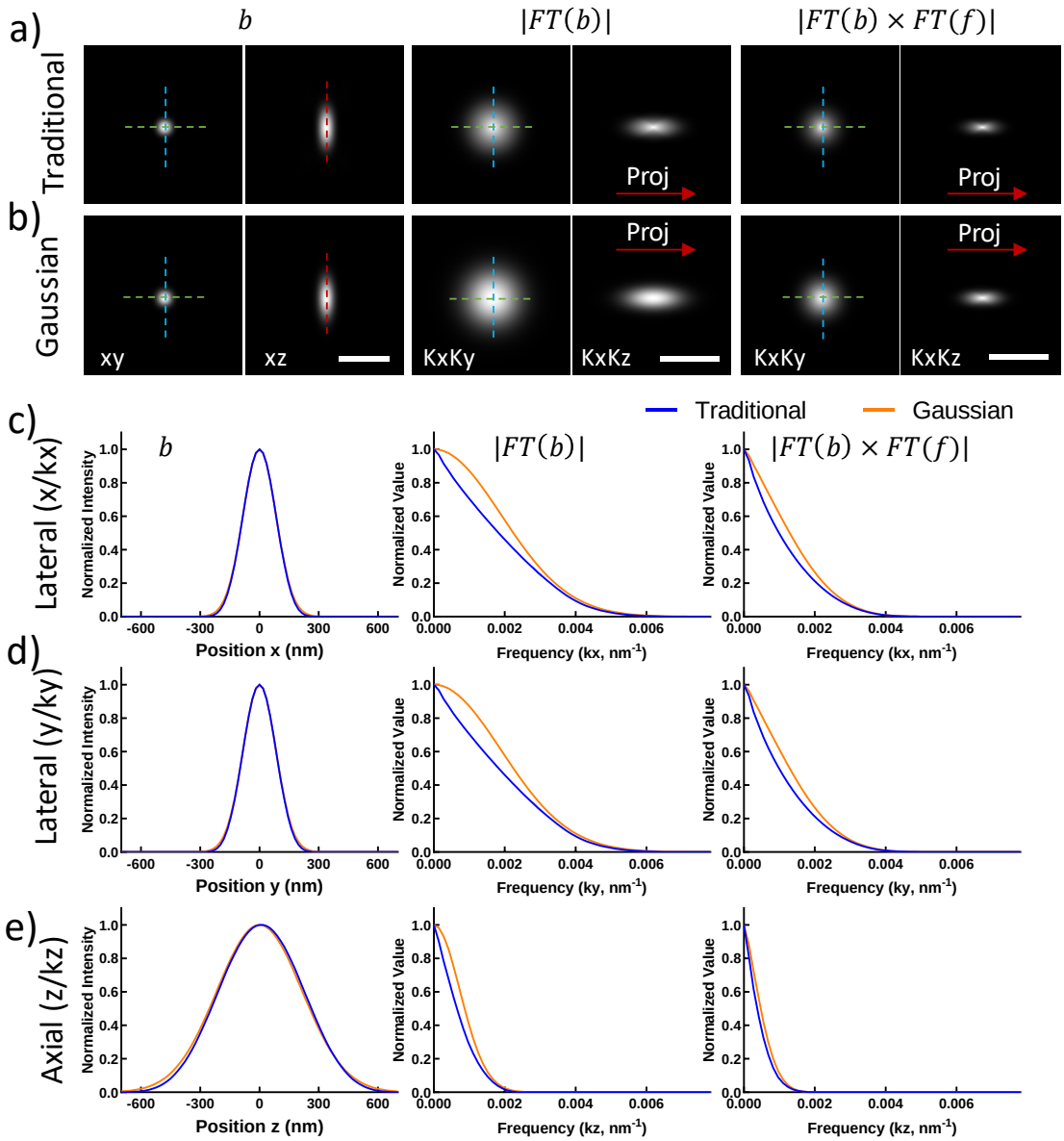

Figure S2.1, Comparison of traditional and Gaussian back projectors with equivalent FWHM a), **b)** Lateral and axial slices through the traditional (**a**) and Gaussian (**b**) back projectors for iSIM, shown in real space (left, b), Fourier space (middle, |FT(b)|) and the spectral product of forward and back projectors (right, |FT(b) FT(f)|). **c)** Lateral (x, kx) line profiles through the center of the slices showing in **a**, **b** (green dashed lines), comparing back projectors in real space (left), Fourier space (middle), and the spectral product (right). **d)** Lateral (y, ky) line profiles through the center of the slices shown in **a**, **b** (cyan dashed lines), comparing back projectors in real space (left), Fourier space (middle), and the spectral product in Fourier space (right). **e)** Axial (z or kz) profiles of the slices shown in **a**, **b**, comparing back projectors in real space (left), Fourier space (middle), and the spectral product (right). Note the left profiles correspond to line profiles through the center of the corresponding images in **a, b** (red dashed lines), while the middle and right profiles are maximum intensity projections in the kx direction as indicated by the red arrows ('Proj') in **a**, **b**, to capture the full extent of the spatial frequencies in the axial direction. Scale bars: **a**, **b**) 1 μm in left column, 1/100 nm^{-1} in middle, right columns.

2. Butterworth back projector

To make the spectral product $|DFT(b)DFT(f)|$ flatter, one possibility is to make the discrete Fourier transform of the back projector $DFT(b)$ broader (which is equivalent to making the back projector narrower in the spatial domain). An extreme example is the Dirac delta function, i.e. the narrowest positive distribution in the spatial domain, which produces a uniform distribution in the Fourier domain. However, all microscopes function as low-pass filters, allowing only frequencies lower than the resolution limit to be transferred to the image. If the delta function is used as a back projector, higher spatial frequencies would be introduced into the image, thus boosting the noise during the R-L iteration as shown in **Figure S2.2**. To suppress this noise, we employ a Butterworth low-pass filter to ensure that the frequency contribution of the back projector remains within the resolution limit of the microscope. The one- dimensional Butterworth filter is defined as:

$$H(k) = \frac{1}{\sqrt{1 + \varepsilon^2 k^{2n}}} \tag{19}$$

where k is the spatial frequency in the Fourier domain, n is the order of the filter and ε is the maximum passband gain.

To obtain a 3D Butterworth filter, we decompose k into 3 components, accounting for the microscope's resolution limit in each dimension:

$$k = \sqrt{\left(\frac{k_x}{k_{cx}}\right)^2 + \left(\frac{k_y}{k_{cy}}\right)^2 + \left(\frac{k_z}{k_{cz}}\right)^2}, \tag{20}$$

where the k_{cx}, k_{cy}, k_{cz} are the cutoff frequencies corresponding the the resolution limit in the xyz dimensions, respectively. We then define the the Butterworth back projector in the Fourier domain, $FT(b)$,as:

$$B_{Butterworth}(k_x, k_y, k_z) = \frac{1}{\sqrt{1 + \varepsilon^2 \left[\left(\frac{k_x}{k_{cx}}\right)^2 + \left(\frac{k_y}{k_{cy}}\right)^2 + \left(\frac{k_z}{k_{cz}}\right)^2\right]^n}} \tag{21}$$

In the spatial domain, the Butterworth back projector can be obtained by an inverse Fourier transformation:

$$b_{Butterworth}(x,y,z) = FT^{-1}[B_{Butterworth}(k_x,k_y,k_z)]. \quad (22)$$

The spectral intensity at the cutoff frequency is

$$\beta = B_{Butterworth}(k_{cx},0,0) = B_{Butterworth}(0,k_{cy},0) = B_{Butterworth}(0,0,k_{cz}) = \frac{1}{\sqrt{1+\varepsilon^2}}. \quad (23)$$

β is also referred to as the cutoff gain, i.e. it represents the spectral amplitude that is passed at the microscope's resolution limit.

The Butterworth back projector $B_{Butterworth}(k_x,k_y,k_z)$ (or $b_{Butterworth}(x,y,z)$ in the spatial domain) can thus be characterized by the cutoff gain β and the filter order . β is often set as a small value that suppresses high frequencies beyond the resolution limit, thus reducing the noise in the deconvolution (**Figure S2.2**). The filter order n is related to the transition slope at the cutoff. Ideally the transition slope would be as steep as a "brick wall"; a higher filter order brings the filter closer to an ideal "brick wall". In practice however, this ideal transition slope is undesirable as it produces excessive ringing in the spatial domain.

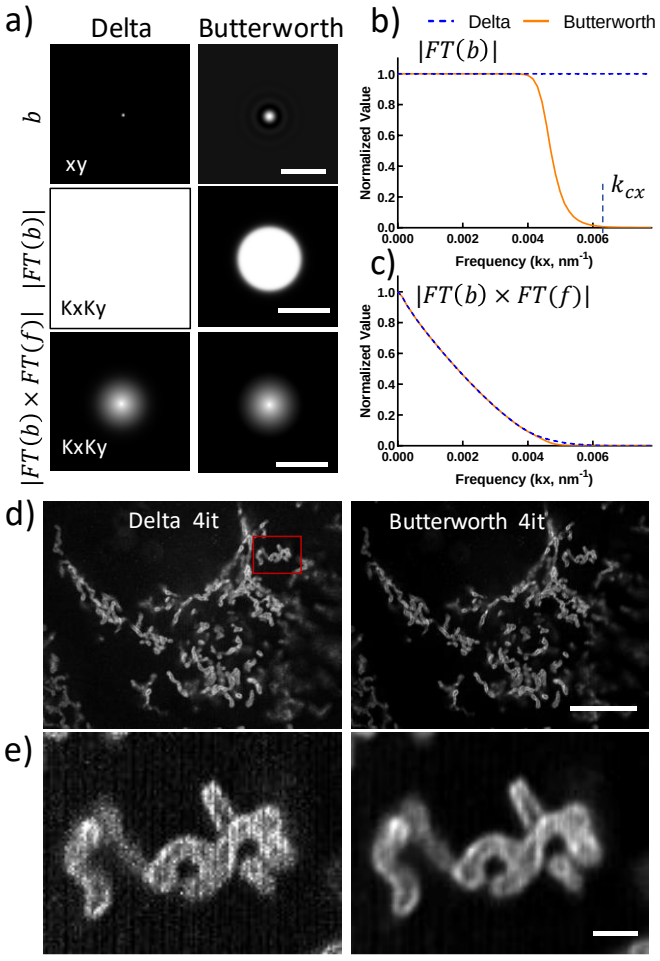

Figure S2.2, Delta and Butterworth back projectors and corresponding R-L deconvolution. a) Lateral slices through the Dirac delta (left) and Butterworth (right) back projectors for iSIM, shown in real space (top, b), Fourier space (middle, |FT(b)|) and the spectral product of forward and back projectors (bottom, |FT(b) FT(f)|). **b)** Lateral (kx) line profiles through the center of the image in **a,** middle row, comparing back projectors in Fourier space. The cutoff frequency k_{cx} is indicated by a dotted line. **c)** Lateral (kx) line profiles through the center of the image in **a** bottom row, comparing the spectral product using the two different back projectors. **d)** R-L deconvolution of images of U2OS cells immunolabeled by Tomm20 Alexa-Fluor 488 and imaged with iSIM. Single planes from imaging stacks are shown, with iteration number (it) and back projector as indicated. **e)** Higher magnification views, corresponding to the red rectangular region in **d**, highlighting the additional noise that results when using the delta function back projector. Note this noise is suppressed when using the Butterworth back projector. Here we used $\beta = 0.001$ and $n = 8$ for the Butterworth back projector. Scale bars: **a**) 1 µm in top row, 1/100 nm^{-1} in middle and bottom rows; **d**) 10 µm; **e**) 1 µm. Experiments were repeated on similar datasets at least 2 times for **d)** and **e)**, with similar results obtained each time; representative data from a single experiment are shown.

3. Wiener-Butterworth back projector

Finally, the choice that maximally flattens the spectral product $|DFT(b)DFT(f)|$, sets the discrete Fourier transform of the back projector equal to the inverse of the discrete Fourier transform of the forward projector, i.e. $DFT(b) \approx 1/\ DFT(f)$. Obviously $DFT(f)$ goes to zero at some point, but one could consider

$$B_{Wiener}(k_x, k_y, k_z) = \frac{Conj[DFT(f)]}{[DFT(f)]^2 + \alpha}, \tag{24}$$

where α is a small value that prevents the denominator from becoming zero. This is like a classic Wiener filter that seeks to invert the forward projector $DFT(f)$ out to some point and then rolls off gently. However, when using such a filter, the results are highly sensitive to the choice of α. The Wiener filter either fails to recover the best resolution possible with the microscope (if α is too large) or amplifies the noise and introduces more ringing artifacts (if α is too small, see also **Supplementary Fig. 4**). We would ideally circumvent these issues by combining the Wiener and Butterworth filters, obtaining a back projector that enables a flat spectral product but also suppresses spatial frequencies beyond the resolution limit. This is the Wiener-Butterworth back projector we use in our paper:

$$\begin{aligned} B_{WB}(k_x, k_y, k_z) &= B_{Wiener}(k_x, k_y, k_z) \times B_{Butterworth}(k_x, k_y, k_z) \\ &= \frac{Conj[DFT(f)]}{[DFT(f)]^2 + \alpha} \times \frac{1}{\sqrt{1 + \varepsilon^2 \left[\left(\frac{k_x}{k_{cx}}\right)^2 + \left(\frac{k_y}{k_{cy}}\right)^2 + \left(\frac{k_z}{k_{cz}}\right)^2 \right]^n}}. \end{aligned} \tag{25}$$

The spatial analog of this filter can be derived by taking an inverse Fourier transform:

$$b(x, y, z)_{WB} = FT^{-1}[B_{WB}(k_x, k_y, k_z)]. \tag{26}$$

Again, we define the cutoff gain as

$$\beta = B_{WB}(k_{cx}, 0, 0) = B_{Wiener}(k_{cx}, 0, 0) \times \frac{1}{\sqrt{1 + \varepsilon^2}}, \tag{27}$$

so that as before β represents the spectral amplitude that is passed at the microscope's resolution limit.

Given a forward projector f, we now need to determine three parameters to fully specify the Wiener-Butterworth back projector: α, β and n. α is a small value used to ensure that inverting the forward projector does not result in division by zero. As with the Butterworth back projector, the cutoff gain β is set at a small value that suppresses spatial frequencies beyond the resolution limit, and the filter order n is used to set the transition slope at the cutoff frequency. We'll discuss these parameters in more detail in the next section.

4. Parameter configuration

1) The cutoff frequency

The cutoff frequency is usually defined as the highest possible spatial frequency passed by the microscope. We have yet to encounter a microscope capable of achieving this cutoff frequency, so instead we define the cutoff frequency as the FWHM of the PSF. Although in principle this choice may slightly underestimate the highest resolution achieved by the microscope, in practice we find that it avoids noise amplification at the highest spatial frequencies while still yielding high quality reconstructions.

2) Parameter α

As shown in equation (25), α is used to invert $DFT(f)$ in the first, Wiener filter term. We set α at a value that slightly boosts the spatial frequencies past the cutoff frequency, relying on the Butterworth filter term to suppress noise. In our experience, good results are obtained if α is set in the range $0.001 \sim 0.05$ (**Table S2.1**).

3) Parameter β

β defines the spectral amplitude at the cutoff frequency or resolution limit, and in our experience good results are obtained when this is set at a small value in the range from 0.001 to 0.05. Alternatively one can also set β based on the theoretical cutoff of the traditional R-L back projector $B\left(k_x, k_y, k_z\right)_{Traditional}$, or $DFT(\hat{f})$:

$$\beta = (B_{Trad}(k_{cx}, 0, 0) + B_{Trad}\left(0, k_{cy}, 0\right) + B_{Trad}(0, 0, k_{cz}))/3. \quad (28)$$

In this case, β is an average of the 3 cutoff gains corresponding to each dimension of the traditional back projector. All β values used for datasets in our paper are listed in **Table S2.1**.

4) Parameter n

The filter order n is related to the flatness of the frequency distribution within the passband of the Butterworth filter. A higher n would result in a flatter frequency response until the cutoff. However, as mentioned in previous sections, a higher n would also make the transition slope closer to a hard cutoff like a "brick wall", causing the ringing artifacts in the spatial domain. In contrast, a lower order n would make the transition slope gentler and sacrifice some spectral amplitude at spatial frequencies close to the cutoff. This choice in turn would require more iterations in R-L deconvolution. To empirically investigate this issue, we designed Wiener-Butterworth back projectors with different n and tested them on an image acquired by iSIM. As shown in **Figure S2.3**, the deconvolution with $n = 8$ only needs 1 iteration, while using smaller n requires more iterations for similar image quality.

We used n in the range 4 - 10 for all datasets presented in our paper (**Table S2.1**). For the datasets acquired by single- or dual- view microscopes, $n = 8$ or 10 enables R-L deconvolution with 1 iteration. For the datasets acquired by quad-view light-sheet microscopy, reflective diSPIM and reflective lattice light-sheet microscopy, the deconvolution is more sensitive to the ringing caused by a higher filter order. We used $n = 5$, producing a resolution-limited result with only 2-5 iterations. We note that even using this relatively conservative choice, Wiener-Butterworth deconvolution is still 10-15x faster than traditional R-L deconvolution.

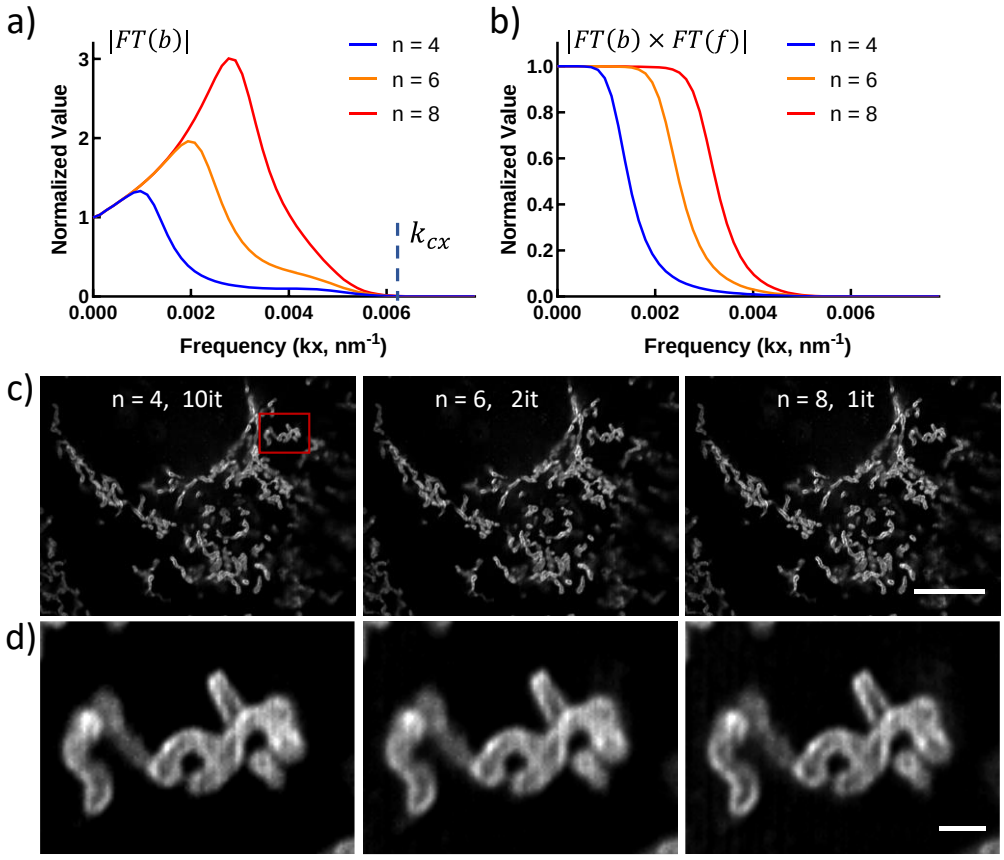

Figure S2.3, Comparing Wiener-Butterworth back projectors with different filter orders. a) Lateral (kx) line profiles through the central slice of Wiener-Butterworth back projector, for different filter orders. **b)** Lateral (kx) line profiles through the center of the spectral products $|DFT(b)DFT(f)|$ with filter orders as in **a**. **c)** R-L deconvolution results of images of U2OS cells immunolabeled by Tomm20 Alexa-488 and imaged with iSIM. Single planes from imaging stacks are shown, with filter orders and iteration number (it) as indicated. **d)** Higher magnification views, corresponding to the red rectangular region in **c**. Scale bars: **c**) 10 µm; **d**) 1 µm. Experiments were repeated on similar datasets at least 2 times for **c)** and **d)**, with similar results obtained each time; representative data from a single experiment are shown.

Table S2.1, Parameters for all datasets used in Butterworth and Wiener-Butterworth Deconvolution

		Butterworth			Wiener-Butterworth			
Figures/Videos	**Microscope**	$\boldsymbol{\beta}$	$\boldsymbol{n}$	**Iteration Number**	$\boldsymbol{\alpha}$	$\boldsymbol{\beta}$	$\boldsymbol{n}$	**Iteration Number**
Fig. 1 e, f, Sup. Fig. 4f Sup. videos 1-3	iSIM	0.001	8	4	0.001	0.001	8	1
Sup. Fig. 5c, 7c	Widefield	0.01	10	4	0.01	0.01	10	1
Sup. Fig. 7a	Confocal	0.001	8	3	0.001	0.001	8	1
Sup. Fig. 7b	iSPIM	0.01	10	5	0.05	0.01	10	1
Figs. 2a, j, 3a, d Sup. Figs. 8, 19 Sup. Videos 4, 5, 7, 11-15	diSPIM	0.01	10	3 (Sup. Fig. 8)	0.05	0.01	10	1
Fig. 2e Sup. Fig. 9 Sup. Video 6	Quad-view light-sheet	--	--	--	0.01	0.05	5	5
Fig. 4c Sup. Video 16	Reflective diSPIM	--	--	--	0.01	0.02	5	2
Fig. 4f Sup. Video 17	Reflective LLS	--	--	--	0.01	0.02	5	4
Sup. Figs. 13, 14 Sup. Video 10	Zeiss Z.1 light-sheet	--	--	--	0.05	0.03	10	1

Supplementary Note 3, Connection between single-iteration R-L and Wiener filtration

The challenges of deconvolution are well known. One seeks to determine a more faithful estimate of the imaged object e by modeling and compensating for the effects of the convolution kernel f. If the imaging equation is

$$i = e * f, \tag{29}$$

then in the Fourier domain it is given by

$$I = EF, \tag{30}$$

where capital letters denote Fourier transforms, and F, the Fourier transform (FT) of the point spread function f is known as the optical transfer function (OTF). While it might seem that the FT of the desired estimate could be readily obtained by calculating $\hat{E} = I/F$, this formulation is problematic for two reasons. (1) Most OTFs go to zero at some point determined the NA of the lens and wavelength of the light, rendering the ratio undefined. (2) when F is finite but vanishingly small, dividing the measured data by those small values will amplify any noise contaminating i.

A common strategy is to include a small constant in the denominator $\hat{E} = I/(F + \alpha)$. This prevents division either by zero or by too small a value of F and is a form of the *Wiener filter*. In the frequency domain, the resulting filter approximates the inverse OTF at low frequencies where F is relatively large and then rolls off toward zero at the cutoff frequency. In the spatial domain the effect is a convolution with a kernel given by the inverse FT of $1/(F + \alpha)$.

For the modified R-L explored here, it can be shown that when the starting guess is a uniform image, the first iteration corresponds to application of a Wiener-like filter. The modified R-L update is given by

$$e_{k+1} = e_k \left\{ \left[\frac{i}{e_k * f} \right] * b \right\}. \tag{31}$$

If $e_0 = u$, where u denotes a uniform image of 1s, then

$$e_1 = u\{ \left[\frac{i}{u * f} \right] * b \}, \tag{32}$$

Now $u * f = u$ because in the Fourier domain $FT\{u * f\} = U(v)F(v) = \delta(v)F(v) = \delta(v)$ because $F(0) = 1$ for a normalized PSF. So

$$e_1 = u \left\{ \left[\frac{i}{u} \right] * b \right\}, \tag{33}$$

The elementwise division of i by a uniform image has no effect and neither does the multiplication by a uniform image, so

$$e_1 = i * b. \tag{34}$$

This corresponds to linear, shift-invariant filtration with the modified back projection kernel. I.e., for the WB kernel the first iteration is equivalent to filtering with the WB function. Any subsequent iterations lead to an effectively nonlinear relationship between the estimated image and the raw measured image.

When the starting guess is taken to be the measured image itself, $e_0 = i$, the first iteration already leads to a nonlinear relationship between the between the estimated image and the raw measured image. In this case the expression

$$e_1 = i\left\{\left[\frac{i}{i * f}\right] * b\right\}. \tag{35}$$

cannot be expressed as the action of a linear filter on the measured data i.

Supplementary Note 4, Deep learning for deconvolution

Our goal is to create deep learning models that simultaneously improve axial and lateral resolution, directly incorporating 3D information contained within the image stacks. A challenge when processing 3D image volumes is the associated computational burden. For example, processing a modestly sized 32-bit input image stack 40 MB in size, using only 8 convolution layers with 4 channels to output the result, implies that 40 x 4 x 8 = 1280 MB of memory is required. Recent evidence suggests that many complex tasks benefit from even deeper networks, with more layers[4-6]. Such increased depth and additional operations including activation functions and batch normalization[7] help the network to better represent[8] the underlying task and to stabilize the learning procedure[7], but at least double the computational memory required. Back-propagation, which is used to tune the network parameters according to the loss function, additionally doubles computational cost. One solution to the memory problem is to use down-sampling (pooling) in the learning model, e.g. as employed in the U-net architecture[9]. However, too much down-sampling results in a loss of detail unless the model contains enough parameters to compensate for the effect. Another solution is to crop the input data into multiple subimages. Selecting a random subset of these images for training can help the model learn the relationship between input and labels (ground truth) in a memory-efficient manner, but during the test procedure, stitching is required to combine the cropped images back to the original image size. Boundary artifacts[10], as well as differing local intensity/contrast in each restored sub-image can make this a nontrivial task. These issues motivated our search to find an efficient deep learning method for performing 3D deconvolution on the whole volumetric image input.

We adopted the concept of a densely-connected network[11] (Densenet) to establish this framework, terming our model 'DenseDeconNet'. The major components of our model are three dense blocks. These blocks use multiple dense connections between convolutional layers to extract relevant features from the image volumes, learning the deblurring necessary for image reconstruction. To efficiently process volumes of nearly 80 MB input size with a 14-layer model, another important concept we incorporated is the use of down-sampling and up-sampling operations, decreasing the computational memory required by at least 50%.

1. Model architecture

The DenseDeconNet Framework is shown in **Figure S4.1**. Our DenseDeconNet adopts a fully convolutional architecture[12] for 3D image data, taking full advantage of the 3D geometric cues for effective volume-to-volume image restoration and enabling the processing of input data of different sizes. Our model also incorporates dense connections to create short paths from a layer to all its subsequent layers. These connections improve the usability of early layers' features, which decreases the number of parameters needed to learn redundant feature maps, thus making the model easier to train.

As shown in **Figure S4.1**, our network consists mainly of three dense blocks, with additional operations before and after the blocks. The convolutional layer before dense block 1 is used to increase the channel number (i.e., the number of feature maps), sampling the input data with dimension w x h x d for later skip connection after dense block 3. The convolution in this layer is performed with [3x3x3] kernel and [1x1x1] stride, and is followed by a batch normalization (BN) and rectified linear unit (Relu) activation function[13]. The number of output channels (denoted as O_{11}) is 4, resulting in an output of size of w x h x d x 4.

After O_{11}, dense block 1 contains three other convolutional layers with output denoted O_{12}, O_{13}, and O_{14}. The operations in each convolutional layer also include a convolution (Conv), a BN, and a Relu activation function. The convolution kernel size is set to [3x3x3] with stride [1x1x1]. These operations are used to extract higher-level features from previous layers. We denote the series of operation in each layer

as $T(\bullet)$, thus O_{12} can be computed from O_{11} as:

$$O_{12} = T(O_{11})$$

We use O_{12} to compute O_{13} and to create a short path for delivering the feature map from O_{11} to O_{13} as follows. First, we concatenate the output channels O_{12} and O_{11}, denoting this operation as $(O_{12} \oplus O_{11})$, where $\oplus$ represents the concatenate operation (Concat). Then we use this concatenation as the input of next layer so that O_{13} is computed as:

$$O_{13} = T(O_{12} \oplus O_{11})$$

Similarly, short paths for O_{11} and O_{12} to O_{14} are created and concatenated with O_{13} as the input to O_{14}:

$$O_{14} = T(O_{13} \oplus O_{12} \oplus O_{11})$$

Concatenation helps subsequent layers to reuse previous feature maps, but it also causes the inclusion of redundant features and increases the number of parameters. For example, if the number of output channels in O_{12} is 8 and the number of output channels for O_{11} is 4, then the number of input channels for O_{13} is 12, and the number of input channels for O_{14} is 16. Because O_{12} is derived from O_{11}, their feature maps may be similar. To lessen this redundancy, the number of output channels in O_{13} and O_{14} is limited to 4 by using the convolutional layers to select the most important features. This attribute also minimizes extraneous computational burden.

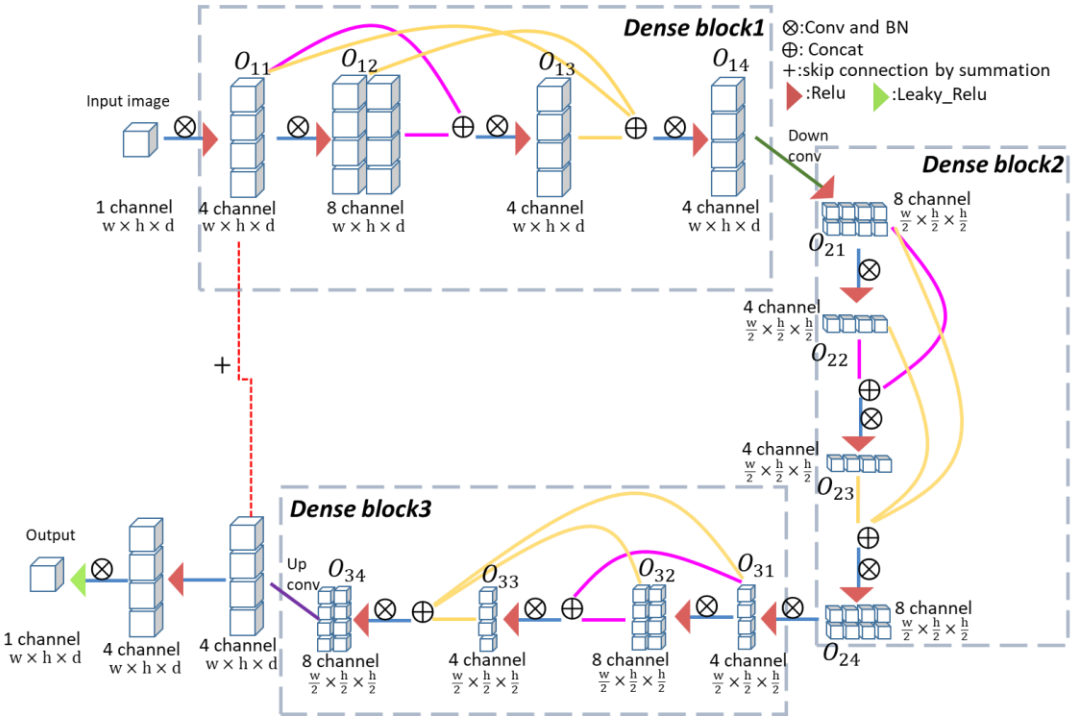

Figure S4.1, The architecture of our DenseDeconNet neural network. This fully convolutional network consists of three dense blocks (dashed rectangles), one down-sampling operation ('Down conv'), one up-sampling operation ('Up conv') and one skip connection (red dotted line). All operations are implemented on 3D data. Conv: convolution; BN: batch normalization; Relu: rectifying linear unit; Leaky_Relu: leaky rectifying unit; w: width; h: height; d: depth; Concat: concatenation. O_{b1}, O_{b2}, O_{b3}, O_{b4}, with b=1, 2, 3 represent the output of convolutional layers in each dense block. Blue lines signify the extraction and transfer of feature maps in all layers. Magenta lines signify the concatenation of the first two layers in each block, yellow lines signify the concatenation of the first three layers in each block.

After dense block 1, we use a down-sampling layer to decrease the size of the feature map O_{14} by half to w/2 x h/2 x d/2, but include 8 channels. The result O_{21} serves as the beginning of dense block 2. The down-sampling layer consists of a convolution with [2x2x2] kernel and [2x2x2] stride (denoted Down conv), a BN and a Relu activation. Constructing O_{21} in this way enables efficient memory usage while also increasing the receptive field to incorporate more information surrounding each voxel.

Dense block 2 also contains other 3 convolutional layers with similar function to dense block 1, with outputs denoted O_{22}, O_{23}, O_{24}, respectively. Again, the number of output channels are limited to 4 or 8, and we rely on the network learning the most salient features to avoid redundancy.

After dense block 2, a convolutional layer connects dense block 3 to increase the depth and receptive field of the model. This layer consists of a convolution with [3x3x3] kernel and [1x1x1] stride, a BN and a Relu activation and compresses the number of feature maps from 8 in the last output of dense block 2 (i.e., O_{24}) to 4 in the input of dense block 3 (i.e., O_{31}).

Dense block 3 contains 3 other convolutional layers with outputs O_{32}, O_{33}, O_{34}, respectively, with characteristics shown in **Fig. S4.1**. After dense block 3, the network needs to recover the size of the original input image. Therefore, we use an up-sampling component composed of a transport convolution with [2x2x2] kernel and [2x2x2] stride (Up conv) and a BN. However, the transport convolution usually introduces checkerboard artifacts[10], which decreases output quality. To remedy this problem, we use a long skip connection that sums the output of O_{11} and the up-sampled output of O_{34}. Next, we implement a nonlinear Relu operation. A final convolution layer is used to output the result. Because the gradient may vanish when the input of the Relu operation is negative, we used a Leaky-Relu operation[14] in the last convolution layer to maintain the gradient. The total number of learned parameters in our DenseDeconNet are approximately 18 thousand.

We designed our objective (loss) function with three terms: the mean squared error (*MSE*), the structural similarity (*SSIM*) index[12] and the minimum value of the output (*MIN*). The *MSE* is widely used as a fidelity term to make sure the difference between network outputs and ground truths is as small as possible, but it may lead to blurred edges and a loss in resolution and fine image structure[15]. Thus, we also used the *SSIM* to preserve the global structural similarity between the network output and the ground truth. Because the Leaky_Relu in the last convolutional layer permits negative values, we monitor the *MIN* of the output to avoid negative values. The *MSE* and the *MIN* complement each other, as the objective function tends to make the *MIN* value larger, but the *MSE* acts to limits the *MIN*. Specifically, the objective function we aim to minimize is:

$$L(l,o) = MSE(l,o) - \ln\left(\frac{1+SSIM(l,o)}{2}\right) - \lambda MIN(o) \tag{36}$$

where *l* represents the ground truth, *o* represents the model output and ln is the natural logarithm function. The *MSE* is defined as:

$$MSE(l,o) = \frac{1}{whd}\sum_{k=1}^{d}\sum_{j=1}^{w}\sum_{i=1}^{h}\left(l(i,j,k) - o(i,j,k)\right)^2 \tag{37}$$

where d, w, h represents the depth, width and height of the ground truth volume. The *SSIM* is defined as:

$$SSIM(l,o) = \frac{(2\mu_l\mu_o + C_1)(2\sigma_{lo} + C_2)}{(\mu_l^2 + \mu_o^2 + C_1)(\sigma_l^2 + \sigma_o^2 + C_2)} \tag{38}$$

where μ_l, μ_o are the mean values of l, o; ${\sigma_l}^2$, ${\sigma_o}^2$ are the variances of l, o; σ_{lo} is the covariance of l and o; and C_1 and C_2 are small constants that prevent the denominator from becoming zero. In our implementation, we set $C_1 = 1e^{-4}$ and $C_2 = 9e^{-4}$. *SSIM* is in the range $(0,1]$. When *SSIM* equals 1, the ground truth and output are identical. Values for *MSE* and *SSIM* for all datasets are reported in **Table S4.2**. The $\ln(\cdot)$ operation is used to keep the objective function positive. The last term *MIN* is the minimum value of the output: $MIN(o) = \min(output)$.

We use a tunable parameter λ to control the influence of *MIN*. If during training, the output tends to shift towards negative values, we set $\lambda > 1$, otherwise, we set $\lambda < 1$ or $\lambda = 0$.

The network is optimized using the backpropagation algorithm with the adaptive moment estimation (Adam) optimizer[16] and a starting learning rate r_0 which decays during the training procedure according to:

$$r = r_0 * k^{\frac{global\_step}{decay\_step}} \tag{39}$$

where *k* is the decay rate, *global_step* represents the number of training iterations (updated after each iteration), and *decay_step* determines the decay period. The values of these parameters are given in **Table S4.1**.

DenseDeconNet is implemented with the Tensorflow framework version 1.4.0 and python version 3.5.2 in the Ubuntu 16.04.4 LTS operating system. Training was performed on a workstation equipped with 32 GB of memory, an Intel(R) Core (TM) i7 – 8700K, 3.70 GHz CPU, and two Nvidia GeForce GTX 1080 Ti GPUs with 11 GB memory each. Kernels in the convolution layers were randomly initialized with a Gaussian distribution (mean= 0, standard deviation= 0.1). For an input image 70 MB in size, fully training the network with 10000 iterations took ~60 h.

2. Results

We tested DenseDeconNet on images of membranes and nuclei in live *C. elegans* embryos acquired with diSPIM, images of GCaMP3 expression in live *C. elegans* embryos acquired with reflective diSPIM, and images of α-actinin in live cells acquired with reflective lattice light-sheet (LLS) microscopy. Ground truth data consisted of traditional Richardson Lucy (R-L) joint deconvolution with 10 iterations for diSPIM data (conventional glass coverslips and reflective coverslips), and R-L deconvolution with the Wiener-butterworth back-projector with 1 iteration for reflective lattice light-sheet data. Additional parameters for datasets are shown in **Table S4.1**. All data are derived from volumetric time-series ('4D' data); 80% of volumes are used for training and the remaining 20% for testing. The test data are randomly chosen; all results shown in the following figures and in the main text figures display only the test data. Different datasets have different input sizes, but the training batch size is always 1. All the input data and ground truth data are normalized as follows:

$$X_N = \frac{X - \min(X)}{\max(X) - \min(X)} \quad X\ is\ input\ data \tag{40}$$

We first investigated the performance of deep learning on images of live *C. elegans* embryos expressing a pan-membrane mCherry label and pan-nuclear GFP label, acquired with diSPIM. We used the single-view images as network inputs and the dual-view joint deconvolution results as the ground truth. As shown in **Fig. S4.2**, the output of our DenseDeconNet network closely resembles the dual-view traditional deconvolution (e.g., the details indicated by yellow and pink arrows), although with worsened axial resolution. Interestingly we found that the network retained some details that are lost in the dual-view ground truth (e.g. the details indicated by the green arrows disappeared in the dual-view deconvolution but are retained in our method). These results are likely due to the highly dynamic nature of the membrane during embryo development, resulting in slight differences between the two raw views (which are acquired 1 s apart) and thus a loss of fine structure in the reconstruction.

Results were similar for relatively large structures like nuclei (**Fig. S4.3**) in late embryogenesis, when the embryo moves and twists frequently inside the eggshell. As before, the output from DenseDeconNet worsened axial resolution relative to the dual-view joint deconvolution (red arrows). However, this effect is counterbalanced by the effects of motion blur, which hinder the registration of the two volumetric views and compromise the resulting deconvolution (orange arrows).

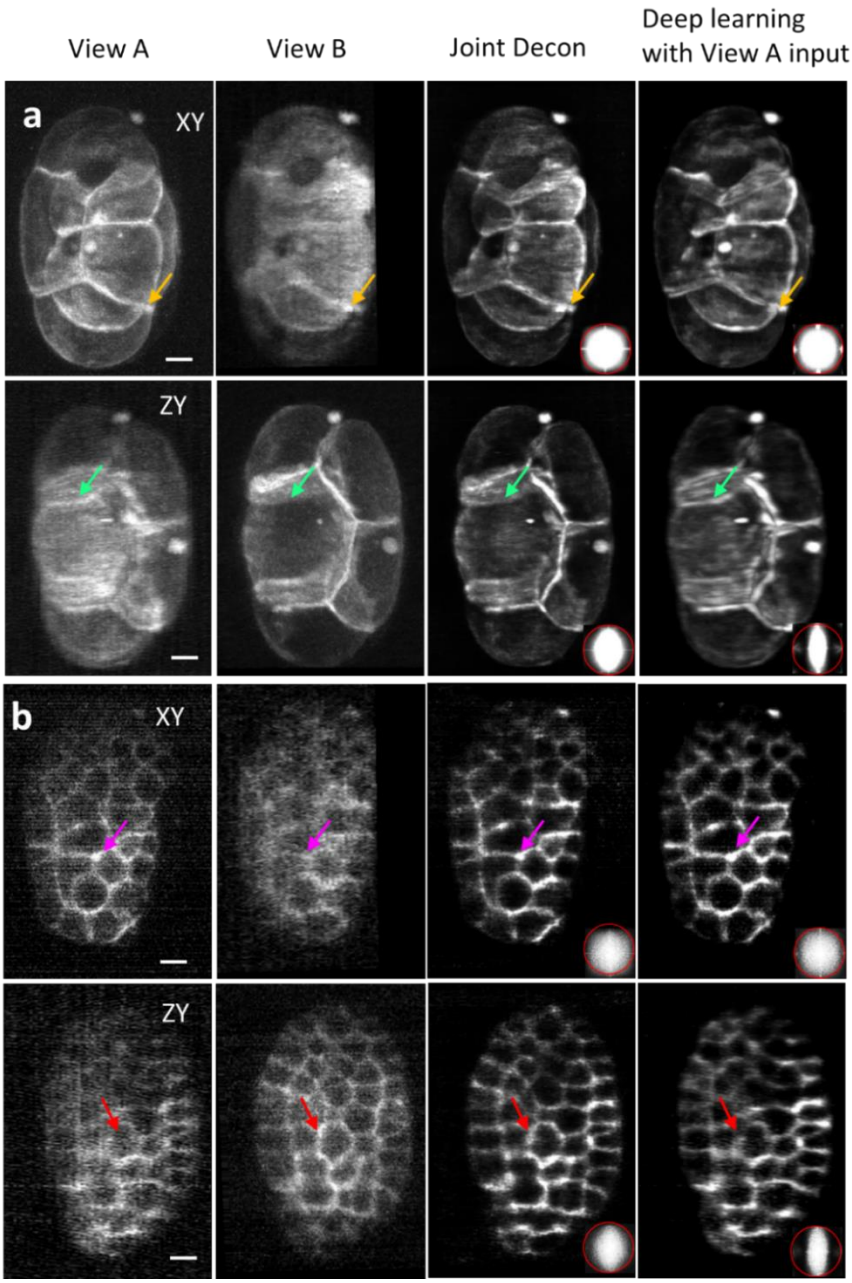

Figure S4.2, Comparisons between raw single views, traditional joint deconvolution ('Joint Decon'), deep learning with single-view input, mCherry-membrane label in live *C. elegans* embryos. a) Examples are from ~1 hour post fertilization and **b)** 4 hours post fertilization, XY and YZ maximum intensity projections are shown. In lateral XY views, both deep learning and traditional joint deconvolution produce similar reconstructions. The improved spatial resolution and contrast relative to the raw data reveal details that are otherwise obscured (magenta and yellow arrows). In axial YZ views, axial resolution in the learned result is not improved to to same extent as in the joint deconvolution (red arrows, see also OTF insets). However, the network results retain features evident in View A that are lost in the joint deconvolution (green arrows). OTFs averaged from all slices are shown at inset; red bounding box indicates a circle of 0.33 μm^{-1}. Scale bars: 5 µm. Traditional joint deconvolution experiments were repeated on similar datasets at least 2 times, with similar results obtained each time; the deep learning model was trained on one time-lapse dataset and applied to multiple datasets (N>=2), with similar results obtained for each dataset.

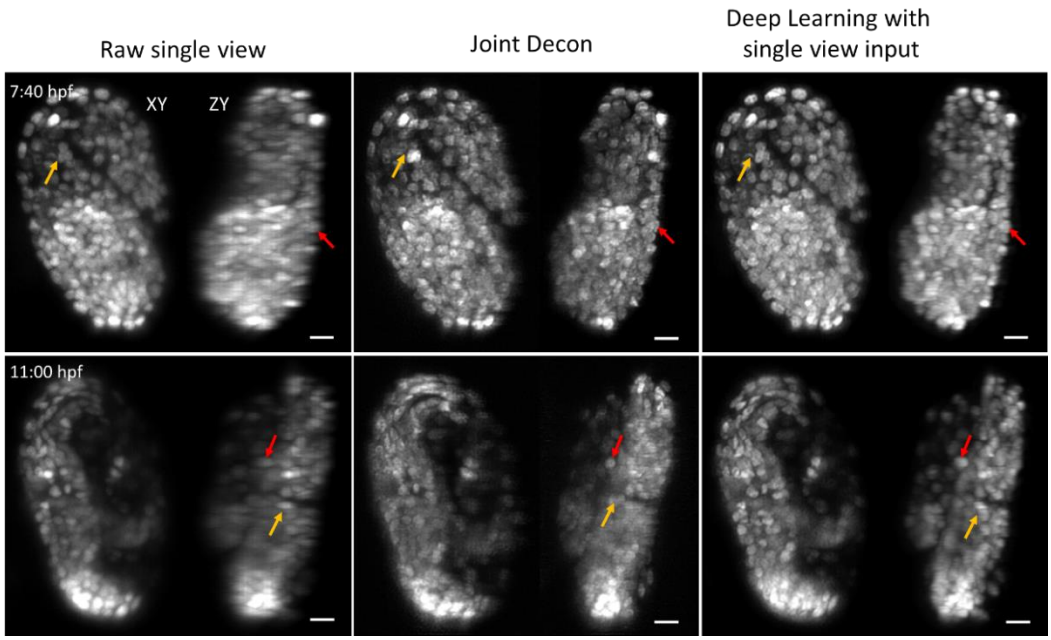

Figure S4.3. Comparisons between raw single view, traditional joint deconvolution ('Joint Decon'), and deep learning, GFP-nuclear label in live *C. elegans* embryos. Lateral (left) and axial (right) maximum intensity projections are shown for each condition; selected time points are shown both earlier in embryogenesis (top row) and later, post-twitching (bottom row). Note that the results shown for late twitching were obtained using training data from early twitching. Axial resolution is highest in the deconvolved result (red arrows). However, movement and twitching lead to degraded registration and deconvolution, resulting in improved reconstructions for many nuclei in the learned result (orange arrows). Scale bars: 5 µm. Traditional joint deconvolution experiments were repeated on similar datasets at least 2 times, with similar results obtained each time; the deep learning model was trained on one time-lapse dataset and applied to multiple datasets (N>=2), with similar results obtained for each dataset.

We next investigated if we could further improve our reconstruction by using both orthogonal, registered volumes as input, and the joint deconvolution as the ground truth (**Supplementary Video 18**). The only change to the network is that the two inputs are concatenated, and the number of input channels is increased to two (**Fig. 4b**). For example, for two registered, orthogonally captured volumes in the reflected diSPIM each with dimensions [w x h x d], the input is now [w x h x d x 2]. However, like the single view case considered above, the output sizes of the first convolutional layer in both cases are [w x h x d x 4], and the following dense blocks and other operations are all the same as in the single view input case. Thus, operating the network with two inputs does not substantially increase computational burden. As shown in **Fig. S4.4** and **Supplementary Video 18**, using two inputs provides more information to the network, allowing resolution and resolution isotropy recovery, as well as the removal of epifluorescence contamination. With suitable training data, our DenseDeconNet thus facilitates the reconstruction of raw reflective diSPIM data.

Additional examples illustrating that the network performs better if two registered views are incorporated include registered dual-view GCaMP3 *C. elegans* embryo data acquired in the diSPIM (**Fig. S4.5, Supplementary Video 16**) and α-actinin data acquired by reflective lattice light-sheet (LLS) microscopy (**Fig. S4.6, Supplementary Video 17**).

For α-actinin data acquired by reflective LLS, the input data size for each view is 398 x 526 x 198 voxels, or 158 MB. This size exceeds the current memory limit for our network. Thus, in this case, we were forced to crop the data into multiple sub-volumes for training. Each subvolume then has size 210 x 271 x 198

voxels (42 MB), with a 22-pixel region in x and 16-pixel region in y overlap between neighboring subvolumes to avoid boundary artifacts. Note that when applying the training model to the test data, there is no need to crop the input data (i.e., we maintained the original size of the test data).

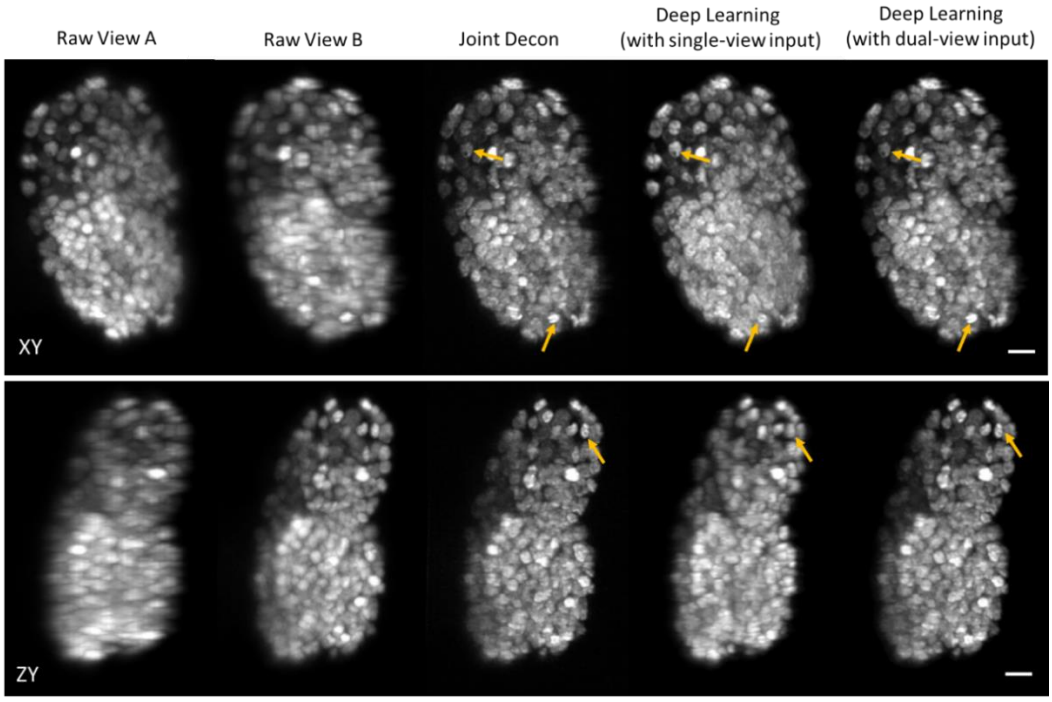

Fig. S4.4, Comparing reconstructions of pan-nuclear *C. elegans* data with single- vs. dual-view input, acquired on the diSPIM. Raw input data, traditional joint deconvolution ('Joint Decon'), deep learning with single-view input, and deep learning with dual-view input. Note the close resemblance (e.g. orange arrows) between the learned output with two inputs compared to the traditional deconvolution method. Scale bar: 5 µm. See also **Supplementary Video 18**. Traditional joint deconvolution experiments were repeated on similar datasets at least 2 times, with similar results obtained each time; the deep learning model was trained on one time-lapse dataset and applied to multiple datasets (N>=2), with similar results obtained for each dataset.

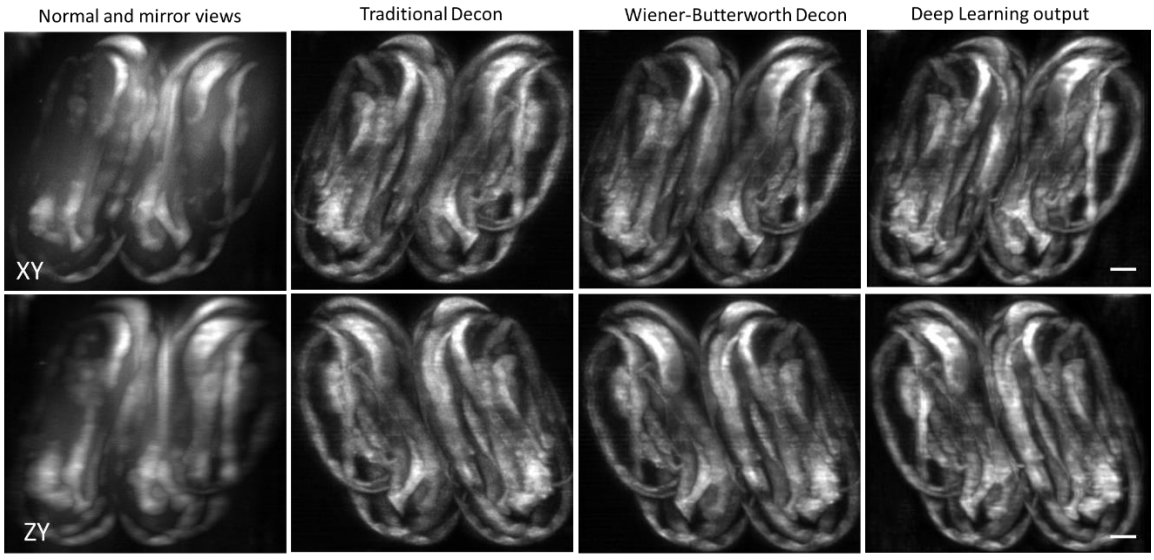

Fig. S4.5, Comparisons between raw mirror data, traditional joint deconvolution ('Joint Decon'), Wiener-Butterworth joint deconvolution, and deep learning, GCaMP3 expression in twitching *C. elegans* embryos. Lateral (top) and axial (bottom) maximum intensity projections are shown**.** Note the near equivalence of the deconvolved recontructions and the deep learning network output. Scale bars: 5 µm. See also **Supplementary Video 16**. Traditional and Wiener-Butterworth deconvolution experiments were repeated on similar datasets at least 2 times, with similar results obtained each time; the deep learning model was trained on one time-lapse dataset and applied to multiple datasets (N>=2), with similar results obtained for each dataset.

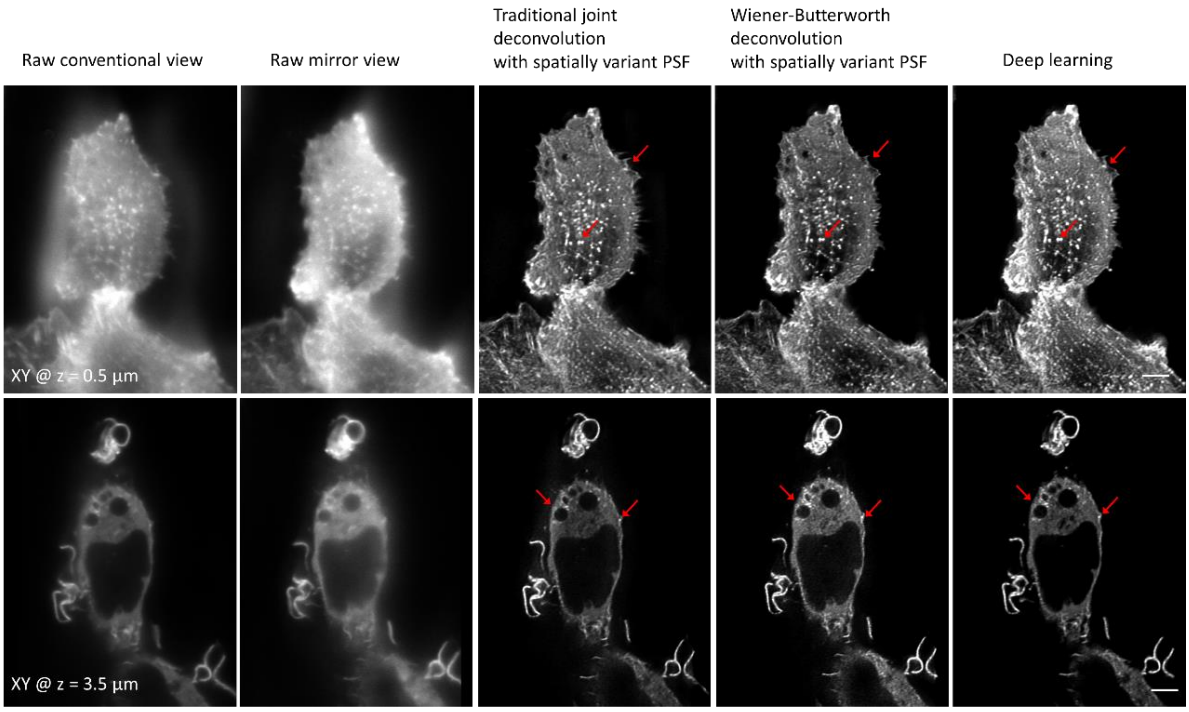

Fig. S4.6, Post-processing mEmerald α-actinin data acquired by reflective LLS microscopy. Two single-plane views at indicated axial depths from the coverlip are shown, columns indicate the two raw, registered inputs (conventional and mirror views), traditional joint deconvolution output, the Wiener-Butterworth deconvolution, and the output from DenseDeconNet deep learning (DL output). The deep learning output closely resembles the results obtained with traditional and Wiener-Butterworth deconvolution, including the retention of fine features (red arrows). Scale bar: 5 µm. Traditional and Wiener-Butterworth deconvolution experiments were repeated on similar datasets at least 2 times, with similar results obtained each time; the deep learning model was trained on one time-lapse dataset and applied to multiple datasets (N>=2), with similar results obtained for each dataset.

3. Network Validation

Reliability testing

Because the kernels in the convolution layers of our network are randomly initialized, the final learned parameters will be slightly different every time training is repeated, even given the same input. To determine if these differences significantly alter the network prediction (a common concern when using deep learning methods), we independently trained DenseDeconNet four times (N=4) to obtain different networks, each trained with randomized orderings of the same input volumes and randomized kernel

initialization, and examined the resulting outputs. We denote the learned parameters of each network as θ_n (m=1,…,N), so the per-pixel mean value of these independent networks is:

$$Mean(x,y) = \frac{1}{N}\sum_{n=1}^{N} output(x,y;\theta_n) \quad (41)$$

where (x,y) represents each pixel's location and $output(x,y)$ represents the normalized output intensity of each network. We also compute the standard deviation (SD) of the *N* networks as a measure of network disagreement:

$$SD(x,y) = sqrt\left[\frac{1}{N}\sum_{n=1}^{N}(output(x,y;\theta_n) - Mean(x,y))^2\right] \quad (42)$$

These quantities provide estimated maps of the average network output, and the disagreement between networks. To provide a more compact measure of network reliability we also computed the coefficient of variation (CV):

$$CV = \frac{\sum_{x,y} SD(x,y)}{\sum_{x,y} Mean(x,y)} \quad (43)$$

A larger CV value represents a larger disagreement between networks.

We performed this analysis on images of membranes and nuclei in live *C. elegans* embryos acquired with diSPIM (**Figs. S4.7-9**), images of GCaMP3 expression in live *C. elegans* embryos acquired with reflective diSPIM (**Fig. S4.10**), and images of α-actinin in live cells acquired with reflective lattice light-sheet (LLS) microscopy (**Fig. S4.11**). In all cases, we found our network to produce highly reliable output (CV < 0.07 with the vast majority of pixels showing SD < 5% of the mean).

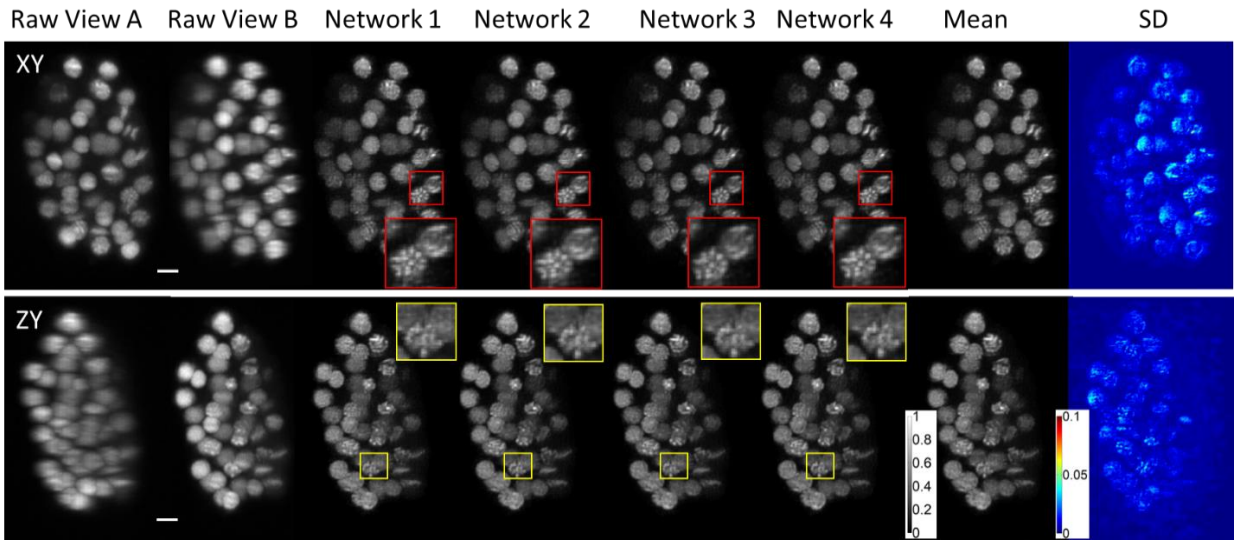

Fig. S4.7, DenseDeconNet reliability testing with dual-view input, GFP-labeled nuclei in live *C. elegans* embryos acquired with diSPIM. From left to right we show the lateral (top) and axial (bottom) maximum intensity projections of input data, predictions of the four networks, the pixel-wise mean, and the pixel-wise standard deviation (SD). The latter is shown in a different colormap, to better highlight the small variations in network performance. Bars at the side of mean and SD images show intensity mapping in arbitrary units. The coefficient of variation is 0.0443 and 0.0401 for lateral and axial projections, respectively, indicating a small disagreement between networks (see also red and yellow higher magnification view insets in network predictions). Scale bars: 5 µm. The deep learning model was trained

on one time-lapse dataset and applied to multiple datasets (N>=2), with similar results obtained for each dataset.

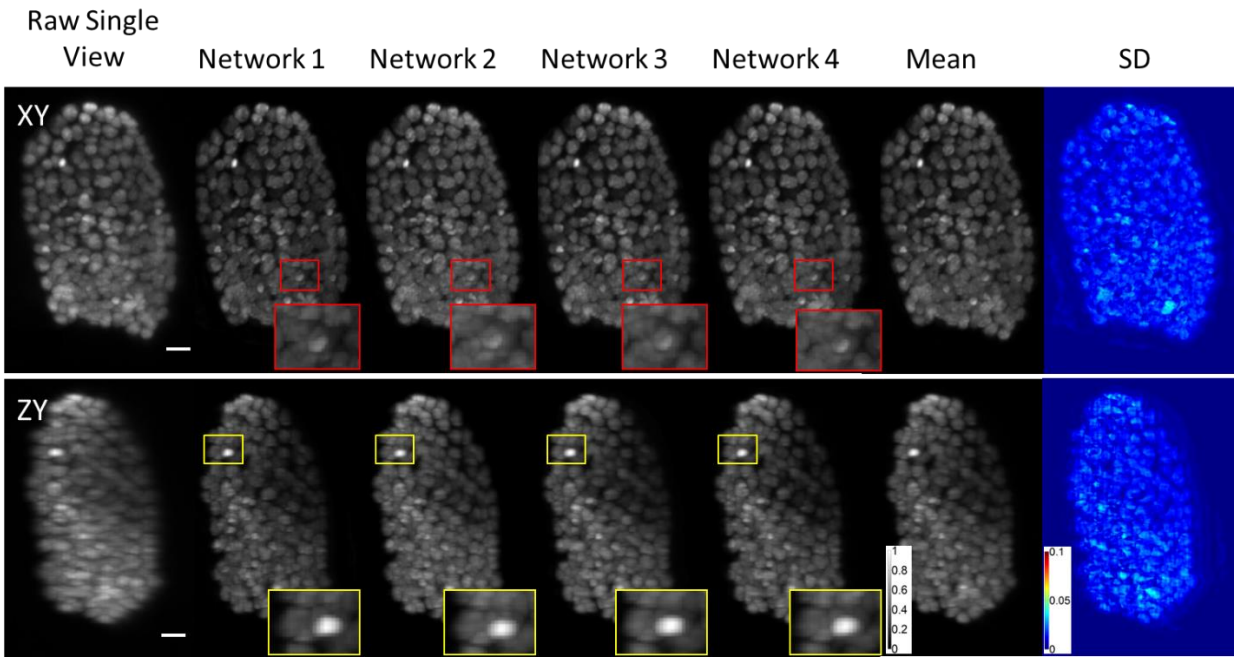

Fig. S4.8, DenseDeconNet reliability testing with single-view input, GFP-labeled nuclei in live *C. elegans* embryos acquired with diSPIM. From left to right we show the lateral (top) and axial (bottom) maximum intensity projections of input data, predictions of the four networks, the pixel-wise mean, and the pixel-wise standard deviation (SD). The coefficient of variation is 0.059 and 0.0575 for lateral and axial projections, respectively, indicating a small disagreement between networks. Scale bars: 5 µm. The deep learning model was trained on one time-lapse dataset and applied to multiple datasets (N>=2), with similar results obtained for each dataset.

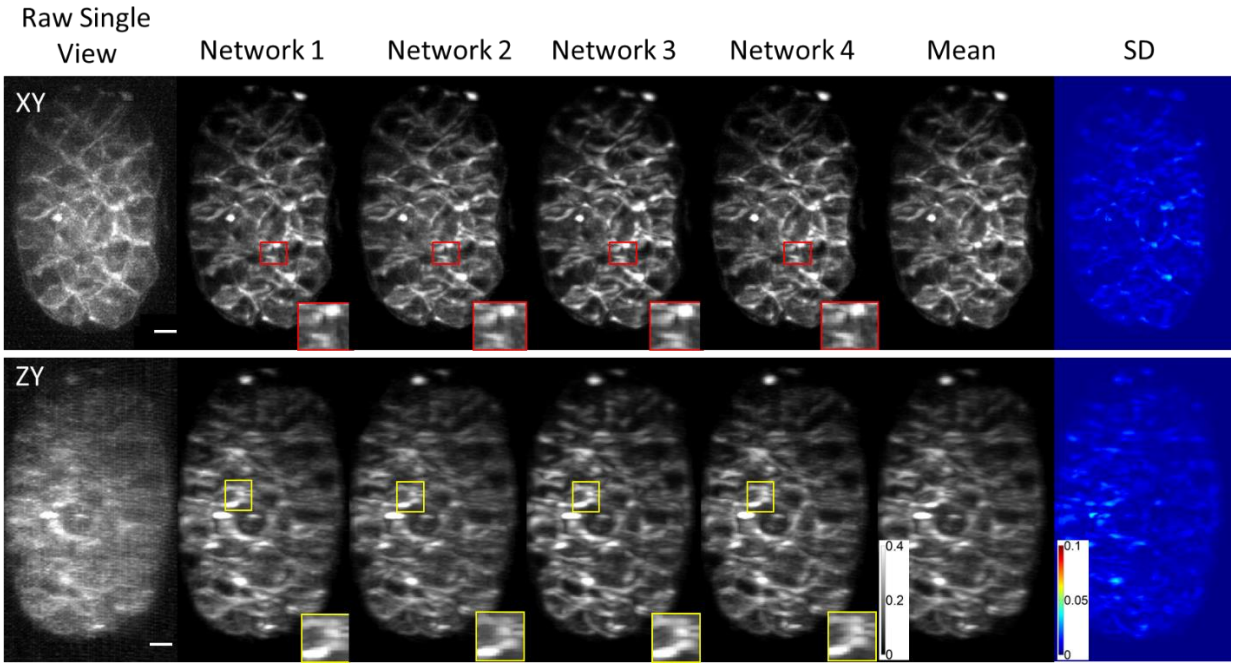

Fig. S4.9, DenseDeconNet reliability testing with single-view input, mCherry-membrane in live *C. elegans* embryos acquired with diSPIM. From left to right we show the lateral (top) and axial (bottom) maximum intensity projections of input data, predictions of the four networks, the pixel-wise mean, and the pixel-wise standard deviation (SD). The coefficient of variation is 0.07 and 0.0675 for lateral and axial projections, respectively, indicating a small disagreement between networks. Scale bars: 5 µm. The deep learning model was trained on one time-lapse dataset and applied to multiple datasets (N>=2), with similar results obtained for each dataset.

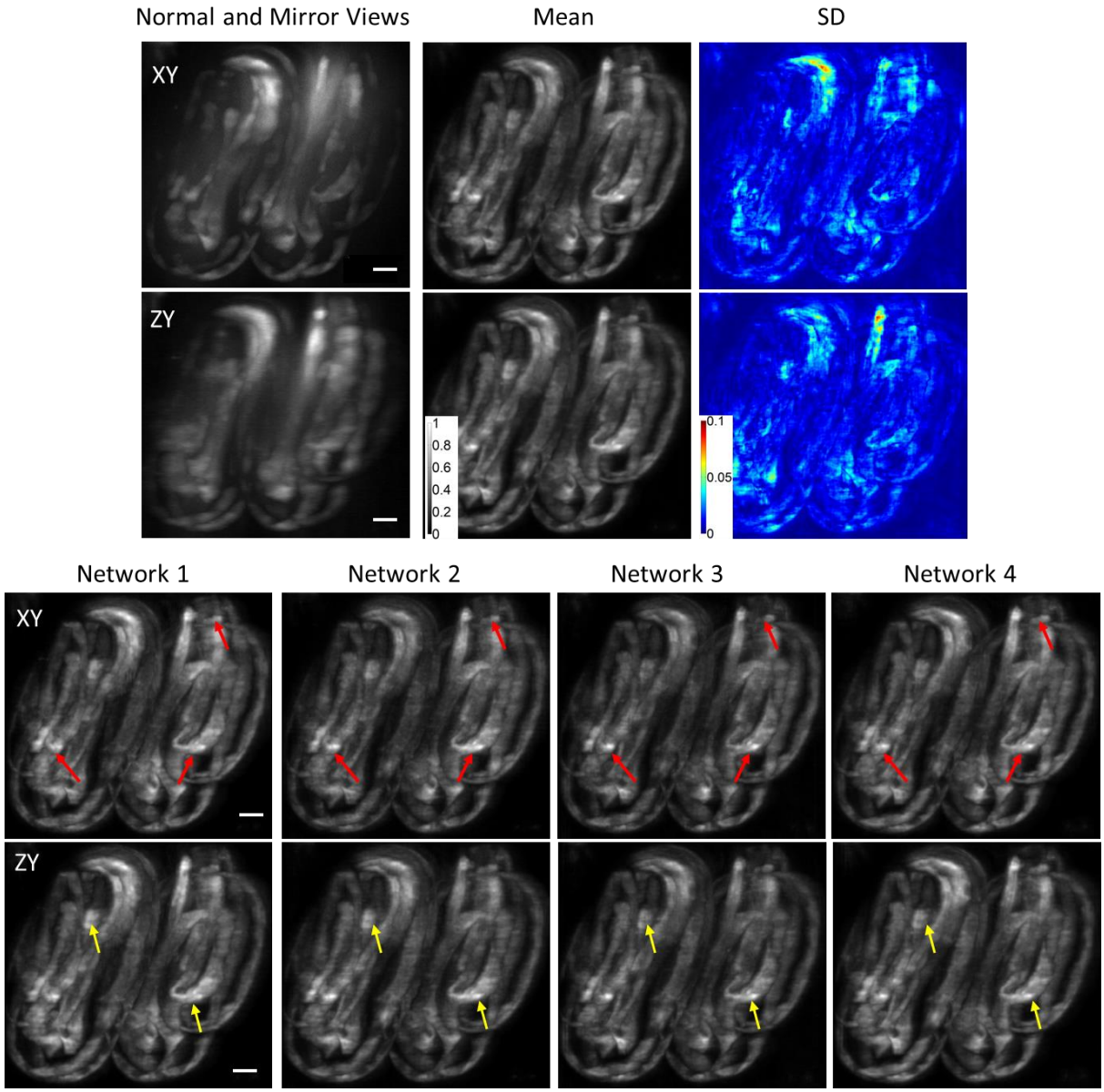

Fig. S4.10, DenseDecon reliability testing with GCaMP3 expression in twitching *C. elegans* embryos imaged with reflective diSPIM. The top two rows compare the raw mirror data (both lateral and axial maximum intensity projections), the pixel-wise mean prediction from the 4 networks, and the pixel-wise standard deviation (SD). The bottom two rows show the the predictions from each of the 4 networks. The coefficient of variation is 0.0538 and 0.0523 for lateral and axial projections, respectively, indicating a small disagreement between networks (yellow and red arrows show regions of slight variation). Scale bars: 5 µm. The deep learning model was trained on one time-lapse dataset and applied to multiple datasets (N>=2), with similar results obtained for each dataset.

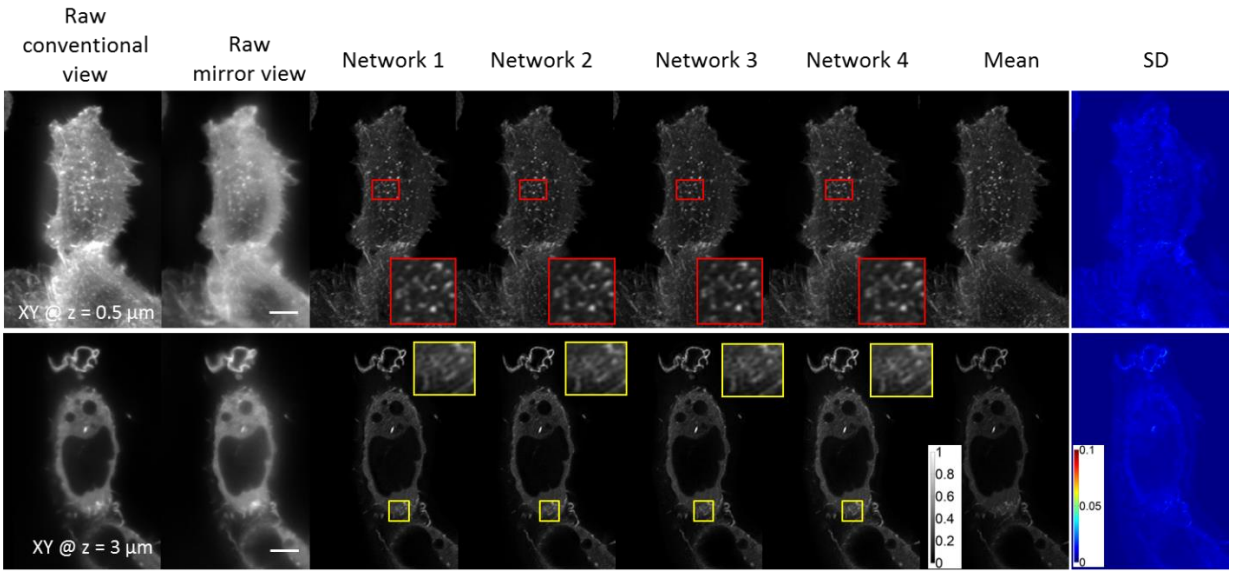

Fig. S4.11, DenseDeconNet reliability testing with mEmerald α-actinin data acquired by reflective LLS microscopy. Shown are two single-plane views at indicated axial depths from the coverlip. Columns indicate the two raw, registered inputs (conventional and mirror views), predictions of the four networks, the pixel-wise mean, and the pixel-wise standard deviation (SD). The coefficient of variation is 0.0389 and 0.0664 for the two examples, indicating a small disagreement between networks. Scale bars: 10 µm. Experiments were repeated on similar datasets at least 2 times, with similar results obtained each time; representative data from a single experiment are shown.

Generalization testing

By generalization, we mean the neural network's ability to produce sensible outputs in response to unseen data. One of the main impediments to generalization is overfitting, which can be caused by insufficient training data or by a poor choice of network parameters. To examine the generalization of DenseDeconNet, we calculated the convergence of the averaged MSE and the averaged loss as a function of epoch (up to 100 epochs, 200 iterations for each epoch) during training and validation for both single-view input and dual-view inputs of GFP-labeled nuclei in live *C. elegans* embryos acquired with diSPIM (**Fig. S4.12**). Here we randomly selected 200 datasets (by 'dataset' we mean the inputs and deconvolution of those inputs as ground truth) for training and 91 datasets for validation. In each epoch, the values of averaged MSE and averaged loss were computed as:

$$ave\_MSE = \frac{\sum_{n=1}^{N} MSE_n}{N} \tag{44}$$

$$loss = MSE - \ln\left(\frac{1+SSIM}{2}\right) \tag{45}$$

$$ave\_loss = \frac{\sum_{n=1}^{N} loss_n}{N} \tag{46}$$

, where *N* is the number of datasets used for training or validation.

With single-view inputs (**Fig. S4.12a, b**), the averaged MSE and loss converge at ~80 epochs, whereas for dual-view inputs (**Fig. S4.13c, d**), the averaged MSE and loss converge more rapidly and achieve values more than 10-fold smaller than those under single-view input training, indicating that the dual-view input training model outperforms the single-view input model. This result is unsurprising as more information is contained with two inputs. In both models, the averaged MSE and loss for training and validation datasets are overlap until ~80 epochs. This overlap shows that DenseDeconNet neither underfits nor overfits our data.

For the results we presented in this paper, we used ~40 epochs (i.e., 7000 - 8000 iterations for the nuclei-model shown in **Table S4.1**). This resulted in a ~56-hour training time for the dual-view input nuclear diSPIM model (**Fig. S4.4**). However, during the revision process for this manuscript, we found that training time can be significantly reduced to only 2.5 hours if training is performed with a small cropped subvolume (~15 MB) instead of the entire volume (~80 MB), while still maintaining acceptable restorations (SSIM values of 0.96-0.99 relative to the ground truth, **Fig. S4.13**).

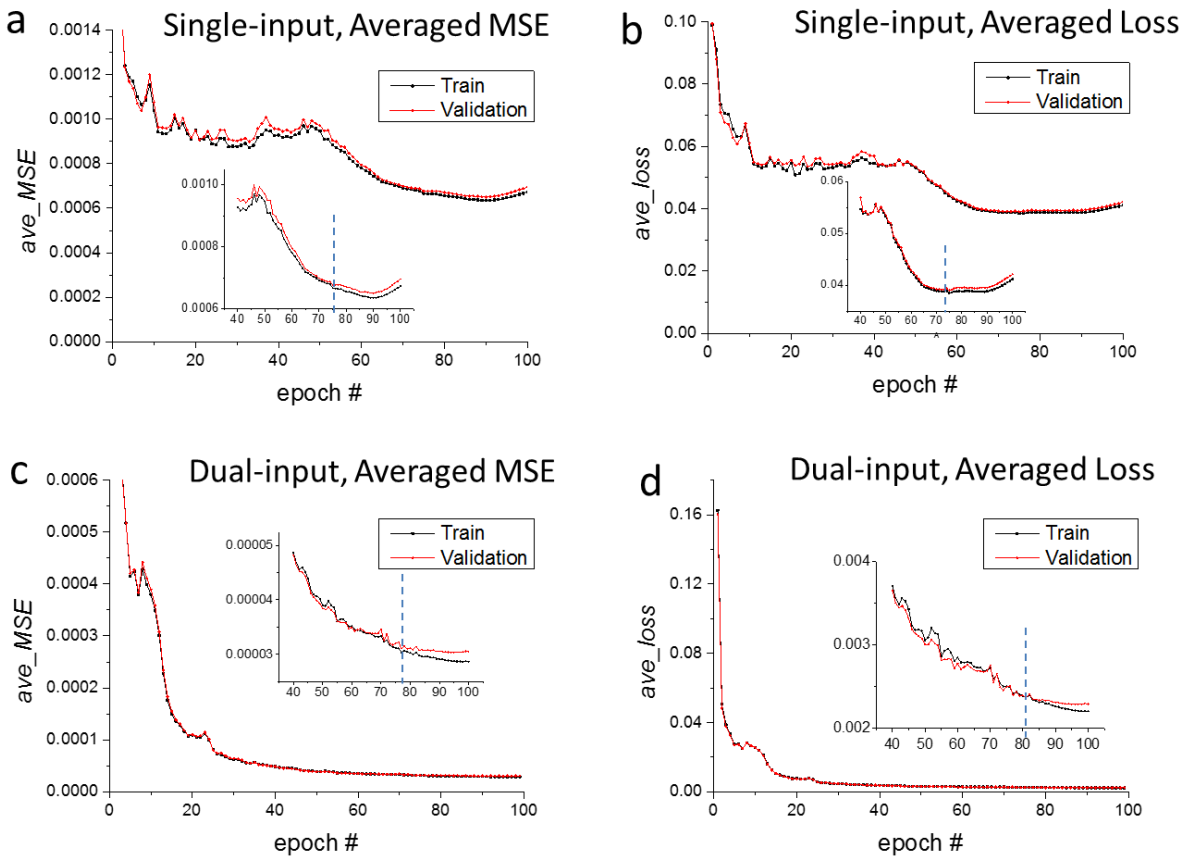

Fig. S4.12, Convergence of averaged MSE (a, c) and averaged loss (b, d) on diSPIM nuclear models as a function of epoch #. Results for single (**a, b**) and dual (**c, d**) input models are included. The blue dashed lines indicate the approximate epoch # where the values of averaged MSE and loss between training and validation datasets begins to diverge (see also insets).

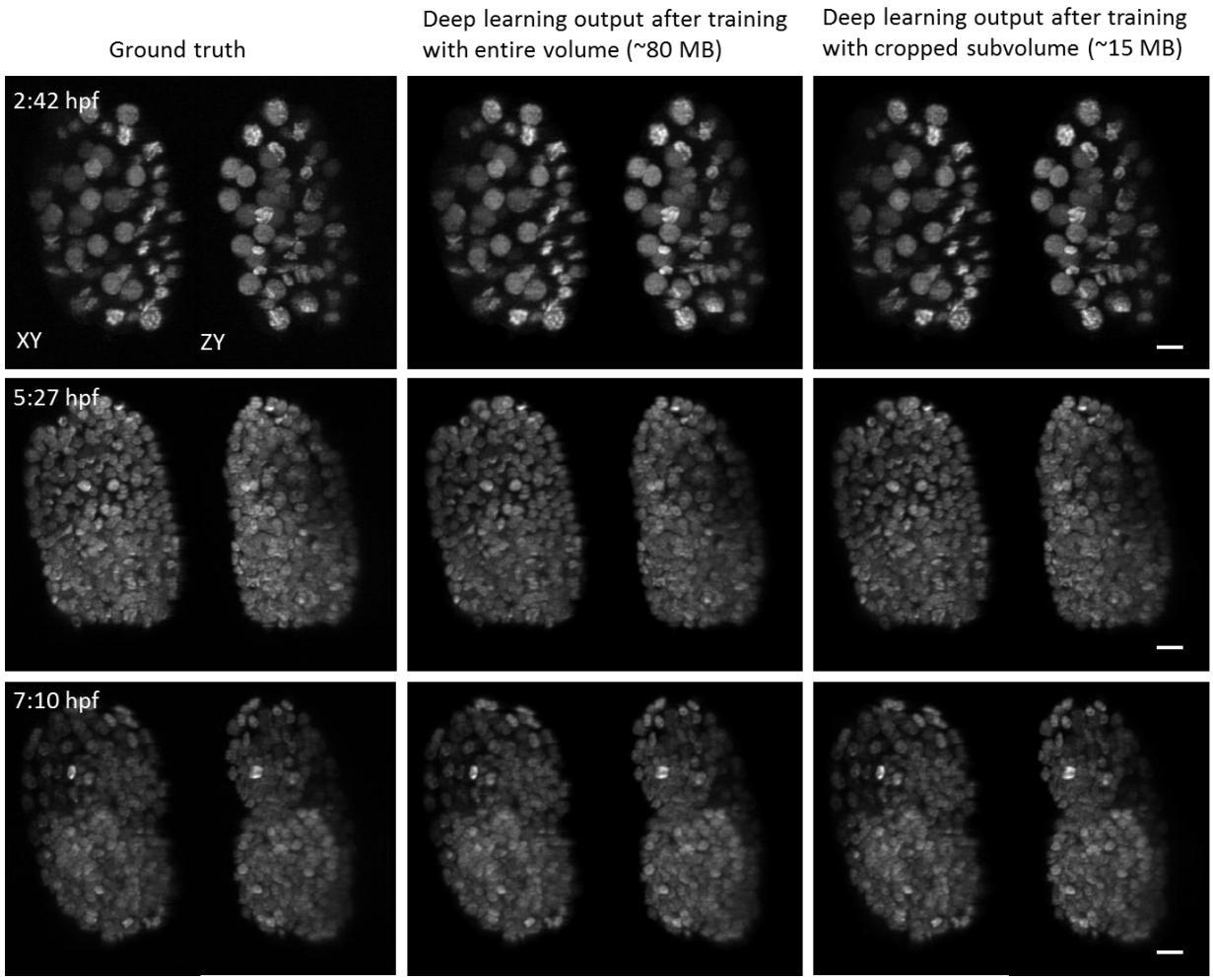

Fig. S4.13, Comparison of restoration quality when training DenseDeconNet with the entire volume vs. cropped subvolumes. Results correspond to dual-view inputs showing GFP-labeled nuclei in live *C. elegans* embryos, acquired with diSPIM. From left to right we show the traditional joint deconvolution ground truth, the deep learning output with the model established on the entire volume, and the output with the model trained on a cropped subvolume. Maximum intensity projections along lateral and axial views at three time points are shown for comparison. The two networks predict the nuclei structures with same SSIM values relative to the ground truth (top row: 0.99; center row: 0.96; bottom row: 0.99). hpf: hours post fertilization. Scale bars: 5 μm. The deep learning model was trained on one time-lapse dataset and applied to multiple datasets (N>=2), with similar results obtained for each dataset.

Transfer learning

We next assessed if a network trained on one dataset could be directly applied to other datasets with different structures or acquired with different microscopes. First, we applied the dual-input network trained by images of mEmerald α-actinin in live cells acquired with reflective LLS microscopy to another mEmerald α-actinin dataset with visually different morphology (**Fig. S4.14**). We found that the neural network removed epi-fluorescence and improved resolution isotropy, and agreed well with the deconvolved ground truth (SSIM 0.97). Second, we applied the single-input network trained with

mCherry-labeled membrane data to the GFP-labeled nuclear dataset (**Fig. S4.15**). In this case, the network prediction was suboptimal (SSIM relative to the ground truth 0.65 for the membrane model vs. 0.84 for the nuclear model), which follows our intuition that membrane and nuclei structures are very different. We nevertheless found that the membrane-specific network could be rapidly retrained for nuclear prediction with much less nuclear training data than a randomly initialized network. For example, prediction results were comparable to the nuclei-specific model (180 pairs of input/ground truth data, 12000 iterations) when retraining the membrane-specific network with only 100 pairs of nuclei data and 3000 iterations (**Fig. S4.15**, SSIM 0.87).

Last, we applied the network trained by the images of GCaMP3 expression in live *C. elegans* embryos acquired with reflective diSPIM with rolling shutter detection[14,15] to another embryo imaged with reflective diSPIM, but without rolling shutter detection (**Fig. S4.16**). Rolling shutter detection more effectively rejects epifluorescence contamination in reflective imaging[16], which can be modeled using an appropriate detection PSF. Although the network prediction removed the epifluorescence contamination and recovered isotropic resolution in the new data, the predictions show areas of obvious disagreement compared to the ground truth joint deconvolution (which used a PSF appropriate for the data, i.e. without rolling shutter detection). This result is consistent with the current result that most deep learning networks typically do not generalize well to data obtained from a different type of microscope[17,18].

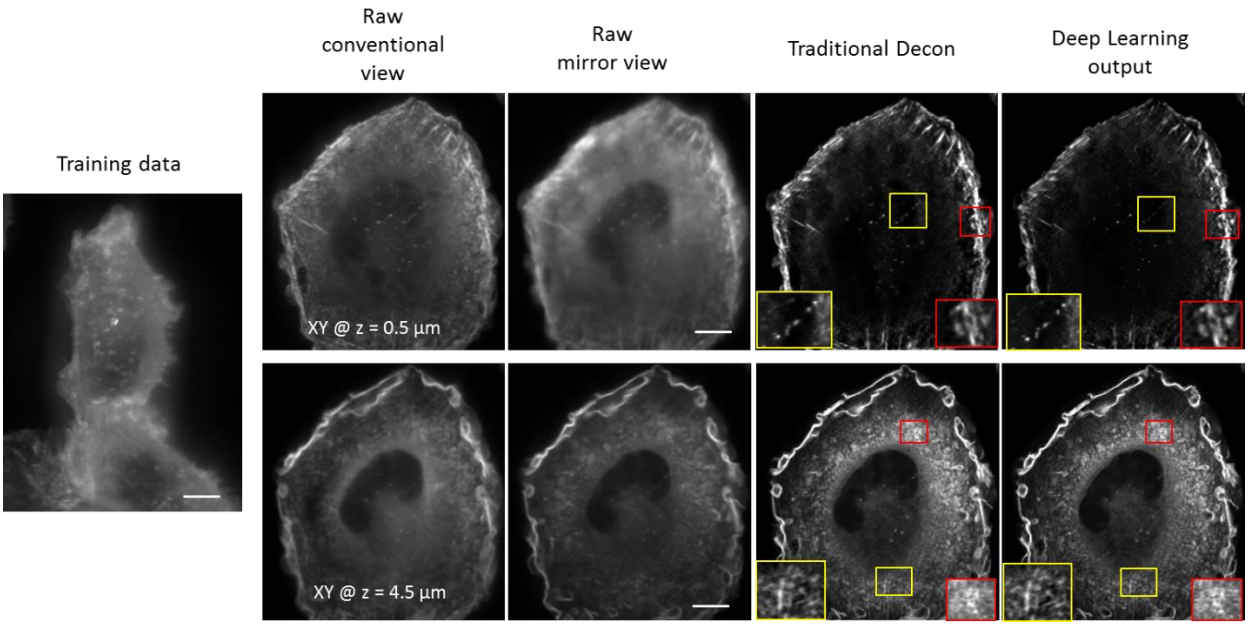

Fig. S4.14, Network transfer testing on images of different cells expressing mEmerald α-actinin, acquired by reflective LLS microscopy. Leftmost panel shows an example of the training dataset at a single plane. Right columns show two single-plane views of other cells (from a different dataset) at indicated axial depths from the coverslip, including raw conventional view, raw mirror view, ground truth spatially variant deconvolution result ('Traditional Decon'), and the deep learning output with the model established from the first cell. The two cells exhibit different morphologies, but the network predicts fine structures well (compare higher magnification views in right hand columns) with an SSIM value of 0.97 relative to the ground truth. Scale bars: 10 µm. Traditional deconvolution experiments were repeated on similar datasets at least 2 times, with similar results obtained each time; the deep learning model was trained on one time-lapse dataset and applied to multiple datasets (N>=2), with similar results obtained for each dataset.

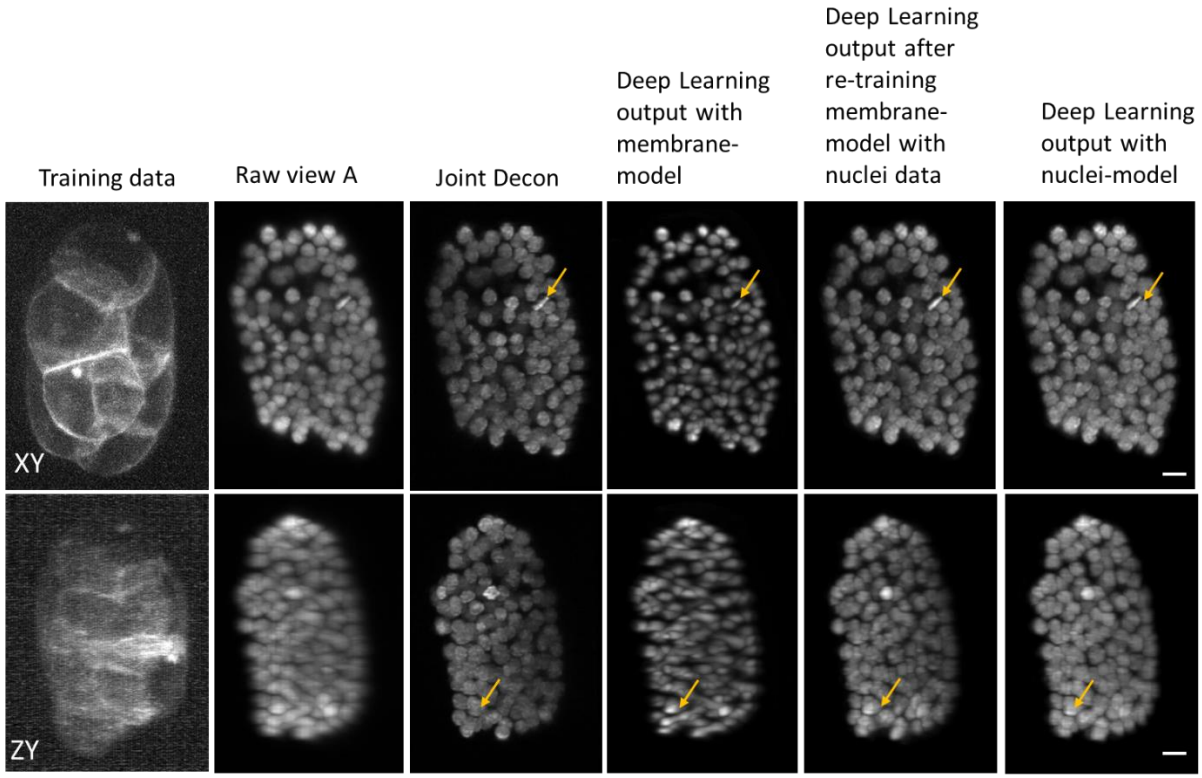

Fig. S4.15, Network transfer testing on images of GFP-labeled nuclei in live *C. elegans* embryos acquired with diSPIM, using the single-input model trained on images from the mCherry-membrane dataset. Shown are exemplary images of mCherry-labeled membranes as the training data, a raw image of GFP-labeled nuclei data as the network input, traditional joint deconvolution ('Joint Decon') ground truth, deep learning output with the membrane-model, deep learning output after retraining with nuclei images, and deep learning output with the original model trained only with nuclear data. Maximum intensity projections along lateral and axial views are shown for comparison. As shown by the arrows, the model that is trained only with membrane data distorts nuclear shapes, but performs well if retrained with nuclear data. The SSIM values of the predictions relative to the ground truth are 0.65, 0.84, and 0.87 for the membrane-model, the original nuclei-model, and the membrane-model retrained with nuclei images, respectively. Scale bars: 5 µm. Traditional joint deconvolution experiments were repeated on similar datasets at least 2 times, with similar results obtained each time; the deep learning model was trained on one time-lapse dataset and applied to multiple datasets (N>=2), with similar results obtained for each dataset.

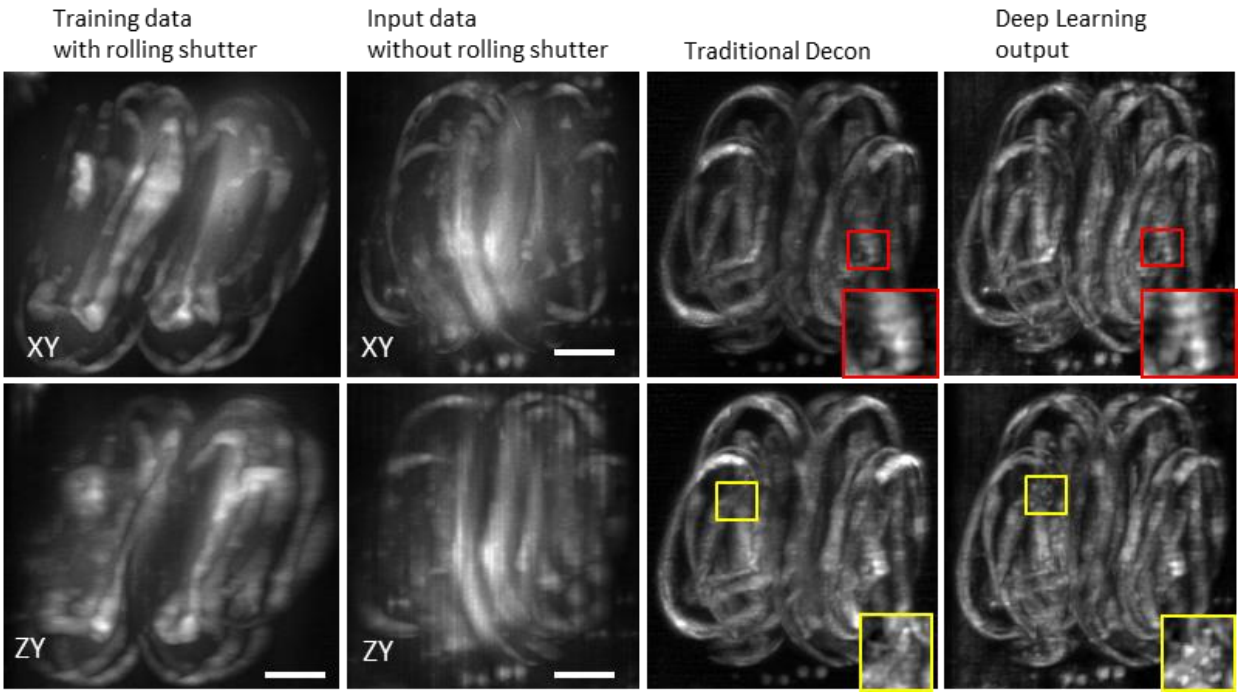

Fig. S4.16, Network transfer testing on images of GCaMP3 expression in live *C. elegans* embryos acquired with reflective diSPIM, with and without rolling shutter detection. Leftmost column shows an example of the training dataset from one embryo measured with reflective diSPIM with rolling shutter detection while the second column shows another embryo imaged without rolling shutter detection. The third column is a ground-truth, traditional spatially variant deconvolution result ('Traditional Decon', using a PSF appropriate for the data in column 2, i.e. without rolling-shutter detection). The final column shows the deep learning output when DenseDeconNet trained on data acquired with the rolling shutter (first column) is applied to data acquired without the rolling shutter (second column). Lateral and axial maximum intensity projections are shown for comparison. Although DenseDeconNet removes epifluorescence and recovers resolution isotropy, the predicted output shows some areas of obvious difference compared to the ground truth (higher magnification views in yellow and red). The SSIM value of the prediction relative to the ground truth drops from 0.93 with the original model trained without rolling shutter to 0.81 when trained with rolling shutter. Scale bars: 10 μm. Traditional deconvolution experiments were repeated on similar datasets at least 2 times, with similar results obtained each time; the deep learning model was trained on one time-lapse dataset and applied to multiple datasets (N>=2), with similar results obtained for each dataset.

Table S4.1, Parameters for all datasets used in deep learning

Samples	***C. elegans* embryo membrane**	***C. elegans* embryo nuclei**		***C. elegans* embryos expressing GCaMP3**	**U2OS cells expressing mEmerald-α-Actinin**
Microscope	diSPIM	diSPIM		reflective diSPIM	reflective LLS
Input view number	1	1	2	2	2
Training volumes	160	180	180	100	80
Test volumes	40	110	110	55	20
Training volume size, voxels	240x340x246 (76.6 MB, 32 bit)	240x360x240 (79 MB, 32 bit)	240x360x240x2 (158 MB, 32 bit)	340x170x340x2 (150 MB, 32 bit)	210x271x198x2 (86 MB, 32 bit)
Test volume size, voxels	240x340x246 (76.6 MB, 32 bit)	240x360x240 (79 MB, 32 bit)	240x360x240x2 (158 MB, 32 bit)	340x310x340x2 (274 MB, 32 bit)	398x526x198x2 (315 MB, 32 bit)
Learning rate, r_0	0.07	0.04	0.004	0.004	0.005
Decay_step	200	150	600	600	400
Decay_rate, *k*	0.98	0.98	0.96	0.985	0.98
λ	1.5	1.2	1.3	1.3	1.3
Training iteration Number	8000	7000	7000	12000	13000
Training time	~57 h	~56 h	~56 h	~10.8 h	~8.2 h
Test time for each volume	~1 s	~0.81 s	~1.23 s	~1.68 s	~2 s

For data with dual-view inputs, the additional dimension (2) represents the concatenation/channel dimension. Training and model application were performed on a PC workstation equipped with 32 GB of memory, an Intel(R) Core (TM) i7 – 8700K, 3.70 GHz CPU, and two Nvidia GeForce GTX 1080 Ti GPU cards with 11 GB memory.

Table S4.2, MSE and SSIM evaluation between joint deconvolution results (ground truth) and deep learning test outputs.

Samples	***C. elegans* embryo membrane**		***C. elegans* embryo nuclei**			***C. elegans* embryos expressing GCaMP3**	**U2OS cells expressing mEmerald-α-Actinin**
Microscope	diSPIM		diSPIM			reflective diSPIM	reflective LLS
Input view number	1		1		2	2	2
Time point	@ 1:00 hpf	@ 4:00 hpf	@ 7:40 hpf	@ 11:00 hpf	@ 7:00 hpf	@ 6.3 s (#19 in the movie)	@ 5 s (#3 in the movie)
MSE	3.0e-04	2.9e-04	6.6e-04	3.5e-03	0.6e-04	4.8e-04	5.0e-05
SSIM	0.684	0.923	0.805	0.440	0.986	0.923	0.965

MSE: mean squared error; SSIM: structural similarity index. Except for the late twitching embryo with single view input, the MSE values are all < 0.001. We suspect this larger MSE value is due to the pronounced twitching late in embryogenesis. SSIM values show more variability, with single-view inputs for the membrane and late nuclear datasets resulting in lower SSIM values, presumably due to registration artifacts in the ground truth data. For datasets with two inputs, the similarity between the ground truth joint deconvolution and the deep learning output is very high. hpf: hours post fertilization.

References

1 He, K., Zhang, X., Ren, S. & Sun, J. Deep Residual Learning for Image Recognition. *IEEE Conference on Computer Vision and Pattern Recognition*, doi:10.1109/CVPR.2016.90 (2016).

2 Szegedy, C. *et al.* Going deeper with convolutions. *IEEE Conference on Computer Vision and Pattern Recognition*, doi:10.1109/CVPR.2015.7298594 (2015).

3 Simonyan, K. & Zisserman, A. Very Deep Convolutional Networks for Large-Scale Image Recognition. *ArXiv*, 1409.1556 (2014).

4 Ioffe, S. & Szegedy, C. Batch Normalization: Accelerating Deep Network Training by Reducing Internal Covariate Shift. *ArXiv*, 1502.03167 (2015).

5 Haykin, S. *Neural Networks: A Comprehensive Foundation*. (Prentice Hall 1994).

6 Ronneberger, O., Fischer, P. & Brox, T. U-Net: Convolutional Networks for Biomedical Image Segmentation. *ArXiv*, 1505.04597 (2015).

7 Odena, A., Dumoulin, V. & Olah, C. Deconvolution and Checkerboard Artifacts. *Distill* (2016).

8 Huang, G., Liu, Z., van der Maaten, L. & Weinberger, K. Q. Densely Connected Convolutional Networks *arXiv*, 1608.06993 (2016).

9 Long, J., Shelhamer, E. & Darrell, T. Fully convolutional networks for semantic segmentation. *IEEE Conference on Computer Vision and Pattern Recognition*, doi:10.1109/CVPR.2015.7298965 (2015).

10 Nair, V. & Hinton, G. E. Rectified linear units improve restricted boltzmann machines. *Proceedings of the 27th International Conference on Machine Learning* (2010).

11 Xu, B., Wang, N., Chen, T. & Li, M. Empirical Evaluation of Rectified Activations in Convolutional Network. *ArXiv*, 1505.00853 (2015).
12 Wang, Z., Bovik, A. C., Sheikh, H. R. & Simoncelli, E. P. Image Quality Assessment: From Error Visibility to Structural Similarity *IEEE Trans Image Process.* **13**, 600-612 (2004).
13 Kingma, D. P. & Ba, J. Adam: A Method for Stochastic Optimization. *ArXiv*, 1412.6980 (2014).
14 Baumgart, E. & Kubitscheck, U. Scanned light sheet microscopy with confocal slit detection. *Opt Express* **20**, 21805-21814, doi:10.1364/Oe.20.021805 (2012).
15 Wu, Y. C. *et al.* Simultaneous multiview capture and fusion improves spatial resolution in wide-field and light-sheet microscopy. *Optica* **3**, 897-910, doi:10.1364/Optica.3.000897 (2016).
16 Wu, Y. C. *et al.* Reflective imaging improves spatiotemporal resolution and collection efficiency in light sheet microscopy. *Nat Commun* **8**, doi:ARTN 1452, 10.1038/s41467-017-01250-8 (2017).
17 Weigert, M. *et al.* Content-aware image restoration: pushing the limits of fluorescence microscopy. *Nat Methods* **15**, 1090-1097, doi:10.1038/s41592-018-0216-7 (2018).
18 Belthangady, C. & Royer, L. A. Applications, promises, and pitfalls of deep learning for fluorescence image reconstruction. *Nat Methods* **16**, 1215-1225, doi:10.1038/s41592-019-0458-z (2019).